ʻUpena o Kū

Journal of Science, Technology, Engineering, and Mathematics

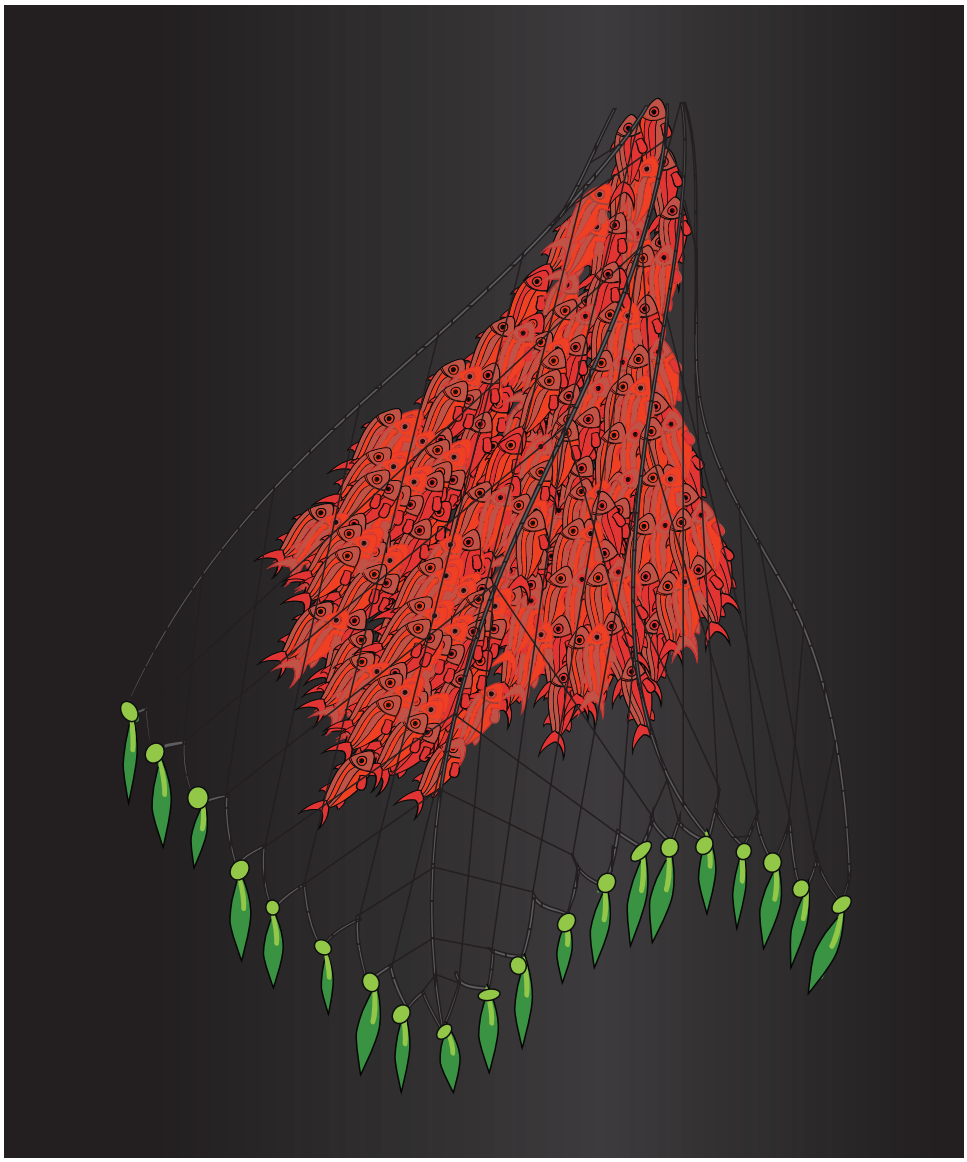

Board of Student Publications

Kapiʻolani Community College / Spring 2014

ʻUpena o Kū

Journal of Science, Technology, Engineering, and Mathematics

UNIVERSITY of HAWAIʻI®
KAPIʻOLANI
COMMUNITY COLLEGE

Board of Student Publications
4303 Diamond Head Road
Honolulu, Hawaiʻi 96816

'Upena o Kū ("Net of Kū") publishes the research writing of Kapi'olani Community College's Science, Technology, Engineering and Mathematics program. The goal of the STEM program is to improve the quality of education in the fields of STEM through various initiatives, including undergraduate research projects, peer mentoring, and summer bridge programs. The effort has increased the number of KCC students transfering to four-year degree programs to prepare for careers in one of the STEM disciplines.

KCC's STEM program was established in August of 2005 with a $1.25 million grant from the National Science Foundation (NSF)'s Tribal Colleges and Universities Program (TCUP), one of whose goals was to increase student diversity in the STEM disciplines, with a special emphasis on Native Hawaiian students. Since that initial grant, additional grants have been awarded.

For more about KCC's STEM program, visit its website at <http://stem.kcc.hawaii.edu/>.

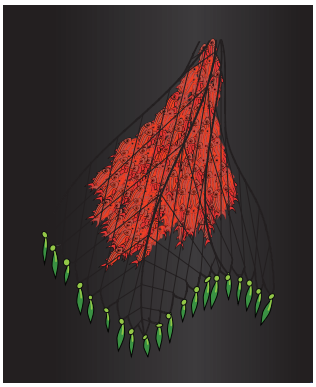

Cover Art: 'Upena o Kū by Andrew Chang, Kumu Kapulani Landgraf, and Kumu Mrs. Keolani Noa

'Upena o Kū, by Kumu Mrs. Keolani Noa

Designed to strengthen the quality of our existence, the 'Upena sewn together is the foundation house to inspire a desire to rediscover the STEM within. Science, technology, engineering and mathematics is the magnet to reinforce the natural intellectual movement, like that of a school of fish. As we follow, pushing upward, we evolve as models that burst of Kū success. As one recognizes that 'IKE and the readiness to persist is beyond knowing, research becomes a level of learning by doing.

'Upena o Kū is published by the Board of Student Publication, Kapi'olani Community College, University of Hawai'i.

TABLE OF CONTENTS

Life Sciences

Physical Sciences

Pre-Engineering

Survey of Biodiversity in Kawainui Marsh

By Leila Jaffuel, Bradley Hughes, Mehana Horner, Courtni Poti, Pookela Stillman Reyes, and Keonona Cullen (*Faculty Mentor*: Mackenzie Manning)

INTRODUCTION

Our ancestors understood the importance of perpetuating natural resources we depend on for sustenance. No place better demonstrates their relationship with the aina than the ahupua'a of Kailua. Between Kailua Bay and the fresh water running through the veins of Maunawilli are the expansive wetlands of Kawainui. Early Polynesian settlers quickly learned to utilize these natural resources, but they also developed advanced systems to increase productivity of vegetation and fish while maintaining the land from which it came. By diverting streams, ditches called 'auwai were formed for irrigation that allowed the construction of what was once the largest loko'ia (fish pond) in Hawaii.

As the culture surrounding Kawainui evolved with time, so did the physical environment. After the destruction of land from erosion, development and soil run-off, we're fortunate that Kawainui still remains the largest wetland in Hawaii. The purpose of our research was to survey and determine an accurate ratio of native to invasive species. The conservation of this unique environment is critical for several of Hawaii's endangered birds and we hope the data we've collected will contribute to restoration efforts and bringing awareness to Kawainui.

MATERIALS & METHODS

- The transect from which we surveyed the plant diversity was 30m in length and 5m wide.
- Flags were used to mark every 5m and flagging tape to outline each quadrant.
- The illustration below shows the layout of our transect (5 quadrants) and the 10 locations from which we took plant surveys.

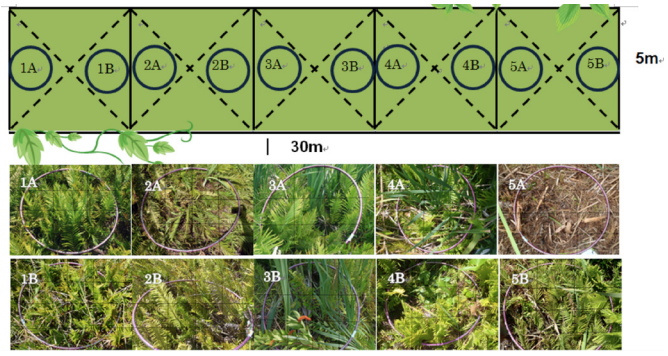

- Timed bird observations were taken on 3 consecutive days using a high-optic Nikon Field scope to identify Avian species.
- Aquatic organism samples were collected (using nets and looking glasses) from opposite ends of the fishpond and recorded. (Image shown bottom left)
- A GPS was also used to plot the waypoint of each flag. (The waypoints recorded were later used to illustrate our research and findings on Google Maps

RESULTS

We found a high number of non-native species in all areas we examined. For the flora we found little to no endemic species and observed mostly cattail and non-native grasses. With the avian population we were excited to see both alae ula and ae'o, which are among the species that are being protected in Kawainui Marsh. The fishes that were seen were all non-native except for one sighting of a o'opu.

Photo 1: Measuring the perimeter of our transect.

Photo 2: Bird watching with the Nikon field scope.

Photo 3: Using nets to collect aquatic samples.

The Avian count (***Figure 1***) shows the species observed within Kawainui marsh adjacent to Ulupo Heiau.

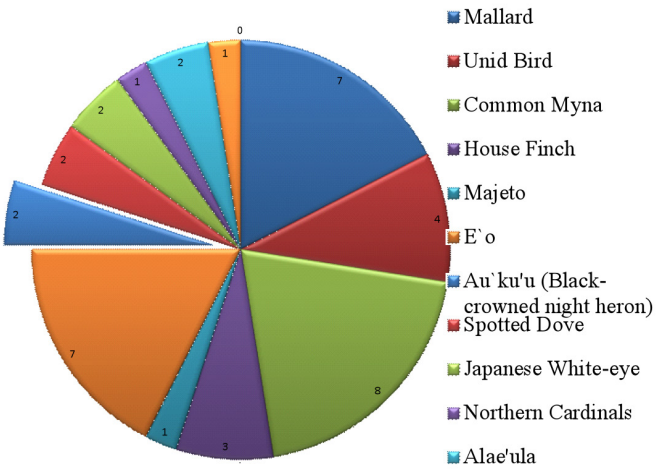

Figure 1. Avian Count

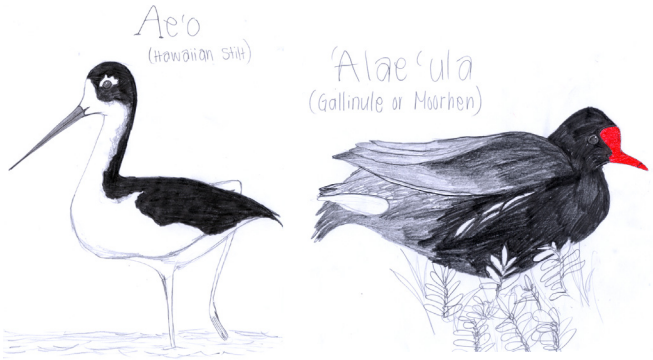

The plant species chart (***Figure 2***) illustrates the flora count within our transects and reveals that the Neke fern is the predominant species in the area we sampled.

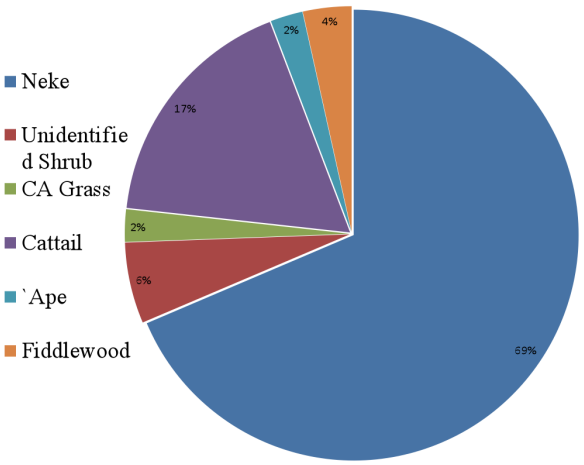

Figure 2. Plant Species

In terms of diversity (***Figure 3***) we observed more non-native species; however, the Neke fern is more abundant so that it dominated the area sampled and influenced the results as shown in our graph.

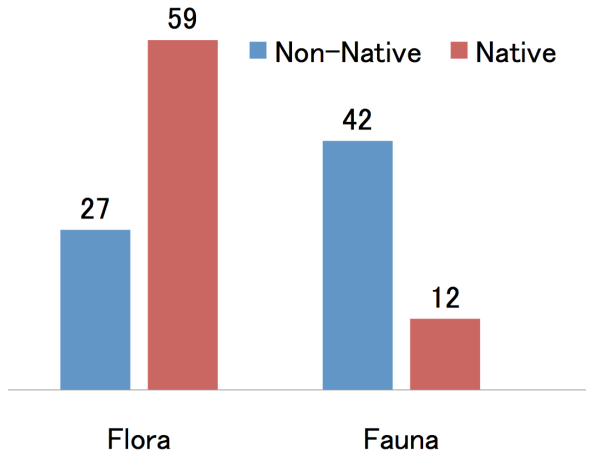

Figure 3. Native vs. Non-Native Species

	Common Name	Scientific Name	Common Name	Scientific Name
Native:	O'opu	Awaous Guamensis		
Non-native:	Guppy	Poecilla Reticulata	Roseate Skimmer Dragonfly	Orthemis Ferruginea
	Sword Tail	Xiphophorus Helleri	Beetles	Coleoptera
	Cat Fish	Silurus Glanis	Grasshoppers	Caelifera Orthoptera
	Telapia	Oreochromis Neloticus	Apple Snails	Pomala Canaliculata
	Tadpoles	Raniceps Raninups	Paper Wasp	Polistes Aurifer
	Cane Toad	Bufo Marinus		

We saw a significant decline in the number of birds observed on the first and third days (we speculate that this was due to poor weather). The second day was the highest avian count (climate was warmer and clear skies). Non-native apple snails are problematic in the marsh.

Photo 4 below: a female snail.

Photo 5 below: Apple snail's eggs.

CONCLUSIONS

- 1 of 6 plant species found were native.
- 4 of 19 animals species found were native.
- From our findings restoration efforts are supporting native flora and fauna at Kawainui Marsh.
- On average we saw 4 native birds everyday.
- We hope to see restoration efforts continue at Kawainui.

LITERATURE CITED

Douglas Pratt, H. “A Pocket Guide To Hawai’i’s Trees and Shrubs.” Mutual Publishing. 1998.

Howarth, Francis G..& Mull, William P. “Hawaiian Insects And Their Kin.” University of Hawaii Press Honolulu. 1992.

U.S. Geological Survey. “Ulupo Heiau Historical Site.” Google Earth. 2012. July 3, 2012.

Walther, Michael. “A Guide to Hawaii’s Coastal Plants.” Mutual Publishing. May 2004.

ACKNOWLEDGEMENTS

We would like to thank Mackenzie Manning our instructor. “Doc” Burrows of ‘Ahahui and Kailua Hawaiian Civic Club for allowing us to do our research. Also Mahalo Nui to Aunty Keolani Noa for giving us a this opportunity and her unwavering support. Mahalo ke Akua.

FOR FURTHER INFORMATION

For more information on this and related research please visit www.ahahui.net, call (808)-263-8008 or email ahahui@hawaii.rr.com. For more information about Kawainui Marsh visit www.hawaiistateparks.org or call (808)587-0300.

Ulupo Heiau: it's all in the water! An exploratory study of water quality

By Melanie Akiu, Melanie Keliipuleole, Kalai Madrona, and Lindsey Watanabe
(*Faculty Mentor*: Mackenzie Manning)

INTRODUCTION

Kawainui Marsh, the largest marsh in Hawaii, is home to Ulupo Heiau, a very important cultural site for native Hawaiians. Located in Kailua, Oahu, HI, Ulupo Heiau was once a mapele, or agricultural heiau, erected to conduct certain rituals to insure the wellness and fertility of crops while using nearby natural springs. Currently, restoration projects are underway that aim to restore this heiau as a functional mapele although baseline data characterizing various aspects of water quality are lacking. Characterizing and monitoring water quality is important in understanding the overall health and sustainability of the heiau to support a diversity of life.

To address this knowledge gap, during the summer of 2012, we set out to gather baseline data to characterize water quality along multiple sites at Ulupo Heiau including, four natural springs, two lo'i kalo, and a portion of the Kawainui Marsh in an effort to support restoration efforts.

Lo'i Kalo

Old Spring

Kawainui Marsh

MATERIALS & METHODS

From June 25th to June 28th, a duration of four days, water samples were taken from various sites to conduct tests using a LaMotte spectrophotometer to determine the levels of nitrates (NO3), ammonia (NH3), tannins, and turbidity. YSI meters were used to determine the levels of oxygen, conductivity, temperature, and pH.

RESULTS

Table 1 below shows average data across all four days for all variables measured.

	NO_3 (mg/L)	NH_3 (mg/L)	Tannins (mg/L)	Turbidity (NTU:FTU)	Temperature (°C)	DO (mg/L)	DO (%)	Conductivity (ms/cm)	pH
First Spring	17	0.06	0.7	4	25.7	4.67	62	0.2650	7.58
Heiau Spring	30	0.07	0.6	0	25.4	5.27	64	0.7023	7.00
Lo'i Entrance	15	0.07	0.7	1	27.0	6.37	79	0.3577	7.91
Sugar Spring	22	0.06	0.3	0	26.1	3.30	41	0.4916	6.81
Old Spring	12	0.40	1.5	11	24.9	0.55	7.0	0.5660	6.72
Lo'i Exit	20	0.13	1.5	50	28.7	4.70	59	0.5300	8.03
Marsh	18	0.25	2.1	40	28.6	4.74	61	0.5190	7.64

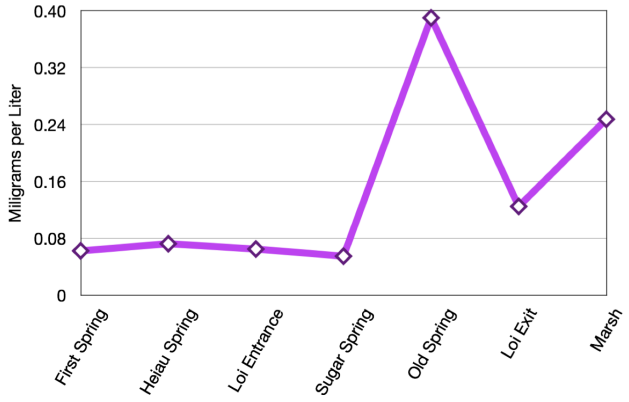

Figure 1. Ammonia (NH3) Levels According to Site. Figure 1 shows an overall trend of increasing ammonia levels as you descend the heiau. However, due to the amount of decaying plant debris in the "old spring" site, it shows an abnormally high level of ammonia.

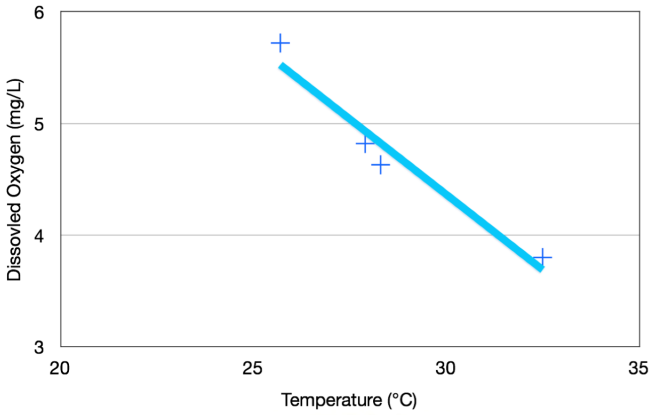

Figure 2. Temperature vs. Dissolved Oxygen in Marsh Across a 4-day Period. Figure 2 shows the daily rate of temperature vs. dissolved oxygen in the marsh. The higher the temperature the lower the oxygen content.

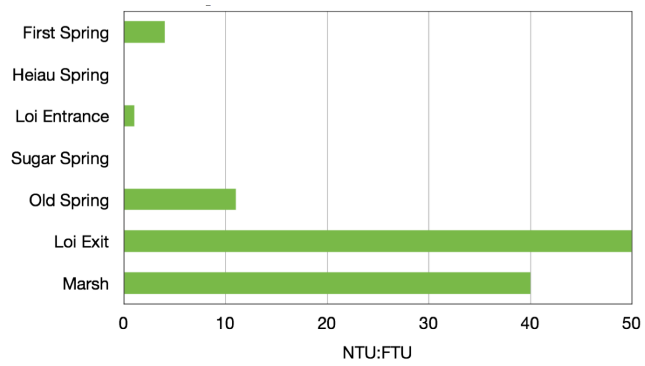

Figure 3. Turbidity Levels According to Site. ***Figure 3*** shows how as water moves down the heiau, it collects particulates which then accumulate in the marsh.

CONCLUSIONS

These baseline studies are important to see how water quality changes over time. The data collected will help determine the overall well-being of the heiau.

According to the data collected, and using the water quality standards of AECOS Inc., all sites except for the old spring are sustainable for kalo as well as other native species of plants and animals. Also, according to the data collected, and using the water quality standards of AECOS Inc., 3 out of the 7 sites--Old Spring, Loʻi Exit, and Marsh--contain high levels of ammonia (NH3) which may be detrimental to the survival of fish.

LITERATURE CITED

"Hawaii State Parks." Dept. of Land & Natural Resources, n.d. Web. 3 Jul 2012. <http://www.hawaiistateparks.org>

"Measuring Water Quality." .AECOS Inc., n.d. Web 3 Jul 2012. <http://www.aecos.com/CPIE/watR-qual.html>

ACKNOWLEDGEMENTS

We would like to thank Mrs. Keolani Noa and the STEM program for allowing us to have this opportunity, Mackenzie Manning for giving us the tools to expand our knowledge of water quality and our overall experience, Kepoʻo Noa for his assistance during data collection, and finally Doc Burrows for introducing us to Kawainui Marsh, home to Ulupo Heiau.

Uncovering the science behind the legend of Ka‘au crater’s red spring

By Melanie Keliipuleole (*Faculty Mentor*: Mackenzie Manning)

INTRODUCTION

In Hawaiian culture there are many mo‘olelo (stories) about waters running red after a battle or a death. Within the Waikiki ahupua‘a (a traditional Hawaiian division of land extending from mountain to sea), there is a mo‘olelo that tells of a spring that runs red due to a great battle between the demi-god Kamapua‘a, and the great roster, Ka‘auhelumoa:

Ka‘auhelumoa’s Spring

“This cock, (Kaauhelumoa) according to legend, was a supernatural being. He was reared by his grandmother Kanihomauole in Palolo. Kamapuaa (half man, half pig, demi-god) came before his grandmother Kanihomauole and said, “I have come to kill Kaauhelumoa and eat him.” Kanihomauole replied, “Whatever you kill you must eat, Kamapuaa.” Kamapuaa went to bite the cock. The cock flew to the right side of the hog’s back and began to peck and kick, The pig felt the pain and rolled in the dust. The cock lit on the ground. He did not make the cock go backwards, but the cock fell into the spring and died in it. It became known by the name of kaauhelumoa. The strange thing about this spring is that it looks as though reddened with blood. If you put some of it in a bottle for a souvenir, your joy will be gone for it will change to the color of ordinary water”(Sterling, Summers, & Bishop Museum 277).

My project seeks to identify the biological and/or chemical factor(s) that may be contributing to the red color of the spring waters. Possible factors that are being investigated include: photosynthetic bacteria or algae, iron levels, tannins, and turbidity. I hope to lend support to the mo‘olelo through science.

MATERIALS & METHODS

Samples were taken in November, January, and March from two different springs in Ka‘au crater, and two waterfalls along the trail leading to the crater. Water was collected for iron, tannin, and turbidity analysis (by means of a LaMotte spectrophotometer), and oxygen, conductivity, temperature, and pH levels were taken using YSI meters. Plankton tows and macroalgae samples were also collected for examination.

Above, from Left to Right: Tool used for plankton tow, LaMotte meter with Tannin & Iron reagents, pH meter, and YSI meter (***bottom***).

Below: Map of Collection Sites.

RESULTS

Figure 1. pH levels per site grouped by collection time.

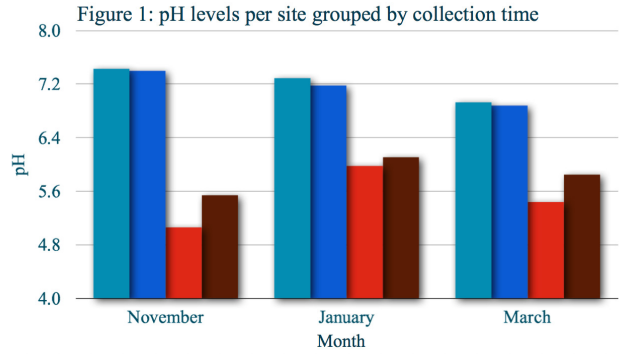

Figure 2. Temperature levels per site grouped by collection time.

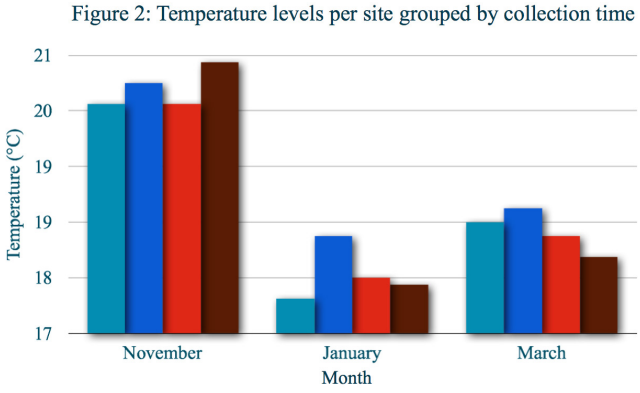

Figure 3.Tannin levels per site grouped by collection time.

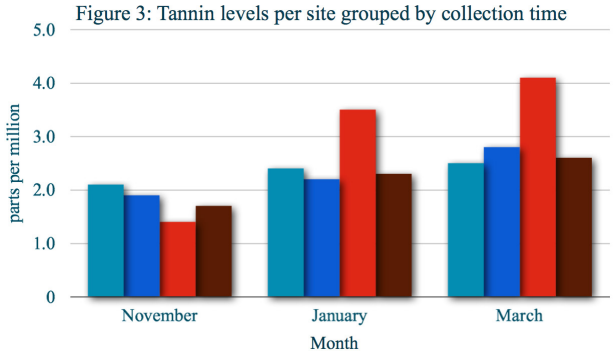

Figure 4. Iron levels per site grouped by collection time.

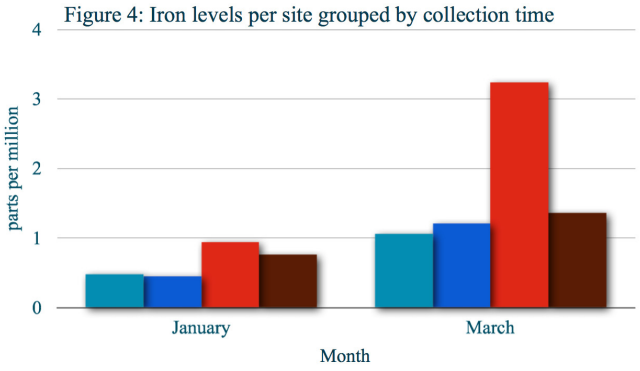

Figure 5. Turbidity levels per site grouped by collection time.

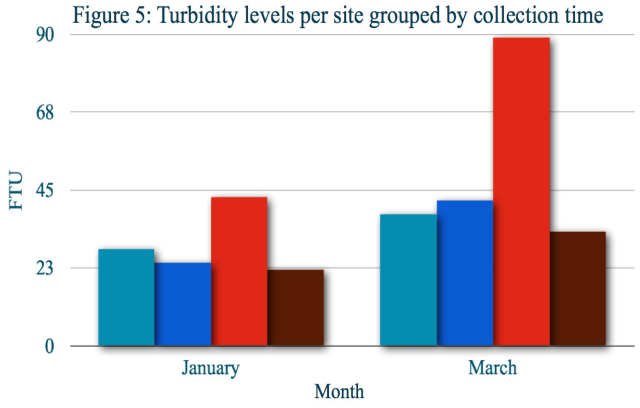

Photo Top Row. Tannin color-metric test by site.
Bottom Row. Iron color-metric test by site.

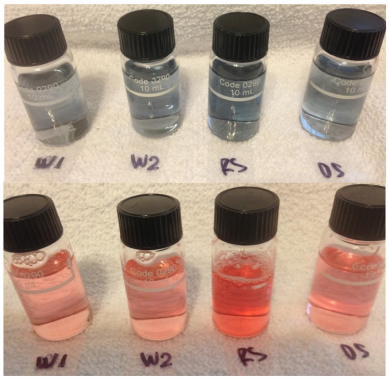

Legend
1st Waterfall
2nd Waterfall
Red Spring
Dark Spring

	January			March		
	DO (mg/L)	DO (%)	Conductivity (µS)	DO (mg/L)	DO (%)	Conductivity (µS)
First Waterfall	7.75	83.2	66.1	4.60	64.1	80.4
Second Waterfall	7.54	80.5	68.8	7.00	75.0	76.3
Red Spring	5.01	54.8	58.0	4.15	41.9	75.3
Dark Spring	4.41	42.5	58.0	0.85	9.1	76.7

Table 1 Above. YSI measurements per site in January & March.

Photo Below: Collecting YSI measurements at the Dark Spring.

Based on the data collected so far, the iron levels may be the cause of the water turning red. According to the Illinois Department of Health, "as little as 0.3mg/L is enough to turn water a reddish brown color", and the data shows to have a significant amount of iron; equalling to more than 0.9 mg/L in January, and more than 3.2 mg/L in March.

It is important to note that based on observations, although the iron level was much higher in March, the water color was much more red in January. This discrepancy may have to do with the pH levels. According to Lenntech, iron is more soluble in lower pH levels, which would explain why the water looked less red in March than in January even though it had a much higher iron content. Along with the pH levels, it is also possible that turbidity and tannins played a part in the water color difference. Based on the data March had higher tannin & turbidity levels, which could lead to color changes in the water.

As a significant trend has not yet been found, more studies of this site would be beneficial to my task of unearthing the science behind the mo'olelo of the red spring.

LITERATURE CITED

"Hawaii State Parks." Dept. of Land & Natural Resources, n.d. Web. 3 Jul 2012. <http://www.hawaiistateparks.org>

"Measuring Water Quality." .AECOS Inc., n.d. Web 3 Jul 2012. <http://www.aecos.com/CPIE/watR-qual.html>

ACKNOWLEDGEMENTS

This project was conducted through Kapi'olani Community College's STEM program. Support was lent by STEM faculty, specifically Mackenzie Manning & Mrs. Keolani Noa.

Ka noho ana o ka Lepelepeohina
(What is the habitat preference of Lepelepeohina)

By Bradley W. Hughes (*Faculty Mentor*: Kahelelani Clark, MA)

INTRODUCTION

Vanessa tameamea is one of two species of butterfly that are endemic to Hawaii. Hawaiians originally referred to *V. tameamea* as "lepelepeohina." Lepelepeohina was the first butterfly species from Hawaii to be described by western scientists but has long been culturally significant to the Hawaiian people (Gorelick and Wielgus, 1968). The introduction of invasive species to Hawai'i has led to increased habitat loss for Lepelepeohina . This threat poses a serious problem for the health of Lepelepeohina populations in the wild whose numbers are dwindling. Few studies have focused on the relationship between this species of butterfly and their plant host species. It is for this reason that I chose to investigate the unique interactions between Lepelepeohina and their host species as well as the connection between Hawaiians and these species. Adult V. *tameamea* are known to feed on Koa (*Acacia koa*) sap, but lays its eggs and feeds on Mamaki (*Pipturus albidus*) as a caterpillar. This study will focus on the habitat preferences and behavioral interaction of Lepelepeohina and various plant species in the Tantalus area on the island of O'ahu, Hawai'i.

Koa Sap **(Photo credit**: http://upload.wikimedia.org/wikipedia/commons/8/8f/Koa_sap.JPG.)

Hawaiian Perspective on Lepelepeohina

Lepelepeohina is most commonly referred to as the Kamehameha butterfly. In most Hawaiian text it is called Lepelepeohina. In the Kumulipo there is reference in the third era second verse.

> Hanau ka Peelua ka makua
> Puka kana keiki he Pulelehua, lele
> Born the caterpillar parent;
> Came his child a butterfly, flew;

The Kolea visits these islands during the winter months. Butterflies are known to frequent Mamaki trees during these months. There is a story that speaks of Lepelepeohina talking to Kolea: "I kekahi kakahiaka, e lele ana keahi lepelepeohina mai kekahi pua a i kekahi, halawai mai la kekahi Kolea…" (Ka Elele Hawaii. Buke 4, Pepa 3, Aoao 9. Iune 22, 1848.22 Iune 1848, HE OLELO NANE KA HAAHEO). Roughly translated, it is a conversation between the two species, and the Lepelepeohina is giving advice to the Kolea. It is possible that this nane hints at an observed co-dependence that perhaps deeply connects these two species.

Another story speaks of Lepelepeohina visiting a number of different flowering plants other than Koa and Mamaki such as Uala and Aeae:

> ... ua like no ko lakou ano me ko ka lepelepeohina. Lele aku no lakou ma na pua kowali, a me na pua uala, a me na pua e ae, a hoo aku i ka umiumi iloko o ka pua e omo ai i

Life Cycle of Lepelepeohina

1. Egg. Lepelepeohina eggs are laid underneath the leaves of the Mamaki. (**Photo credits:** Forest & Kim Starr [***Mamaki***]; and Li‘ula Mahi, Amy Greenwell Ethnobotanical Garden [***egg***].

2. Caterpillar. Larvae live and feed nocturnally on Mamaki during the caterpillar stage. It has been observed rolling itself up in the leaves of the host species for protection from predators. The caterpillar feeds on Makaki until it is very plump then spins its chrysalis on the under side of a leaf. (**Photo credit:** Pete Oboyski [***caterpillar***].)

3. Chrysalis. The chrysalis is spun in about 24 hours,. This stage lasts an average of 2 weeks. (**Photo credit:** Li‘ula Mahi, Amy Greenwell Ethnobotanical Garden [***chrysalis***].)

4. Butterfly. After spending 7 to 14 days in its chrysalis the Lepelepeohina emerges as a adult butterfly. At this point the Lepelepeohina is vulnerable with its wings still drying and unable to fly. Furthermore this species lives on average between 2-4weeks as a adult. (**Photo credits:** Bradley Hughes [***butterfly***]; Koa sap credit, see page 17.)

ka wai momona o na pua." (KE ALAULA. Buke II, Helu 2, Aoao 5. Mei 1867.1 Mei 1867, KA LEPELEPEOHINA)

The flying between these species may suggest that Lepelepeohina is a possible pollinator whose population numbers could be connected to the seasons in which these flowers bloom.

METHODS

- Three proposed observation sites that have host species Mamaki with Koa in close proximity. Sites will be taken from a 1992 Tabashnik et al study done at Tantalus.
- Sites will be connected with culture significance of ahupuaa.
- I will Geotag each field site using Global positioning system (GPS) and Geotag each location and overlay onto google earth.
- Data for the following will be collected to characterize each field site that the Lepelepeohina is found:

Ambient temperature will be measured using iButton temperature loggers.

Wind speed–an anemometer will be used to measure the intensity of the wind.

Radiation–light meter will be used to determine average sunlight exposure.

Soil composition–soil samples will be collected near known and prospective host species.

Diversity and density of plants–plants within the field sites will be identified and mapped using Global Information System (GIS).

Document species interaction/behavior–digital recordings of Lepelepeohina in its immediate environment to observe behavior.

DISCUSSION

In searching for information about the Vanessa tameamea, I found it referenced as the Lepelepeohina. The name itself I found to be very interesting both historically and culturally. I hope to better understand

Fig. 1. Map of Tantalus area on the island of O'ahu

this species scientifically and culturally. I hope that we can be more aware of the Lepelepeohina and its status in the wild as this was an area lacking in my initial research. My personal hope is to see this species survive and thrive. Knowledge of the Lepelepeohina can be used as a tool for education of future generations. With the data I collect I hope to use it to create Butterfly garden with the best host species for the Lepelepeohina to live and interact. This garden would be an area of endemic and indigenous flora and fauna. I also hope that this research will be furthered and used as a tool for curriculum at this garden. I am searching for the best possible home for this butterfly and hope to recreate it. There are many questions culturally I would also like to see brought to light about the connection of species. I hope to talk to Kupuna and cultural experts on the species in general, they are the real experts on questions that sometimes cannot be answered.

LITERATURE CITED

Gorelilck, G.A. & R.S. Wielgus. 1968. Notes and observations on the biology and host preferences of Vanessa tamehameha (Nymphalidae). Journ. Lepidopterists' Society.

Leeper, J.R. 1975. Hawaii's Kamehameha butterfly. Insect World Digest. Nov/Dec. 16-18.

Riotte, J.C.E. & G.Uchida. 1978. Butterflies of the Hawaiian Islands according to the stand of late 1976. J.Res.Lepid. 17: 33-39.

Tabashnik, B.E., et al. 1992. Population ecology of the Kamehameha butterfly (Lepidoptera: Nymphalidae). Ann. Entomol. Soc. Am. 85(3):282-285.

Williams, F. 1928. The Kamehameha butterfly, Vanessa tameameha Esch. Proc.Hawaii.Entomol. Soc. 7(1): 164-169.

Zimmerman, E.C. 1958. Insects of Hawaii. Macrolepidoptera. Vol.7: 463-472. U.H. Press, Honolulu.

ACKNOWLEDGEMENTS

Aunty Keolani Noa, Nari Okui, Patricia Cockett, Kahelelani Clark, Sheperd Meyers.

Effect of Strawberry Guava on the Native Land Snail *Leptachatina cerealis*

By Kaile Costa (*Faculty Mentor*: Dr. Daniel Chung)

INTRODUCTION

Leptachatina cerealis is a member of the endemic Hawaiian land snail family *Amastridae* which has 325 named species (Cowie et al.,1995) that are all in danger of extinction. In the past 30 years, fewer than 20 living species have been seen by observers in the field (personal communication, D.Chung).

Photo Credit: Daniel Chung

This decline is due to various factors; the most important being introduced species and habitat destruction. Chung has noticed that the native ground snails are very rare in areas of strawberry guava (*Psidium cattleianum*) infestation. This study looked at the effects of feeding strawberry guava leaves on the survivorship, weight and egg laying of *L. cerealis*.

PURPOSE

Conservation implications of strawberry guava leaf diet on the land snail *Leptachatina cerealis*.

METHODS

Snails came from a lab population of 200 individuals, They were placed in four boxes given different feeding regimes:

- **Box 1**: 100% mamaki leaves (P*ipturus albidus*), the snail's preferred food in the wild
- **Box 2**: 100% strawberry guava leaves
- **Box 3**: 2/3 mamaki +1/3 strawberry guava
- **Box 4**: 1/3 mamaki + 2/3 strawberry guava.

Each box began with 10 adults, 10 juveniles and a few neonates. Boxes were lined with moist paper towel, and the total leaf area in each boxwas 81 cm^2 (Leaves cut into 9cm X9 cm). Intervals between feedings were 7 - 14 days; boxes were stored at 64-67º F.

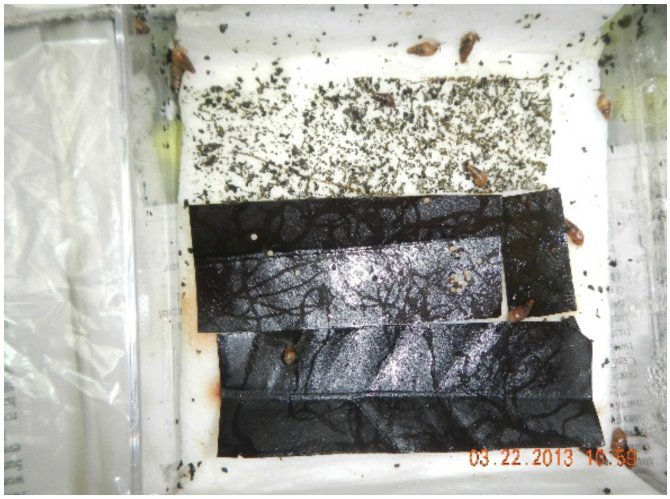

RESULTS

Boxes (different diets) showed differences in survivorship, cumulative number of eggs laid and neonates hatched. The three graphs that follow illustrate the results.

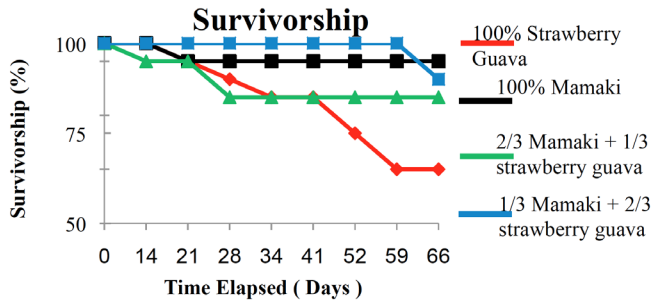

Graph 1. Survivorship

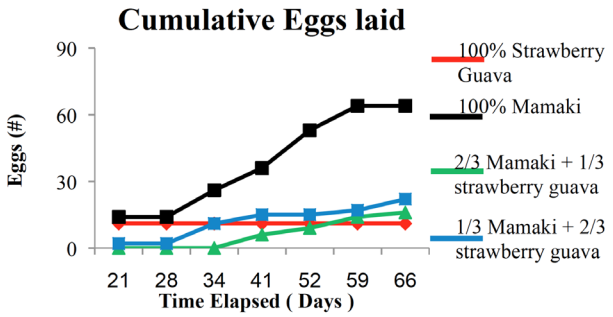

Graph 2. Cumulative Eggs Laid

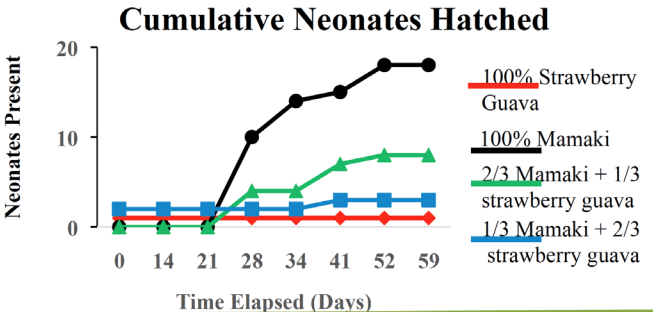

Graph 3. Cumulative Neonates Hatched

DISCUSSION AND CONCLUSIONS

Snails fed strawberry guava leaves stopped all reproduction early in the experiment, while snails fed their preferred diet of mamaki leaves had the highest reproduction, and snails fed mixed diets had intermediate levels of reproduction in terms of number of eggs laid and total neonates hatched.

Survivorship was lowest for snails fed only strawberry guava leaves and was highest for snails fed their preferred diet of mamaki leaves, while those fed mostly strawberry guava leaves with some mamaki leaves showed intermediate survivorship.

Results indicate the *Leptachatina cerealis* living in strawberry guava infestations with no mamaki or other native plants they feed on will die out due to complete lack of reproduction, unless they are replenished by migration from a nearby colony outside of strawberry guava forest.

Since strawberry guava is one of the most serious invasive weeds in Hawai‘i (Smith, 1985), replacing native forest with strawberry guava monocultures, the spread of strawberry guava is a serious threat to the survival of this species and perhaps the entire endemic family Amastridae. The spread of strawberry guava may possibly account for some of the disappearance of the native ground snails of the family Amastridae

Conservation of this species and other native amastrids will require strawberry guava control. Other serious invasive plants, like Cinnamomum burmannii, that appear to adversely affect the native snails must also be controlled for the snails to have a chance at survival.

Photo Credit: Daniel Chung

LITERATURE CITED

Cowie, R. et al., 1995. Catalog of the Native Land and Freshwater Molluscs of the Hawaiian Islands. Backhuys Publishers. Leiden. 248 pp.

Smith, C. 1985. Impact of Alien Plants on Hawaii's Native Biota. In: Charles Stone and J. M. Scott. Hawaii's Terrestrial Ecosystems Preservation and Management. Cooperative National Park Resources Studies Unit. University of Hawaii. Pages 180-243.

State of Hawai‘i Department of Agriculture, comp."Biocontrol of Strawberry Guava by Its Natural Control Agent for Preservation of Native Forests in the Hawaiian Islands." (n.d.): n. pag. 2010. Web. 1 May 2013.

ACKNOWLEDGEMENTS

EPSCoR HAWAI‘I
A Program Administered by the University of Hawai‘i System
NSF
SACNAS
UH ‘ILIMA CHAPTER

Tissue nutrient pools and growth rates of the opportunistic alga U*lva spp*. on Hawaii's leeward coast

By Kanoelani Steward (*Faculty Mentor*: Bruce Dudley, Ph.D.)

INTRODUCTION

Ulva spp. was used as a bioindicator to investigate changes in nutrient availability caused by Kiawe (*Prosopis pallida*) stands in the adjacent marine waters. More specifically, tissue nitrogen pools were measured to analyze changes in concentrations due to Kiawe stands. Additionally, growth rates of *Ulva spp.* were examined in response to variations in seawater nitrogen and phosphorus concentrations.

OBJECTIVE

The aim of this study is to evaluate the nutrient availability on the Kona coast of Hawaii Island and to determine the effects of increases in nutrient concentrations on the growth rates of *Ulva spp.*

METHODS

To evaluate the nutrient availability, seawater conditions were characterized by using a YSI meter to measure dissolved oxygen (mg/L & %), salinity (ppt), conductivity (ms), and temperature (°C). Seawater samples were also collected and analyzed for nutrient concentrations for nitrate, ammonium, and phosphate.

Photo 1 (above). YSI Meter.

***Photo 2* (*right*).** Acid-washed syringe with Whatman GF/F filter and polyethylene vials.

To observe the effects of the altered algal physiology, tissue nitrogen pools were measured by collecting samples of *Ulva spp*. and analyzing it at the UH Hilo analytical lab. To see how physical and chemical conditions altered the growth of *Ulva spp*., metal cages were constructed with ~2g of *Ulva spp*. secured within the rope.

RESULTS

The total inorganic nitrogen (TIN) (µM) was measured by thermal combustion and the average TIN was compared against various variables to evaluate the nutrient availability and algal growth rate.

Photo 3. Collecting samples of *Ulva spp*.

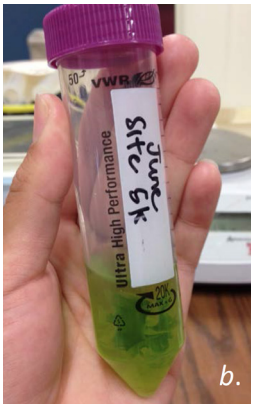

Photo 4. *Ulva spp*. in a methanol:dimethylsulphoxide solution of 4:1 for chlorophyll extraction.

Photo 5. *Ulva spp*. within the rope attached to a metal cage.

Photo 6. Metal cage deployed and submerged at Kiholo;

Photo 7. Metal cage

Graph A. No significant difference between the sites with Kiawe stands and the control sites, without Kiawe stands.

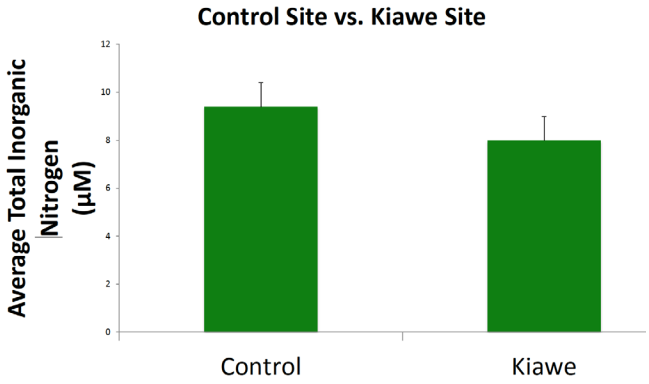

Graphs B and C. In areas where there were low levels of salinity, there were high amounts of nitrogen in the seawater.

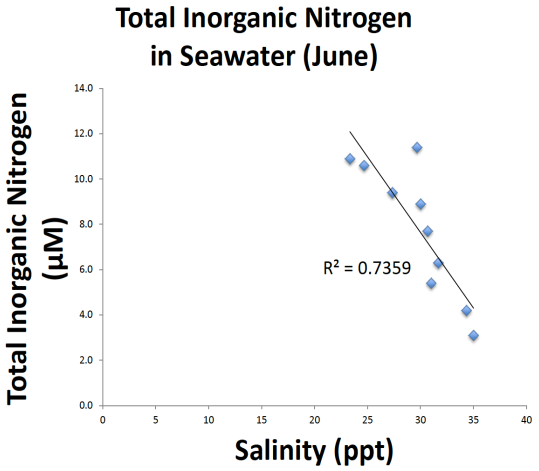

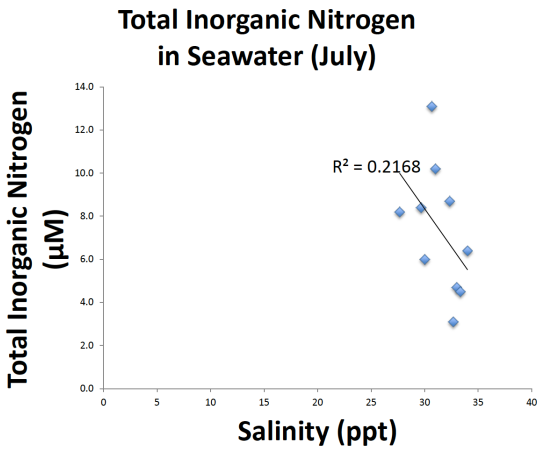

Graph D. As nitrogen increases in the seawater, the total chlorophyll content within the algal also increases.

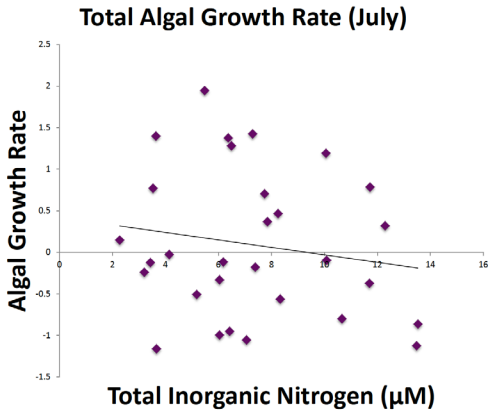

Graph E. No significant correlation between the nitrogen in the seawater and the algal growth rate.

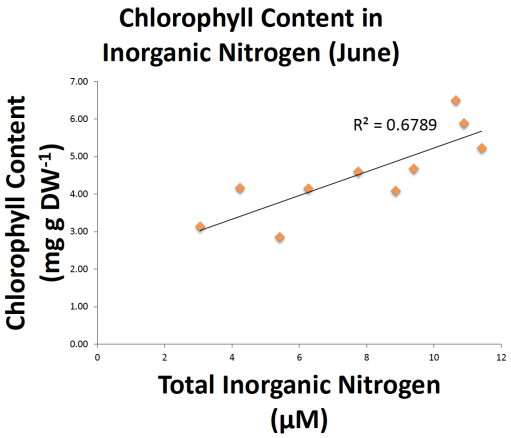

CONCLUSION

Results show that when salinity was low, there was a higher concentration of nitrogen (***Graph B and C***), suggesting that Kiawe stands are not a major source of nitrogen for *Ulva spp*. (***Graph A***). Since there was no significant algal growth rate (***Graph D***) in July, perhaps the climate was too hot and arid, decreasing the population of *Ulva spp*. and hindering its algal growth (***Photo 8***). As a result, light and temperature may be the limiting factors of growth during the summer and nutrients, or more specifically nitrogen, could be the limiting factor(s) during the spring (***Photo 9***).

Photo 8. Taken during the summer (June 2012), there was a low abundance of *Ulva spp*. at a particular site in Kiholo Bay. (**Photo Credit**: K. Steward)

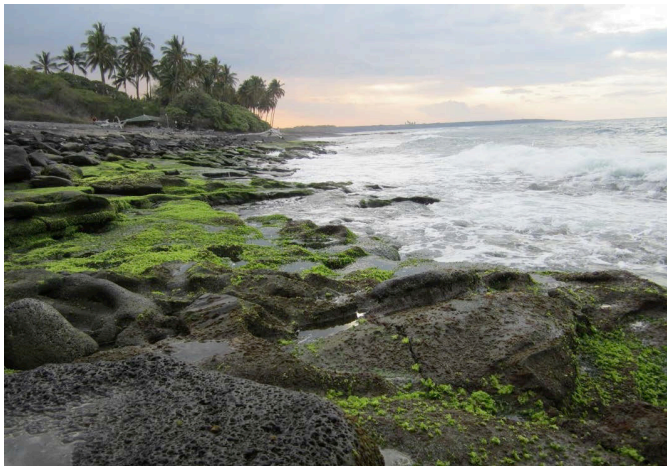

Photo 9. Taken during the spring (February 2012), there was a high abundance of *Ulva spp*. at the same site in Kiholo Bay. (**Photo Credit**: B. Dudley)

DISCUSSION

As coastal development increases, nutrient concentrations will likely increase as well, giving *Ulva spp*. a competitive advantage in high- nutrient environments. This increase may cause a shift in species composition, moving towards species with faster nutrient uptake and growth rates. These faster growing species may also have a greater probability of outcompeting those species that are slow growing, and consequently, will dominate the entire habitat.

FUTURE RESEARCH

Deploying metal cages with *Ulva spp*. during cooler months of the year (February-April) to observe increased probable growth rates. Furthermore, characterizing the community composition of the intertidal zones to observe any shift in species composition due to increased amounts of nitrogen.

LITERATURE CITED

Barr, N. G. 2007. Aspects of nitrogen metabolism in the green alga *Ulva*; Developing an indication of seawater nitrogen loading. PhD thesis, University of Auckland.

Barr, N. G. and Rees, T. A. 2003. Nitrogen status and metabolism in the green seaweed Enteromorpha intestinalis: an examination of three natural populations. Marine Ecology Progress Series 249: 133-144.

Luo, M. B., Liu, F., and Xu, Z. L. 2012. Growth and nutrient uptake capacity of two-occurring species, *Ulva prolifera* and *Ulva linza*. Aquatic Botany 100: 18-24.

Wallentinus, I. 1984. Comparisons of nutrient uptake rates for Baltic macroalgae with different thallus morphologies. Marine Biology 80: 215-225.

ACKNOWLEDGEMENTS

Mahalo to the Pacific Internship Programs for Exploring Science (PIPES), UH Hilo Marine Science Department, and Kapiolani Community College STEM Program for institutional support. Funding was provided by NSF EPSCoR. This material is based upon work supported by the NSF. Any opinions, findings, and conclusions or recommendations expressed in this material are those of the author(s) and do not necessarily reflect the views of the NSF.

Thermal Tolerances of Four Littoral Gastropods: Honolulu, Hawaii

By Patricia M. Cockett (*Faculty Mentor*: Wendy A. Kuntz, Ph.D.)

ABSTRACT

Invertebrates and algae that occur within the littoral zone of Hawaii must tolerate extreme envirorunental stressors. In mid-sununer temperatures experienced by littoral organisms vary from 25° C to 45° C. Such extreme conditions have lead experts to believe that the heat shock protein (HSP) genes of some littoral gastropods are constitutive and that the organisms tend to live near their uppermost temperature tolerances. The Intergovernmental Panel on Climate Change (IPCC) suggests that average surface temperatures may increase between 2° C and 6° C by the end of the 21st century (***figure 1***).

The intertidal zone of Hawaii is a prominent food source for native Hawaiians and holds much cultural significance. It is important for the welfare of native Hawaiian people that we understand the relationship of intertidal gastropods with their surrounding habitat. I examined thermal tolerances for four ittertidal gastropods in Hawaii: *Littoraria pintado*, *Siphonaria normalis*, *Nerita picea*,and *Morula granulata*. These four gastropods occupy separate niches that extend from the uppermost portions of the littoral zone down to the low tide marks. Naturally occurringtemperatures in the separate niches of the gastropods were documented using digital temperature loggers and infrared thermometers. Lethal temperatures of the four gastropods were then compared to the naturally occurring temperatures and confirmed that they live a their uppermost limits.

INTRODUCTION

Invertebrates and algae that occur within the littoral zone in Hawaii must tolerate extreme environmental stressors (Sanford, 2002). Lars Tomanek (2009) suggested that organisms in the littoral zone live close to their thermal limits and a rise in temperature of a few degrees Celsius could be lethal. The Intergovernmental Panel on Climate Change (IPCC) presented possible surface temperature changes and stated that average surface temperatures could rise between 2° C and 6° C by the end of the 21st century. Organisms living in the littoral zone were once a prominent source of food for native Hawaiians and it is of great cultural importance that we understand the response of intertidal conununities to changes in the environment like those associated with climate change.

Rates of biochemical reactions in organisms are directly influenced by temperature and moisture (Menge

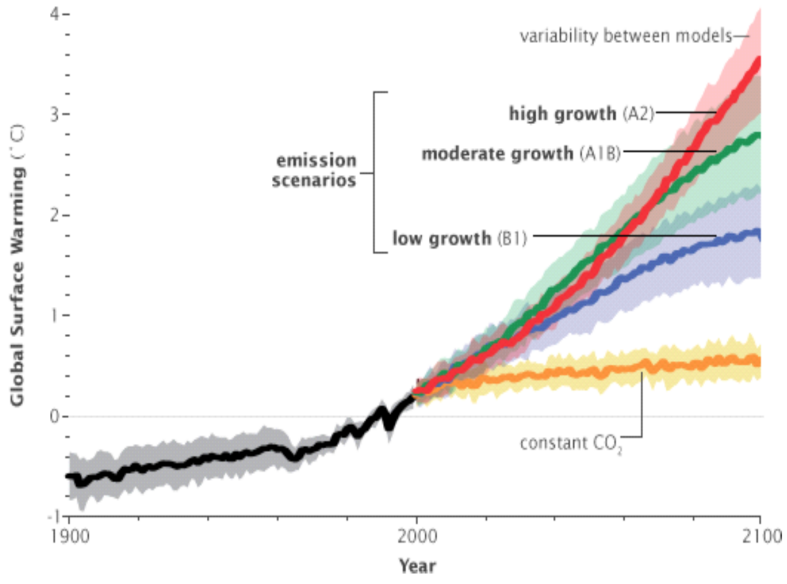

Figure 1
Model simulations by the Intergovernmental Panel on Climate Change (IPCC) show that average surface temperatures could rise between 2° C and 6° C by the end of the 21st century.

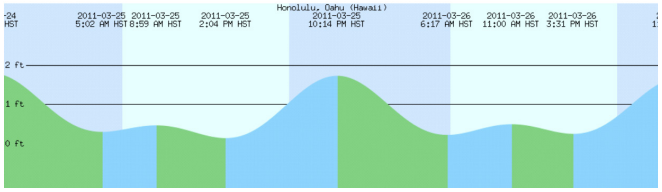

Figure 2. The tide table for Honolulu, Hawai'i, on March 26, 2011.

and Sutherland, 1987). During low tides, invertebrates living in the upper littoral zone must tolerate longer periods of exposure to heat from the sun and desiccation in the absence of splashing waves when compared to the lower littoral zone (Sanford 2002). Littoral organisms have traits that have evolved for the harsh environment in which they live; however, high and low temperatures have lethal effects on organisms (Menge and Sutherland, 1987). The *Littoraria pintado*, *Nerita picea, Siphonaria normalis* and the *Morula granulata* are four gastropods that exist at different levels of the littoral zone in Hawaii. l.pintadooccurs at the highest points of the littoral zone.

S. normalis dwells above the low tide line with the N .picea just below them in overlapping habitats (Kay 1979). The *M. granulata* can be found in the lower littoral zone, in tide pools, and on bio-covered benches (Kay 1979). The elevations in which these organisms live make them prime candidates for testing thermal tolerances because each elevation experiences different temperatures throughout the day. I hypothesized that the gastropods will not survive temperatures that exceed those of their natural environment.

METHODS

Mortality Tests. All organisms were collected the morning of each trial from Maili Point, ill. Five trials were conducted for each species. The temperatures of the incubators were set to 25° C, 41° C, 42° C, 43° C, 44° C, 47° C, 48° C, and 49° C respectively.

Ten individuals of each species were placed in separate petri dishes and left in each incubator for five hours. Five hours represents the maximum time that the organisms could possibly be exposed to higher temperatures. After the five hour duration, the gastropods were placed in a glass dish containing filtered sea water. I determined their mortality by the presence or absence of righting behavior (see ***Figure 4***).

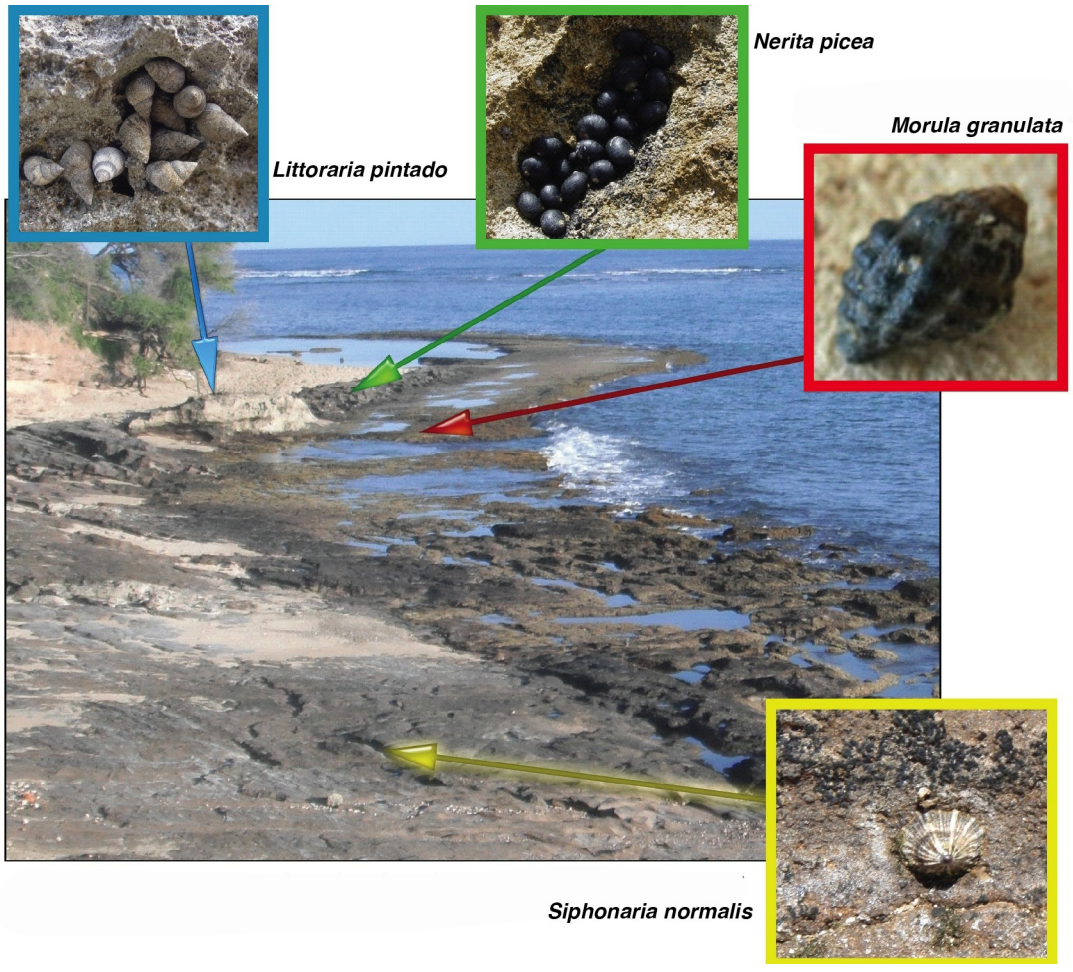

Figure 3. The sea beach below Diamond Head. Each arrow points to the relative habitat of each species.

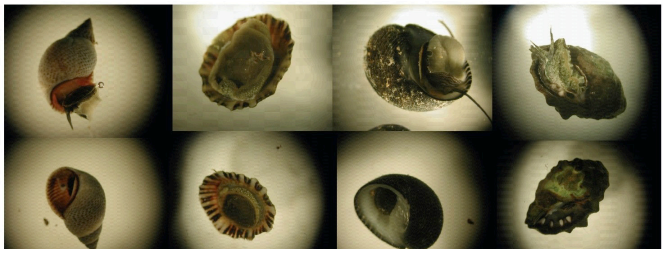

Figure 4. The righting behavior of *L. pintado*, *S. normalis*, *N. picea*,and *M. granulata* (**top row**). The appearance of each gastropod when dead (**bottom row**).

Temperature Samples. Using temperature loggers, measurements were recorded of the substrate on which the gastropods were found. All measurements were taken from the sea bench below Diamond Head (figure 3). The temperature loggers were left out during diurnal low tides and were set to record the relative temperature once every minute.

RESULTS

- The temperature logger near the *L. pintado* had the highest recorded, followed by the *S. normalis, N. picea*, and *M. granulata* in descending order of temperatures (***figure 5***).
- The *L.pintado* was able to withstand the highest temperatures, followed by the *N. picea*, *S. normalis*, and *M. granulata* in descending order (***table 1)***.

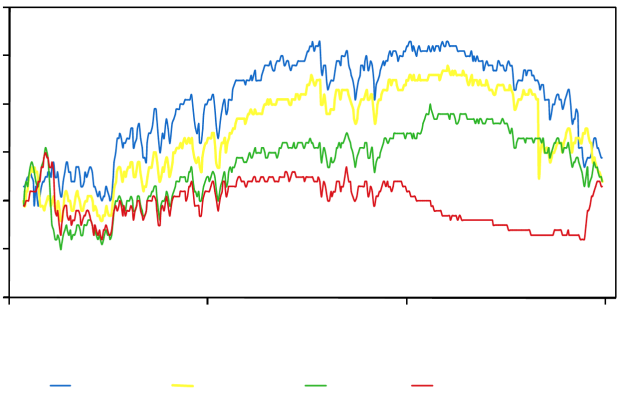

Figure 5. Recorded temperatures of the diurnal low tide at Leahi beach on March 26, 2011. Temperature loggers were attached to the substrate near a colony of each species and recorded the temperature once every minute. Blue: *L. pintado.* Yellow: *S. normalis*. Green: *N. picea*. Red: *M. granulata.*

Average Lethal Temperature (°C)	
L. pintado	**49**
S. normalis	**43.4**
N. picea	**48.6**
M. granulata	**42.8**

Table 1. The average lethal temperatures of the four littoral gastroponds.

DISCUSSION

The *L.pintado* is located in the highest portion of the littoral zone (figure 3). This species died at a slightly higher temperature than those recorded by the temperature loggers (figure 5 and table 1).

The *S. normalis* lives below the *L.pintado* (figure 3). The average lethal temperature for the *S. normalis* similar to the temperature recorded by the loggers (figure 5 and table 1). The *S. normalis* doesn't have an opercula like the other species tested and resides on a home scar during low tides (Kay 1979). It is possible that the *S. normalis* can withstand higher temperatures if sealed to their home scar.

The *N. picea* lives below the *S. normalis* and the temperatures recorded in the field are lower than those of the *S. normalis* (figures 3 and 5). The lethal temperatures, however, are much higher than the observed temperatures in the field (table l).

The *M. granulata* lives at the lowest portion of the littoral zone (figure 3). The temperatures recorded in the field are much lower than the lethal temperatures found (figure 5 and table 1).

The hypothesis that organisms in the littoral zone live close to their thermal limits is supported by the data I collected. Once surface temperatures begin to increase due to climate change, we will likely observe a decline in species of the littoral zone.

CONCLUSIONS

The *L.pintado* is located in the highest portion of the littoral zone (figure 3). This species died at a slightly higher temperature than those recorded by the temperature loggers (figure 5 and table 1).

The *S. normalis* lives below the *L.pintado* (figure 3). The average lethal temperature for the *S. normalis* is similar to the temperatures recorded by the loggers (figure 5 and table l). The *S. normalis* does not have an opercula like the other species tested and resides on a

home scar during low tides (Kay 1979). It is possible that the *S. normalis* can withstand higher temperatures if sealed to their home scar.

The *N. picea* lives below the *S. normalis* and the temperatures recorded in the field are lower than those of the *S. normalis* (figures 3 and 5). The lethal temperatures, however, are much higher than the observed temperatures in the field (table 1).

The *M. granulata* lives at the lowest portion of the littoral zone (figure 3). The temperatures recorded in the field are much lower than the lethal temperatures found (figure 5 and table l). The hypothesis that organisms in the littoral zone live close to their thermal limits is supported by the data I collected. Once surface temperatures begin to increase due to climate change, we will likely observe a decline in species of the littoral zone.

REFERENCES

Kay, E. A. 1979. Hawaiian Marine Shells: Section 4 Mollusca: Bishop Museum Press, Honolulu Hawaii.

Menge, B. A . and J. P. Sutherland. 1987. Community regulation: variation in disturbance com petition and predation in relation to environmental stress and recruitment. Am. Nat.130-5: 730-757.

Sanford, E. 2002. Water temperature, predation and the neglected role of physiological rate effects in rocky intertidal communities. Int. Comp. Biol. 42-4: 881-891.

Tomanek, L. 2010. Variation in the heat shock response and its implication for predicting the e ffect of globaal climate change on species' biogeographical distribution ranges and metabolic costs. J Esp. Bio. 213: 971-979.

Vermeij, G. J. 1971. Temperature relationships of some tropical Pacific intertidal gastropods. Marine Biology.10: 3308-314.

ACKNOWLEDGEMENTS

Mahalo nui loa to my mentor W. Kuntz, Ph.D., and M. Hadfield, Ph.D., for all your help and guidance, Mahalo to B. Nedved, Ph.D., N. Okui, S. Kao, P. Foulk, and L. Perotti, Ph.D., for all your moral fiber and mana'o. I thank EPSCoR and the Kapiolan'i Community College STEM program. I am deeply grateful to Aunty Keolani Noa for being the most wonderful person alive.

The effect of predator cues on phototaxis in *Calcinus seurati* hermit crabs

By Megan Akiko Onuma (*Faculty Mentor*: Dr. Wendy Kuntz)

ABSTRACT

Phototaxis, or movement towards or away from light, is a common henomenon in marine organisms.

The purpose of this study was to find out whether *Calcinus seurati* hermit crabs exhibit phototaxis and (2) whether the phototactic response changes when the hermit crabs are exposed to predator cues

Results indicated that (1) *C. seurati* showed significant positive phototaxis and (2) this phototactic response varied under different predatory cues.

INTRODUCTION

The rocky Hawaiian intertidal environment is characterized by areas of both intense sunlight and sheltered crevices. In mobile organisms that can behaviorally choose to occupy either of these areas natural selection may have favored the evolution of an innate preference towards dark or lit areas. Despite the wealth of research that has been done describing phototaxis in crustacean larva (Latz and Forward 1977, Webley and Connolly 2007), there is little information on photoresponses in adult hermit crabs.

The purpose of this study was to find out (1) whether *Calcinus seurati* hermit crabs exhibit phototaxis and (2) whether the phototactic response changes when the hermit crabs are exposed to predator cues.

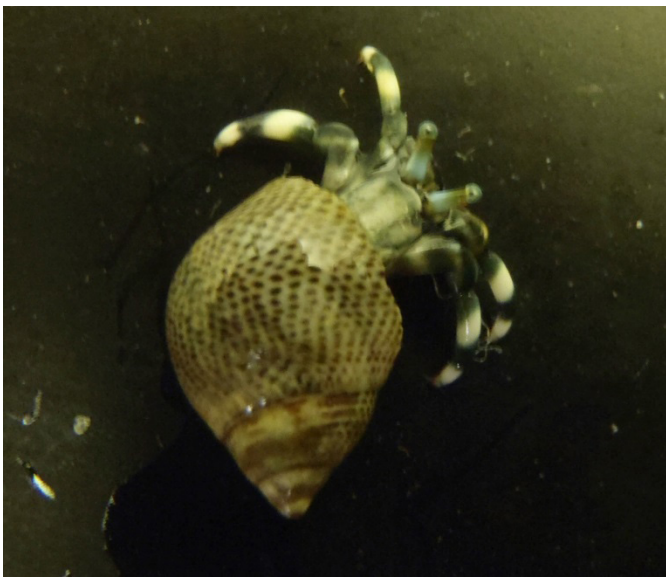

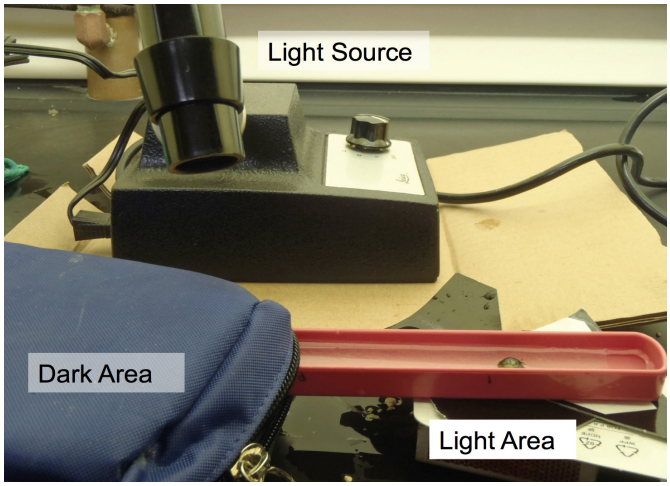

Individual *Calcinus seurati* hermit crabs were placed in a narrow container with equal access to dark and lit areas.

METHODS

I collected sixty *Calcinus seurati* hermit crabs from the tidepools of Makapu'u point on the island of O'ahu. *C. seurati* hermit crabs are well-suited for testing phototaxis because they are generally found higher up in the intertidal (Reese 1969). I placed each crab into a narrow plastic container filled with seawater, with equal access to darkened and brightly lit areas and recorded their position at 10s. I then repeated the procedure with (1) added predator crab effluent (*Carpilius maculatus*), and (2) bird predator visual cue (moving chopsticks). I used chi-square analysis to compare between groups.

RESULTS

In the first treatment, individuals showed a significant preference for the lit area (X2 test $p<0.001$). In the presence of predator crab effluent, hermit crabs preferred lit areas and did not differ significantly from seawater alone. In the presence of a bird predator cue, hermit crabs preference for lit areas declined and was significantly different from seawater alone ($p<0.001$).

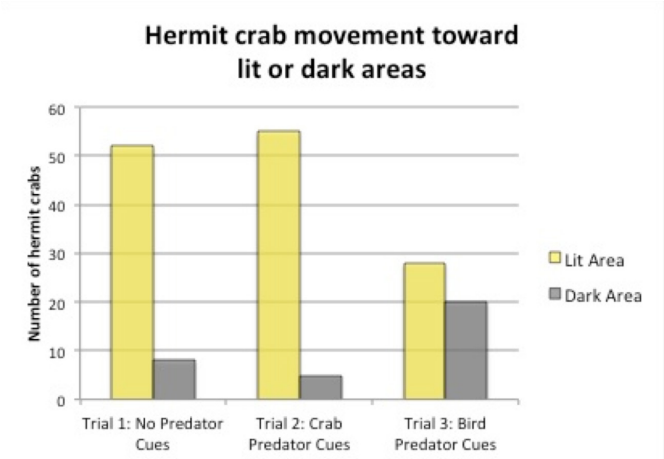

CONCLUSIONS

In this experiment, I found positve phototaxis in *C. seurati* hermit crabs. This preference for lit areas may be an adaptation indicating that light exposed areas are advantageous, perhaps in food abundance or predator evasion. The hermit crabs' behavior change in the presence of avian visual cues is likely an evolutionary response which makes the crabs seek dark, sheltered areas to avoid birds.

LITERATURE CITED

Latz, M.I., and R.B. Forward. 1977. The effect of salinity upon phototaxis and geotaxis in a larval crustacean. Biological Bulletin. 153: 163-179.

Reese, E. 1969. Behavioral adaptations of intertidal hermit crabs. American Zoologist. 2: 343-355.

Webley, J.A.C., and R.M. Connolly. 2007. Vertical movement of mud crab megalopae Scylla serrata in response to light: Doing it differently down under. Journal of Experimental Marine Biology and Ecology. 341: 196-203.

ACKNOWLEDGMENTS

This project could not have been completed without the support and encouragement of faculty advisor Dr. Wendy Kuntz, as well as help from Devan Tatemichi. Thank you.

Calcification rates of the reef building coral *Porites compressa* under different levels of pH and diel pH variation

By Megan Akiko Onuma and Christopher Jury, Hawai'i Institute of Marine Biology and Pacific Internship Program for Exploring Science (PIPES)

QUESTIONS

1. What effect does reduced mean pH have on coral calcification rates?
2. What effect does pH variability have on coral calcification rates?
3. Do treatments (1) and (2) have interactive effects?

INTRODUCTION

Studies have shown that seawater pH has measurable effects on coral growth rates (Dooney et al. 2009). Most studies focus on how reduced seawater pH affects coral calcification rates--pertinent to ocean acidification. However, almost no studies have examined the effect of different levels of pH variation on coral calcification rates.

pH variation can be seen as a product of water in-flow rate, because the metabolic processes of corals change the pH of the surrounding seawater. Low seawater in-flow rates, found in shallow reef flats, would create high pH variability ranges, as biologically induced changes to the seawater chemistry accumulate. High seawater in-flow rates, experienced in reefs exposed to the open ocean, would experience low pH variability.

We examined the effects of different levels of mean pH and of diel pH variability on the rate of coral calcification in *Porites compressa*, an endemic Hawaiian coral.

METHODS

1. Four coral nubbins from 20 colonies of *Porites compressa* were collected
2. Two levels each of pH (ambient and reduced by 0.3 pH units) and pH variation (low and high)- full factorial design with four treatments total
3. pH was reduced using CO2 bubbling
4. Different levels of pH variation were induced by varying seawater in-flow rate to each aquarium

Corals were weighed, exposed to treatments for 30 days, and then weighed again to determine growth rates.

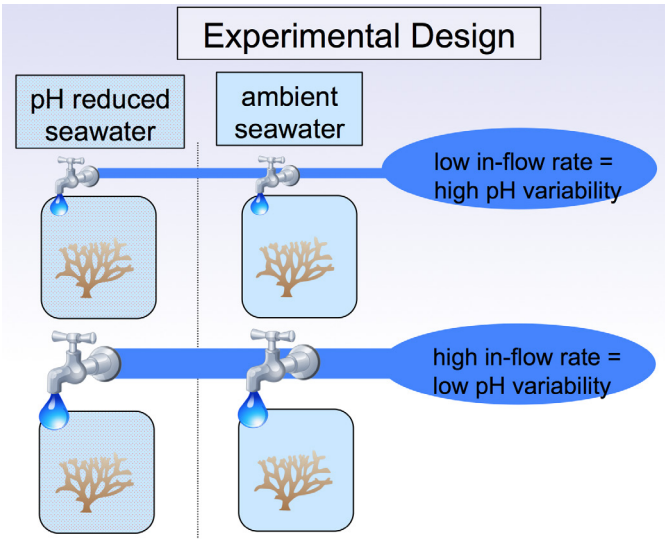

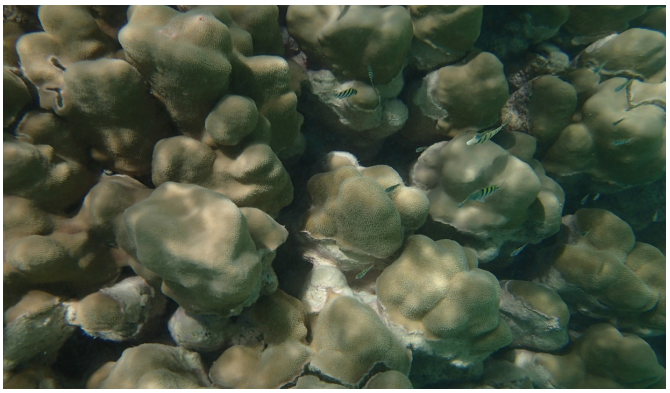

RESULTS

1. Reduced mean pH significantly decreases coral calcification rates (confirms prior studies).
2. High pH variability from low seawater in-flow rates significantly decreases coral calcification rates.
3. These two treatments do not have interactive effects.

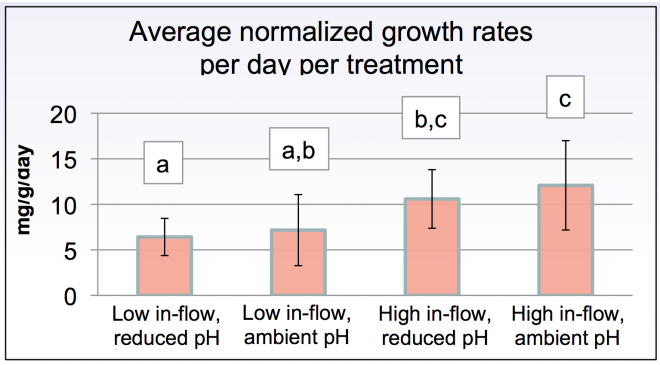

Coral calcification rates were analyzed using a 2-way ANOVA and a Tukey HSD. Both factors of pH and pH variability had a significant effect on the rate of coral calcification ($p=0.029$ and $p<0.001$, respectively).

CONCLUSIONS

Our results indicate that corals experience reduced calcification rates in low in-flow and thereby high pH variability conditions. This implies that corals living in shallow reef also experience reduced calcification rates compared to deeper slope reefs. We found no interaction effects between overall mean pH and pH variability. Temperature and nutrient availability were co-varying variables that may be controlled for in future experiments.

LITERATURE CITED

Doney, S. C., Fabry, V. J., Feely, R. A., and Kleypas, J. A. (2009). Ocean Acidification: The other CO2 Problem. The Annual Review of Marine Science, v.1, 162-192.

PHOTO CREDITS

Diana Kleine. Integration and Application Network, University of Maryland Center for Environmental Science (ian.umces.edu/imagelibrary/); Henry Hsieh.

ACKNOWLEDGEMENTS

Special thanks to Chris Jury, Dr. Paul Jokiel, Dr. Rob Toonen, Dr. Wendy Kuntz, and PIPES staff.

Mycale grandis effect on *Montipora capitata* Photophores and Auto-florescence using Laser Scanning Confocal Microscopy

By Daniel Kamohoali'i Jennings-Kam
(*Faculty Mentor*: Ruth Gates, Ph.D., Hawai'i Institute of Marine Biology)

INTRODUCTION

Scleractinian corals form coral reefs that are home to hundreds of thousands of species of plants, animals and invertebrates. NOAA estimates that in the U.S. reefs systems are commercially worth over 100 million dollars, and healthy reefs attract tourism worth billions. Reefs are also important in shielding shorelines from wave energy. Pharmaceutical compounds from coral reefs have been found and used to treat many ailments including viral and bacterial infections, arthritis and even cancer.

The goal of this project is to explore interspecies relationship between *M. capitata* and the invasive red sponge *M. grandis*.

LASER SCANNING LIVE IMAGING CONFOCAL MICROSCOPY (ZEISS LSM710)

LSM is able to measure the intensity of photophore present. By using LSM we can see individual symbiotic algae cells within live coral tissue. Two types of scans were done on the samples, 3D and Lambda. 3D gives us a nice representation of the symbiont density. Lambda gives us quantitative data in a 2D plane. The areas scanned were areas of the coral as close to the interactor as possible while incorporating live tissue.

FIELD OBSERVATIONS

M. grandis was observed commonly on *Porites compressa* and is rarely found on *M. capitata* and *Pocillopera damicornis*. The colonies of *M. capitata* with *M. grandis* were found on dead or damaged *P. compressa* colonies or on man made structures. *M. grandis* releases a red liquid when disturbed, this is most likely why the coral samples kept with *M. grandis* died within a few days.

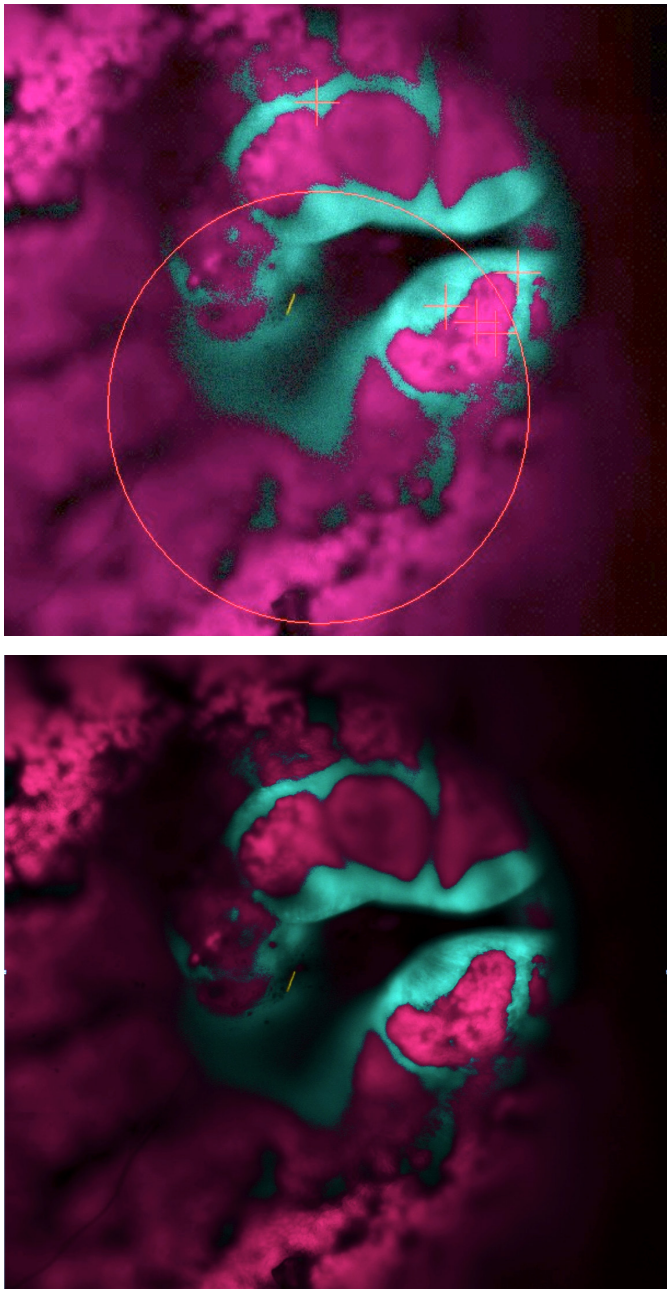

Photos above: examples of Lambda scans of *M. capitata* at 10x magnification. Top image shows quantitative data collecting by the LSM.

METHODS

A sample includes a piece of the coral colony and the site of interaction with the other organism. Control samples were defined as colonies not undergoing a relationship with a macro organism and at least one inch from the site of interaction with another organism. Three different coral species were sampled, *M. capitata*, *P. compressa*, and a *Goniastria sp*. Three different interactors on these corals were collected, *M. grandis*, *Dictyosphaeria versluysii*, and an unidentified brown algae. After preliminary testing *M. grandis* was chosen as the interactor to further pursue.

Samples were collected at Moku o Loʻe, the★ indicate the sights samples were taken. The blue squares represent the areas where corals were observed for interactions.

> ***Tables*** **(opposite page)** were all generated from lambda images of *M. capitata*. ***Tables 1*** and ***3*** are from preliminary samples from different colonies. ***Tables 2*** and ***4*** are samples gathered from the same colony.

RESULTS

Despite the preliminary study and observations of gross morphological differences in samples, *M. grandis* appears to have little to no effect on the photophores and their intensity in *M. capitata*.

> ***Images*** to the right and on page 38 are 3D Z stacks of *M. capitata* showing gross morphological and sybiont density differences.

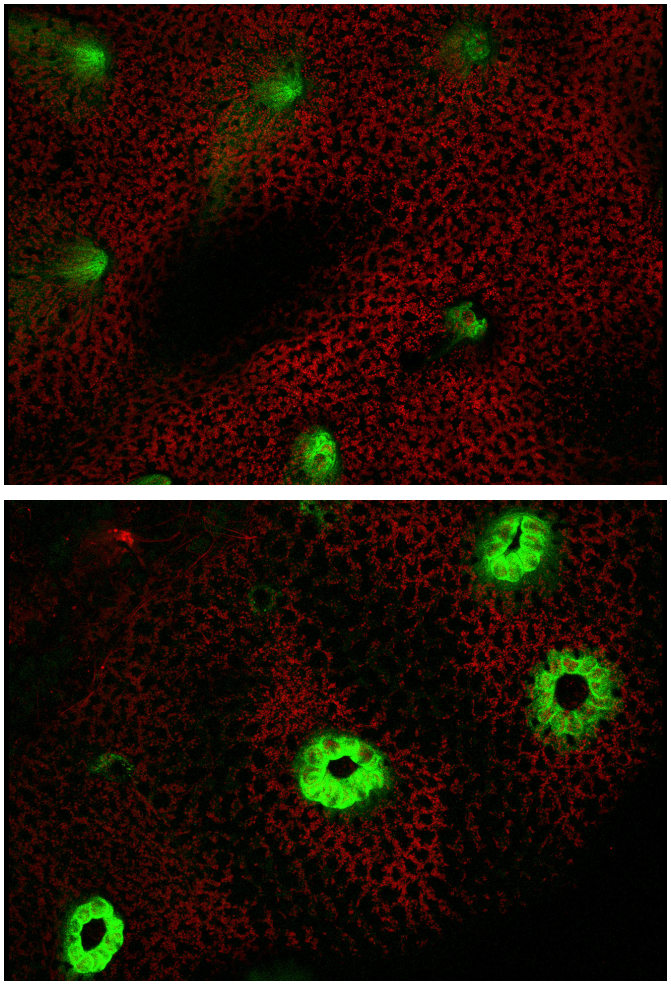

Top: Control, 2.5x
Bottom: Interacting, 2.5x

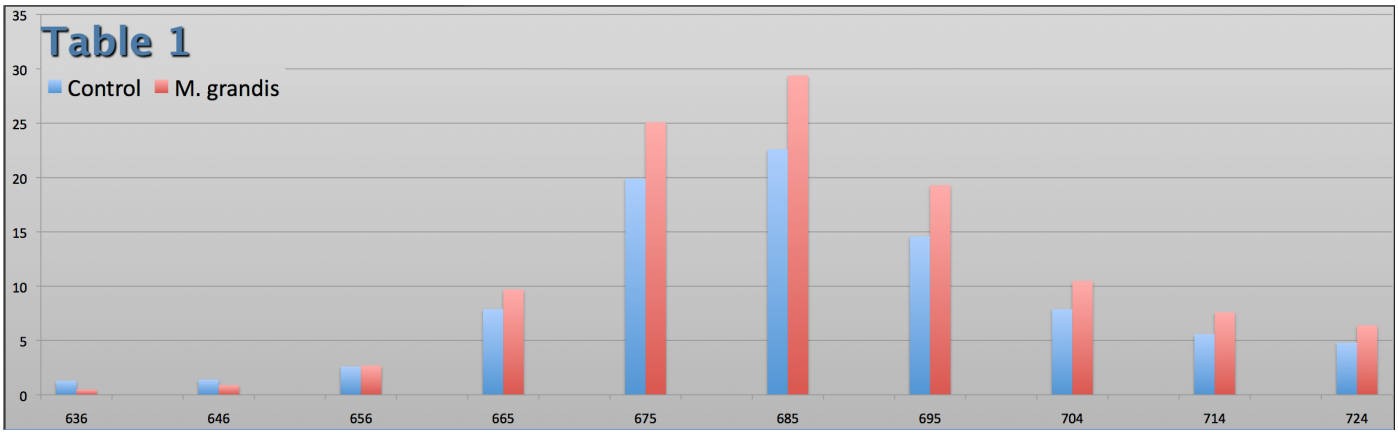
Table 1
Control
M. grandis
35
30
25
20
15
10
5
0
636
646
656
665
675
685
695
704
714
724

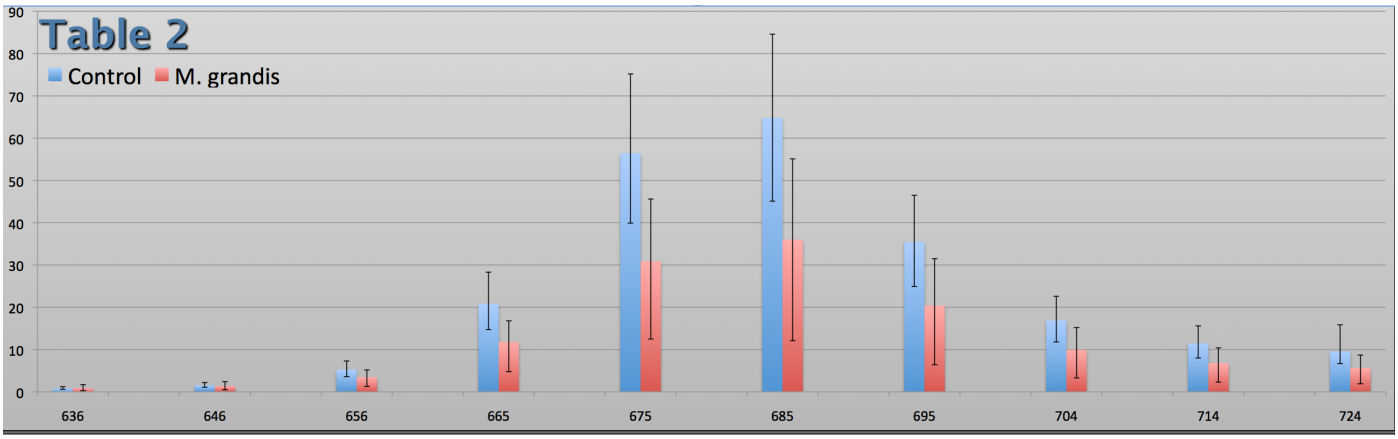
Table 2
Control
M. grandis
90
80
70
60
50
40
30
20
10
0
636
646
656
665
675
685
695
704
714
724

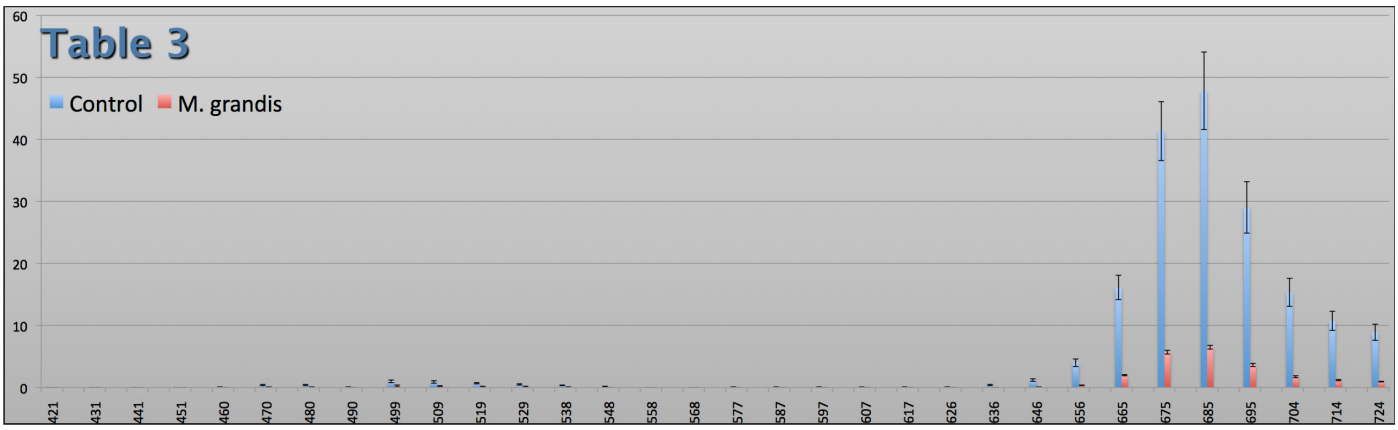
Table 3
Control
M. grandis
60
50
40
30
20
10
0
421
431
441
451
460
470
480
490
499
509
519
529
538
548
558
568
577
587
597
607
617
626
636
646
656
665
675
685
695
704
714
724

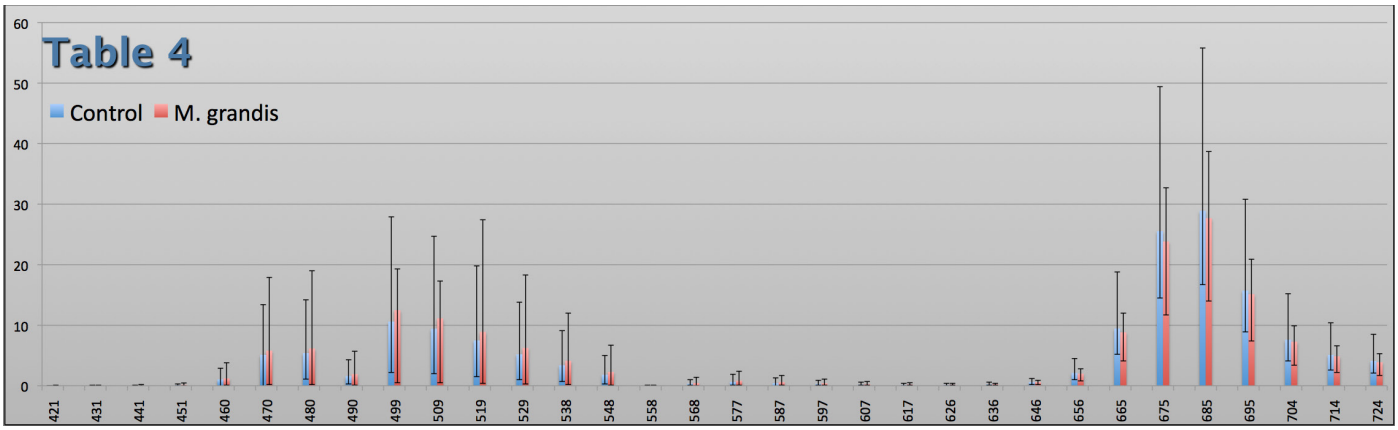
Table 4
Control
M. grandis
60
50
40
30
20
10
0
421
431
441
451
460
470
480
490
499
509
519
529
538
548
558
568
577
587
597
607
617
626
636
646
656
665
675
685
695
704
714
724

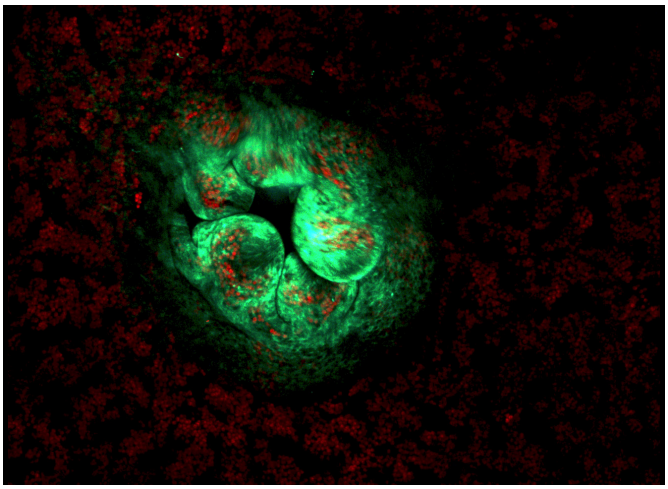

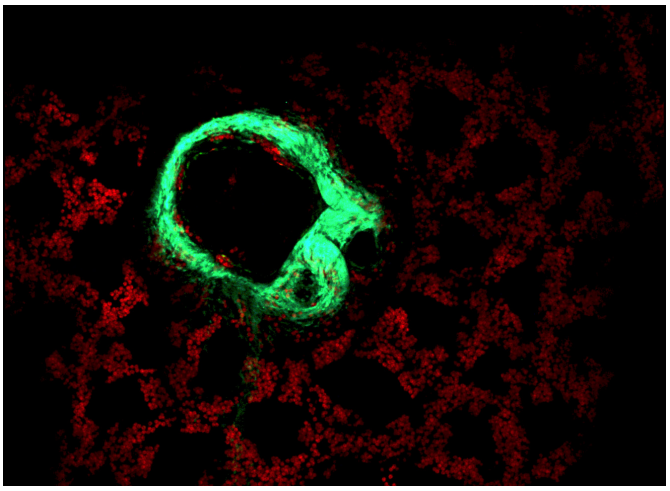

Images above are 3D Z stacks of *M. capitata* showing gross morphological and sybiont density differences.

Top: Control, 10x
Bottom: Interacting, 10x

FUTURE STUDIES

Large sample size allowing for strong statistical testing to determine if *M. grandis* really has an effect on coral potophores or not. Including other species of coral *M. grandis* is found would allow us to understand its effect on different coral species. Investigation into why *M. grandis* readily recruits to *P. compressa* but only rarely recruits to other species may offer insight into how to remove this invasive species.

ACKNOWLEDGEMENTS

Thank you to HIMB, Gates Lab for all its help; PIPES for getting me into HIMB; and KCC STEM for help with finding funding for time with the LSM.

A Novel Approach to Measure the Adherence and Invasion of *Campylobacter sp*. on HeLa Cells

By Codi Wong and Thomas Premeaux

ABSTRACT

Campylobacter sp. is a clinically significant food and water-borne bacterial pathogen, often causing gastroenteritis and paralysis in humans. The molecular basis of its pathogenicity and virulence remains elusive due in part to difficulties in culturing and measuring the organism's interaction with intestinal epithelial cells. To help overcome these limitations we developed a novel method to assess virulence in a high throughput based assay system using growth curve analysis. Strains of *Campylobacter* were grown under a variety of conditions, including the presence of human cervical cancer cells (HeLa cells). We could also correlate adherence/invasion with HeLa cell density, bacterial cell density, and measure differences between the bacterial strains in their ability to interact with the HeLa cells. By measuring and comparing the time intervals needed to reach log phase we can determine significant numbers of organisms either adhering to or invading the HeLa cells. After incubation and extensive washing, the adherence and/or invasion of the organism onto and/or into the HeLa cells was assessed by performing growth curves in an automated, incubating microtiter plate reader over a 48 hour period. Secondly, we determined the number of organisms invading HeLas through treatment with gentamicin. *C. coli* strain B692 was found to be both more adherent and more invasive than *C. jejuni* ATCC, corroborating data from traditional adherence/invasion assays. This high-throughput assay will allow us to investigate variables contributing to invasive pathogenicity of *Campylobacter* and improve the quantification of this process over previously used methods that were less sensitive and more time consuming.

HYPOTHESIS AND GOALS

Create an assay to better study *Campylobacter* invasion:

- That is more efficient, and requires less resources and time;
- and that provides improved, reproducible, consistent, and quantifiable results.

MATERIALS & METHODS (Flow Chart Below)

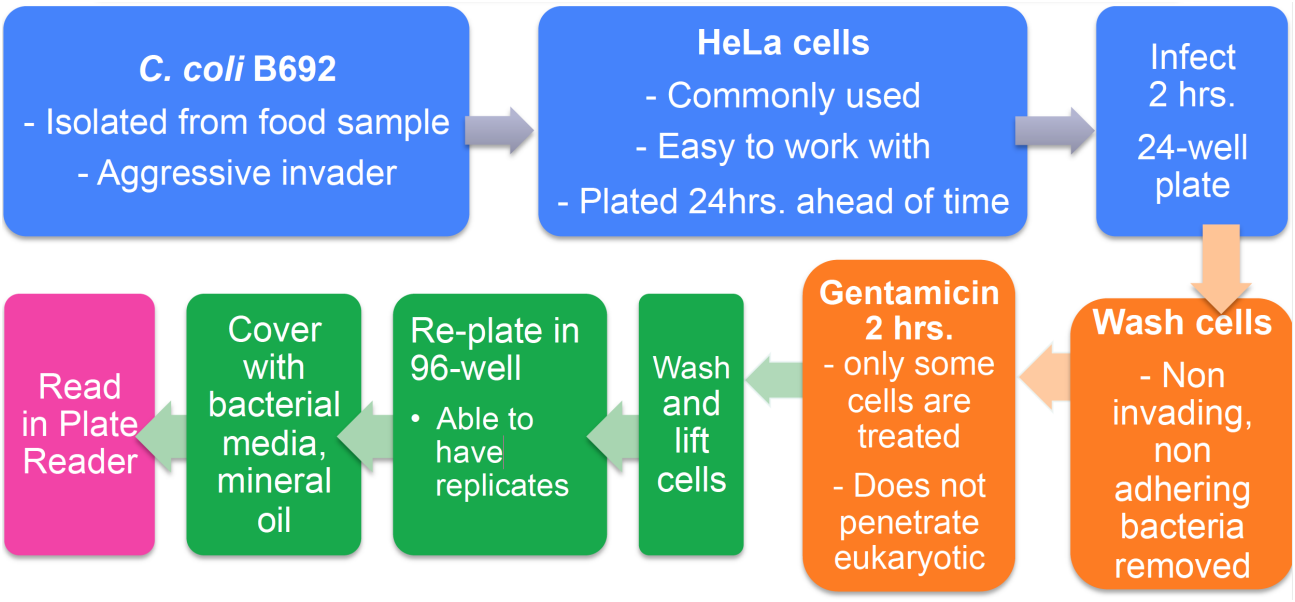

RESULTS

Plotting OD_{600} values over time for each bacterial dilution produces growth curves (***Figure A***). Wells containing invasion reactions are graphed separately (***Figure C*** and ***D***). Wells with no gentamicin treatment (***C***) contain bacteria that have invaded and/or adhered to HeLa cells, while wells with gentamicin treatment (***D***) contain only bacteria that have invaded HeLa cells.

Time is related to bacteria quantity; more initial bacteria results in rapid turbidity. Log phase estimates from these invasion graphs yielded an OD of approximately 1.5, which was then used in conjunction with the bacterial growth curve (***A***) to create a standard curve (***Figure B***). Thereby enabling us to quantify the amount of bacteria at a given time in our invasion assays.

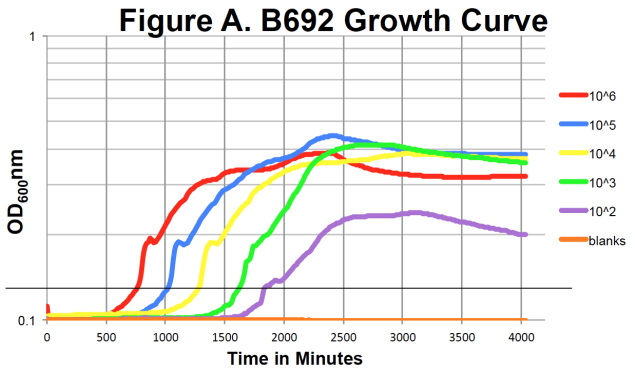

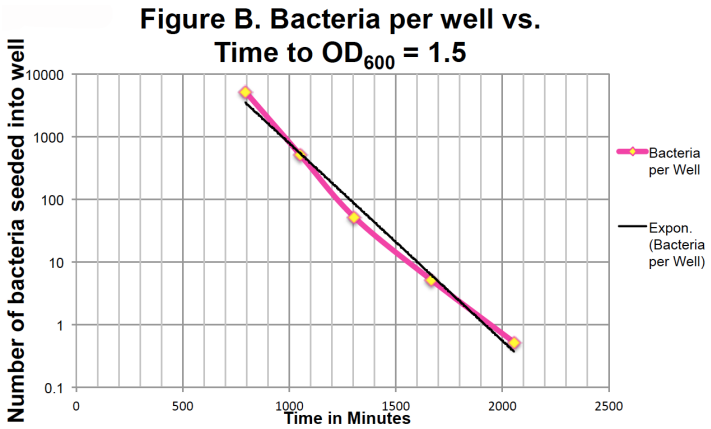

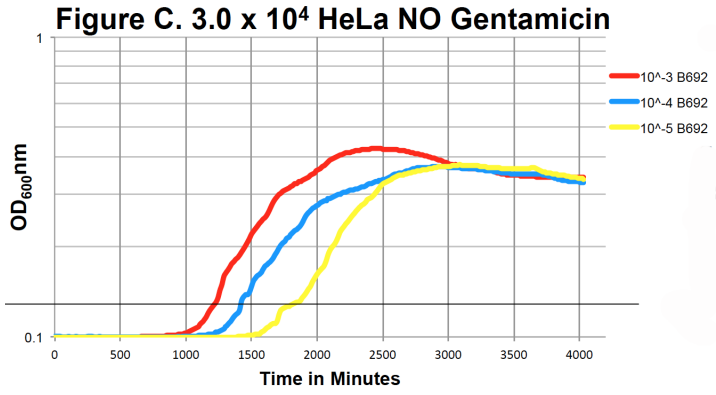

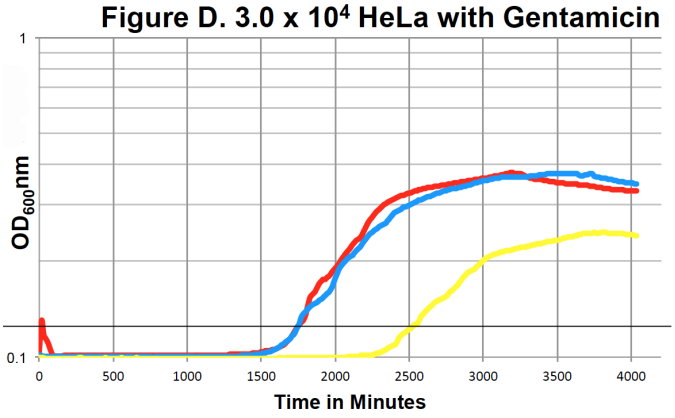

CONCLUSIONS & FUTURE DIRECTIONS

1. *Campylobacter* growth curve kinetics can be used to quantitate the number of organisms in a sample.
2. These assays save time and resources while also providing replicates.
3. These assays corroborate data from traditional assays. More *Campylobacter* is present when more HeLa cells are present.
4. These assays may be extensively modified:
   - Different bacterial strains or species (***Figure E***), genetically modified bacteria
   - Alternate cell lines
   - Additives or adjuvants.

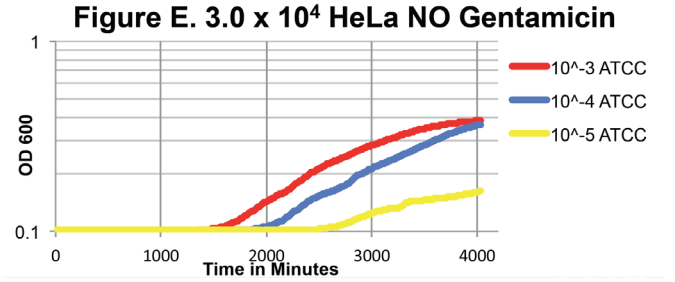

ACKNOWLEDGEMENTS

We thank C. Allen, S. Kawasaki, K. Noji and K. Noa for their ongoing laboratory and administrative support. Funding for this project was provided by the Kapi'olani Community College STEM Program, the Perkins Grant and the National Center for Research Resources (5P20RR016467-11) and the National Institute of General Medical Sciences (8 P20 GM 103466) from the National Institutes of Health. The University of Hawaii RMATRIX Program is supported by award number U545MD007584 from the National Institute on Minority Health and Health Disparities, National Institutes of Health. The content is solely the responsibility of the authors and does not represent the official views of the National Institutes of Health.

DIARRHEA! Studies On The Virulence Of Hawaiian *Campylobacter* Strains In Tissue Culture

By Jeff Griffith (*Faculty Mentors*: Dr. John M. Berestecky and Rebecca Kanenaka)

ABSTRACT

Campylobacter jejuni is the most common cause of bacterial gastroenteritis worldwide. Within the United States, Hawai'i has the highest rate of infection in the nation at 81 cases per 100,000. The exact mechanism of how *Campylobacter* causes diarrheal disease is unknown, although the prevailing hypothesis is that the organisms invade the intestinal epithelial cells as part of the disease process and that the intestinal environment somehow activates bacterial virulence.

We used HeLa cells in tissue culture as a model system to investigate the interaction between these bacteria and human cells. We studied the aVachment and invasion of a number of *Campylobacter* strains that were isolated from local disease cases in which disease severity was documented. We then compared these to 'wild' strains isolated from chicken carcasses, the most common source of *Campylobacter* infection.

The individual strains differed greatly in their ability to attach to and invade HeLa cells. The measured adherence and invasion efficiency was a reproducible strain characteristic that could not be altered by treatment of the bacteria with trypsin, a proteolytic enzyme found in the human gastrointestinal tract. Thus, there was no enhancement of virulence by this common intestinal environmental factor, nor did trypsin-sensitive bacterial surface proteins play a role in bacterial ability to adhere and invade. Surprisingly, the invasiveness of the strains did not correlate with the intensity of the disease in the patients from which the strains were isolated. In part, some of the strains isolated from cases of severe diarrhea were found to have low invasion efficiency while some of the wild chicken strains were highly invasive.

INTRODUCTION

With over 400 million infections worldwide, *Campylobacter jejuni* is one of the leading causes of bacterial diarrhea [1]. Though most cases are self-limiting, one out of 1000 cases may lead to Guillain-Barrè Syndrome (GBS), a neurological disorder in which the body's immune system reacts against the peripheral nervous system leading to paralysis [2]. Though there have been numerous studies in the past few decades, the exact mechanism of *C. jejuni*'s pathogenicity is unknown because there is no laboratory animal model. However, the generally accepted hypothesis is the following:

The bacteria must invade the intestinal epithelial cells. Cell invasion incites an intense inflammatory response via numerous chemical signaling pathways, presumably meant to contain and fight off the invasion within the intestinal environment. The inflammation that is meant to fight off the infection is what allows the bacteria to cause the diarrhea [3].

Experiments by other research groups have employed animal tissue culture techniques and adherence and invasion assays with *C. jejuni*. Such studies were conducted in artempts to find the bacterial virulence factors, as well as the host cellular factors involved in the pathogenesis of *Campylobacter* mediated disease. The results remain inconclusive though some notable conditions include the following:

C. jejuni may invade cells by first penetrating between cells and then moving into the subcellular space below the basal side of the epithelial cell to use some unknown mechanism to invade the epithelial cell from below [3]. A number of *Campylobacter* proteins have been shown to be somehow associated with the invasion process, including a secreted *Campylobacter* invasion antigen C (CiaC) [4] and Cad-F, an outer membrane protein [5]. Increased virulence has been attributed to sodium deoxycholate, a normal secretion in the intestinal tract [6]. The degree of virulence also appears to vary with the morphology of the organism, as rod forms have been shown to be more virulent than coccoid forms [7]. Other factors that may affect virulence include temperature, culture medium and the

degree of aeration [8].

Our experiments were designed to assess the following parameters: (1) which bacterial cell density gave the maximal adhesion and invasion, (2) which HeLa cell density gave the maximal adhesion and invasion, and (3) which *Campylobacter* growth phase gave the maximal adhesion and invasion. Aeer these parameters were determined for the reference strain B692, various other strains of *C. jejuni* and *C. coli* were assayed for comparison, including the GBS-associated Penner 41 strain and strains collected from Hawai'i clinical isolates and various poultry strains. Finally, trypsin was used to determine if a naturally occurring proteolytic enzyme in the human gut affected adhesion.

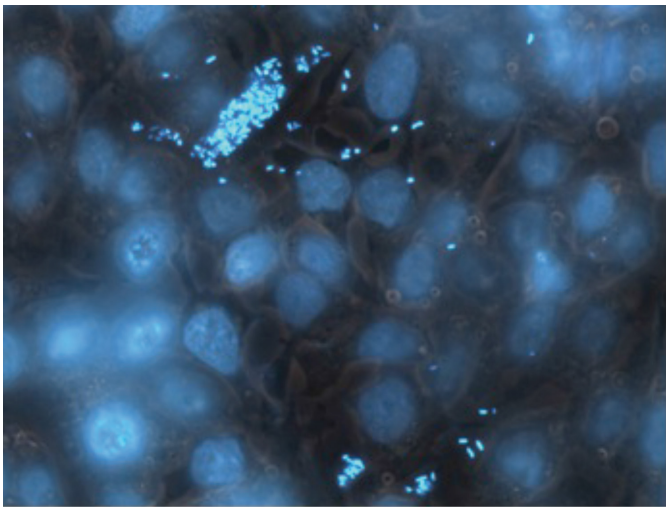

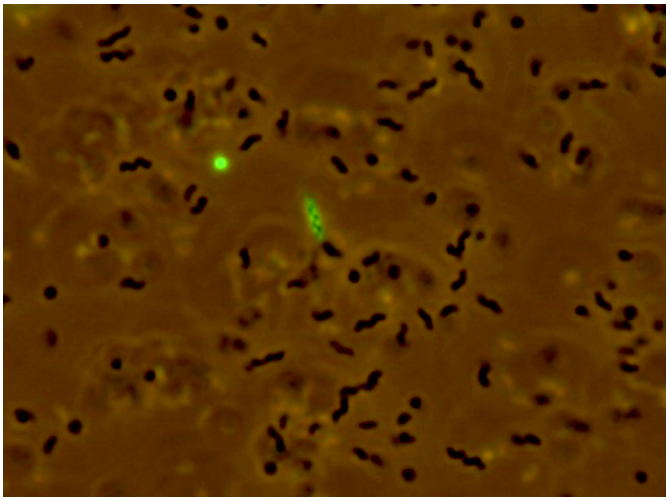

MATERIALS & METHODS

Bacterial cultures were grown for 24 hours, then subcultured for another 24 hours prior to assay. A BIO-RAD SmartSpecTM spectrophotometer was used to adjust the optical density (OD_{600}) of *Campylobacter* strains in tryptic soy broth (TSB) to 0.100 ± 0.01. The adjusted bacterial suspensions were then diluted 1:20 with antibiotic free DMEM with 1% fetal bovine serum (FBS) and inoculated onto HeLa cells seeded in 6-well plates at 1.4 x 10^6 cells/cm^2 (70% confluency). The multiplicity of infection (MOI) ranged from 0.26-36 bacterial cells per HeLa cell. The 6-well plates were incubated at 37˚ C in 5% CO_2.

Adherence was measured aeer 3-hours incubation: 3 wells of HeLa cells were washed with PBS and harvested with 0.1% Triton X-100 and the lysates were plated on Brucella agar aeer serial dilutions. To measure invasion, the remaining 3 wells were treated with a solution of gentamycin (500 µg/mL) in DMEM with 1% FBS and no other antibiotic and incubated for an additional 3 hours, then washed, lysed and cultured as above. Brucella plates were incubated at 37˚ C and colonies were enumerated aeer 72 hours. Controls for HeLa cell confluency, bacterial growth phase and bacterial concentration were also performed to ensure optimal assay conditions. Trypsin-treated bacteria suspensions were used to observe effect on adhesion.

RESULTS

$$Multiplicity\ of\ Adherence\ (MOA) = \frac{\left(\frac{Raw\ Data\ Adhered}{HeLa\ Cell\ Number}\right)}{(Supernatant + Raw\ Data\ Adhered)} \times 10^6$$

Strain	Species	MOA
Patient 12	*C. coli*	0.084009
Chicken Strep-R	*C. coli*	0.031665
Patient 3	*C. jejuni*	0.014858
Patient 11	*C. jejuni*	0.00488
Patient 5	*C. jejuni*	0.004314

Table 1. Five highest MOA values of the strains and species tested. MOA is a measure of the number of bacteria that adhere per host cell per each 10^6 bacteria in the well.

$$Multiplicity\ of\ Total\ Infection\ (MOIN\ Total) = \frac{\left(\frac{Number\ of\ Invading\ Bacteria}{HeLa\ Cell\ Number}\right)}{(Supernatant + Raw\ Data\ Adhered)} \times 10^6$$

Strain	Species	MOIN/Total
Patient 12	*C. coli*	0.002610
Chicken Strep-R	*C. coli*	0.000529
Patient 3	*C. jejuni*	0.000211
Patient 11	*C. jejuni*	0.000155
Patient 5	*C. jejuni*	0.000101

Table 2. Five highest MOIN Total values of the strain and species tested. MOIN Total is a measure of the number of bacteria that invade per host cell per each 10^6 bacteria in the well.

Strain at Specified Confluency	MOA	MOIN Total
Chicken Strain at 50% Confluency	0.024782	0.000239
Chicken Strain at 70% Confluency	0.021218	0.000185
Chicken Strain at 90% Confluency	0.021589	0.000049

Table 3. MOA and MOIN Total when varying the concentration of HeLa (host) cells per well. A 6-well plate is estimated to hold a maximum 2 x 10^6 HeLa cells per well.

Strain with Growth Time	MOA	MOIN Total
Chicken Strain at 16 hours	0.682177	0.001906
Chicken Strain at 24 hours	0.469567	0.004895
Chicken Strain at 48 hours	0.404995	0.002464

Table 4. MOA and MOIN Total when varying the bacterial growth phase prior to assay.

Treatment Well	Average MOA
Trypsin Treated Well	0.00163500
Non-Trypsin Treated Well	0.00159645

Table 5. The effect of trypsin treatment on MOA in HeLa cells. Average MOA of three replicas per treatment. *Campylobacter* were pretreated with trypsin for one hour before being added to the HeLa cell culture.

DISCUSSION

Aeer establishing optimal conditions for invasion (i.e. HeLa cell confluency, bacterial growth phase, and bacterial concentration), our results strongly suggest that the mechanisms for adhesion and invasion are independent events. Although a strain may have high MOA values, it does not necessarily correlate with high MOIN Total values.

Furthermore, *Campylobacter* treated with trypsin exhibited no change in its ability to attach to HeLa cells. This suggests that the adhering factor is not a protein that is susceptible to trypsin's proteolytic activity.

C. coli seems to possess strong adhesive and invasive ability. This suggests that *C. coli* may play a larger role in gastrointestinal infection than *C. jejuni*.

MOA and MOIN Total values generally did not correlate with the clinical intensity of gastroenteritis (i.e. bloody diarrhea).

REFERENCES

1. World Health Organization: *Campylobacter*. www.who.int/vaccine_research/diseases/diarrhoeal/en/index2.html. 12/10/09
2. Nachamkin, I, Allos, BM, and Ho T. (1998) *Campylobacter sp*ecies and Guillain- Barrè Syndrome. Clinical Microbiology Reviews 11: 555–567.
3. van Alphen, LB, Bleumink-Pluym, NMC, Rochat, KD, van Balkom BWM, Wöste, MMSM, and van Putten, JPM. (2008) Active migration into the subcellular space precedes *Campylobacter jejuni* invasion of epithelial cells. Cell Microbiology 10: 53-66.
4. Christensen, JE, Pacheco, SA, and Konkel, ME. (2009) Identification of a *Campylobacter jejuni*-secreted protein required for maximal invasion of host cells. MolecularMicrobiology 1-13.
5. Monteville, MR, Yoon, JE, and Konkel, ME. (2003) Maximal adherence and invasion of INT 407 cells by *Campylobacter jejuni* requires the CadF outer- membrane protein and microfilament reorganization. Microbiology 149: 153- 165.
6. Malik-Kale, P, Parker, CT, and Konkel, ME. (2008) Culture of *Campylobacter jejuni* with Sodium Deoxycholate Induces Virulence Gene Expression. Journal of Bacteriology 190: 2286–2297.
7. Moran, AP and Upton, M. (1986) A comparative study of the rod and coccoid forms of *Campylobacter jejuni* ATCC 29428. Journal of Applied Bacteriology 60: 1-10.

8. Verhoeff-Bakkenes, L, Hazeleger, WC, de Jonge, R, and Zwietering, MH. (2009) *Campylobacter jejuni*: a study on environmental conditions affecting culturability and in vitro adhesion invasion. Journal of Applied Microbiology 1-8.

ACKNOWLEDGEMENTS

In gratitude to John Berestecky, Ph.D., Rebecca Kanenaka, Matt Tuthill, Ph.D., Colleen Allen, Andrew Miyashiro, Codi-Lee Wong, Lucas Manica, Sherine Boomla, Sheryle Ishimoto, Vannarin Tan, Zach Darnell, Jill Fujiyama and Amy Jenkins. Funding provided by NSF and NIH-INBRE (Award Number P20RR016467). This material is based upon work supported by the Na6onal Science Founda6on. Any opinions, findings, and conclusions or recommenda6ons expressed in this material are those of the author(s) and do not necessarily reflect the views of the NSF.

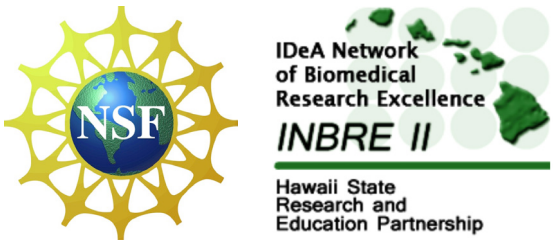

Use of growth curves to measure adherence of *Campylobacter sp*. on HeLa cells

By Codi Wong, Lucas Heldt, and Thomas Premeaux
(*Faculty Mentors*: Matthew Tuthill, Alan Garcia, and John Berestecky)

ABSTRACT

Campylobacter sp. is a clinically significant food and water-borne bacterial pathogen, often causing gastroenteritis and, in some cases, paralysis in humans. The molecular basis of its pathogenicity and virulence remains elusive due in part to difficulties in culturing and measuring the organism's interaction with intestinal epithelial cells. To overcome this limitation we developed a way to assess virulence in a novel microtiter plate based assay system using growth curve analysis. Strains of *Campylobacter* were grown under a variety of conditions, including the presence of human cervical cancer cells (HeLa cells).

After an initial incubation and extensive washing, the adherence and/or the invasion of the organism onto or into the HeLa cells was assessed by performing growth curves in an automated, incubating plate reader measuring optical density (OD) at multiple intervals over a 48 hour period. By measuring and comparing the time intervals needed to reach log phase we could determine whether or not significant numbers of bacteria were either adhering to or entering the cells they were grown with. We could also correlate adherence/invasion with HeLa cell density as well as bacterial cell density and we also could measure differences between the bacterial strains in their abiltiy to interact with the HeLa cells. This high-throughput protocol will allow us to investigate various questions posed by our initial experiments and challenge previous research done with less sensitive techniques.

MATERIALS & METHODS

Campylobacter strains were inoculated in to biphasic cultures and incubated in 10% CO_2 at 37˚ C before use in the adherence assays.

HeLa cells were plated in either 96- or 24- well plates at various cell densities in DMEM-10% FCS for 48 hours. Prior to co-cultivation with *Campylobacter* the plates were washed and dilutions of *Campylobacter* in DMEM-1% FCS with no antibiotic, were pipetted onto the HeLa cultures and incubated at 5% CO2 at 37˚ C for 2 hours.

The 96-well plates were then washed 3 times with DMEM to remove non-adherent *Campylobacter*, whereupon 100 µl of Bolton broth was added, overlaid with two drops of sterile mineral oil, and incubated in a BioTek Synergy plate reader at 37˚ C. Absorbance readings at 600 nm were performed at 15 minute intervals over a 48 hour period.

Alternatively for assays performed in 24-well plates, wells were washed with DMEM to remove non-adherent *Campylobacter*, cells were lifted with trypsin/EDTA and neutralized with an equal volume of DMEM-1% FCS. Replica 10 uL samples from each well were transferred to wells on a 96-well plate containing 100 µl of bolton broth and overlaid with 2 drops of sterile mineral oil and incubated in the BioTek Synergy plate reader as described above.

HYPOTHESIS

a.) Bacterial growth curve analysis can be used to enumerate the number of bacteria in the well of a 96-well plate.

b.) If true, then such growth curve analysis can be used to measure bacterial adherence to and invasion into host cells.

DATA & RESULTS

Our initbactial adhesion assay experiments presented two problems: (1) Campyloer adheres to no HeLa (control) wells, and (2) washing in 96-well plates causes a large and unpredictable loss of HeLa cells.

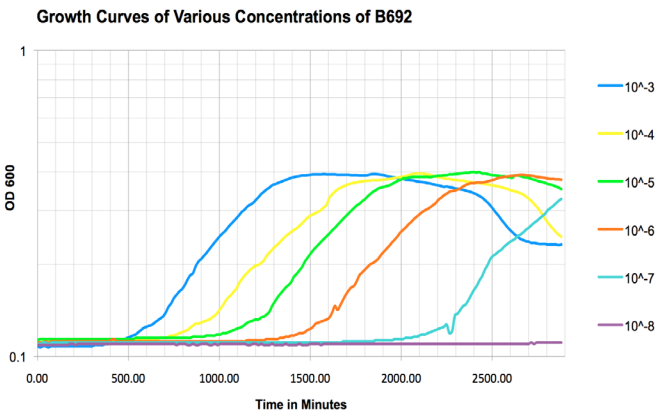

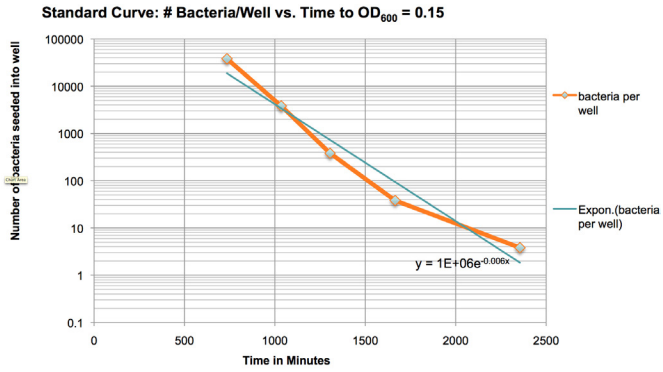

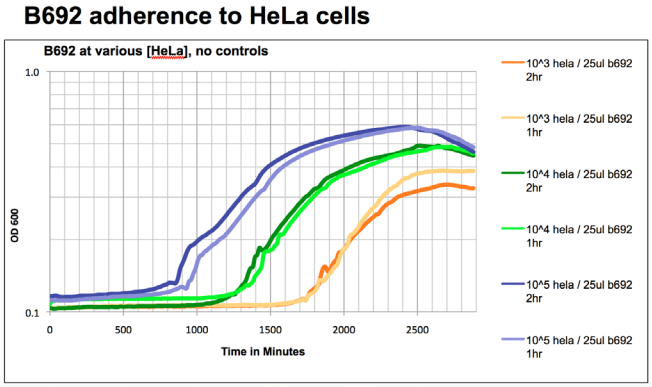

Washing Experiment with Staining

Plates seeded with diminishing HeLa cell concentrations and incubated overnight at 37˚ C. Columns were washed multiple times with various buffers and the buffers were suctioned off with a multipipettor. Plate fixed with 10% formalin in PBS and stained with crystal violet.

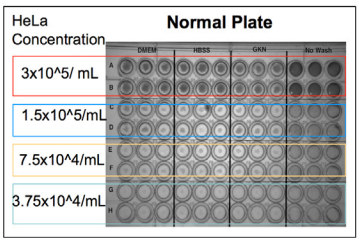

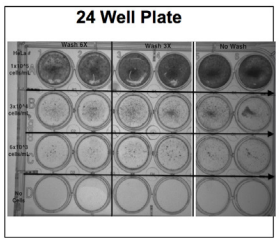

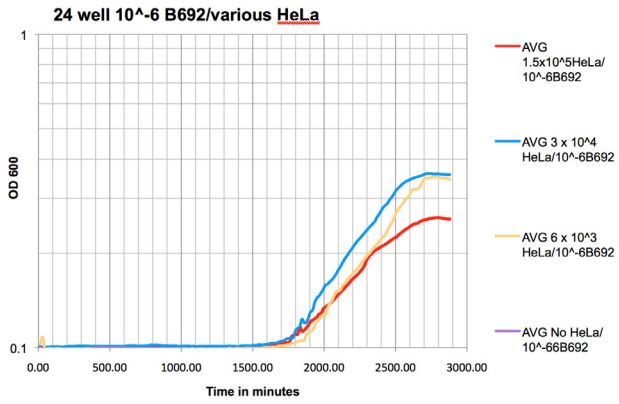

CONCLUSIONS

- *Campylobacter* growth curve kinetics can be used to quantitate the number of organisms in a sample.
- This assay can be adapted to measure bacterial adherence in a 96-well plate format, but the washing steps introduce technical artifacts.
- This limitation appears to be solved by moving to a 24-well plate format.
- This is a work in progress. The initial results showing a strong correlation between HeLa cell number and bacterial adherence needs to be confirmed in the 24-well format.

ACKNOWLEDGEMENTS

We thank R. Kanenaka, C. Allen, S. Kawasaki, K. Noji and K. Noa for their ongoing laboratory and administrative support. Funding for this project was provided by the Kapiolani Community College STEM Program, the Perkins Grant and the National Center for Research Resources (5P20RR016467-11) and the National Institute of General Medical Sciences (8 P20 GM 103466) from the National Institutes of Health. The University of Hawaii RMATRIX Program is supported by award number U545MD007584 from the National Institute on Minority Health and Health Disparities, National Institutes of Health. The content is solely the responsibility of the authors and does not represent the official views of the National Institutes of Health.

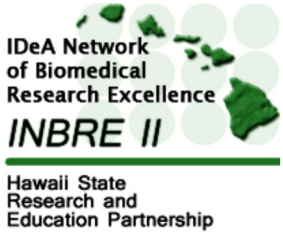

Use of Phage Display to Produce Antibodies against *Campylobacter jejuni*

By Robin Kaai and Thomas Premeaux
(*Faculty Mentors*: Matthew Tuthill, Alan Garcia, and John Berestecky)

INTRODUCTION

Current methods for monoclonal antibody production utilize hybridoma technology. This requires repeated immunization of a mouse followed by the harvest and fusion of spleen cells with an immortalized cell line in order to produce and select for antigen-specific antibody-producing clones. Because of the cost, time, and expertise required for traditional monoclonal production, we are investigating the efficacy of using phage display to generate novel antibodies. The aim of this study is to develop proficiency in phage display, and allow for a supplemental approach to produce monoclonal antibodies at our facilities. Initial studies will target *Campylobacter jejuni*, a gram-negative, epsilonproteobacteria that is the most common cause of bacterial gastroenteritis.

METHODOLOGY

Phage display utilizes a library of modified M13 bacteriophages that display single-chain variable fragments of diverse specificities. Through repeated antigen-targeted biopanning, phage elution, and coinfection of host bacteria with helper phage, target phages with the desired specificity can then be amplified, isolated, and utilized in biomedical research settings.

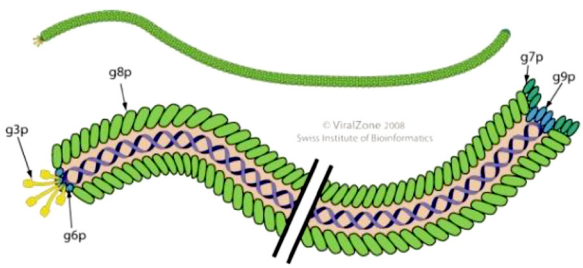

Figure 1. M13 bacteriophage

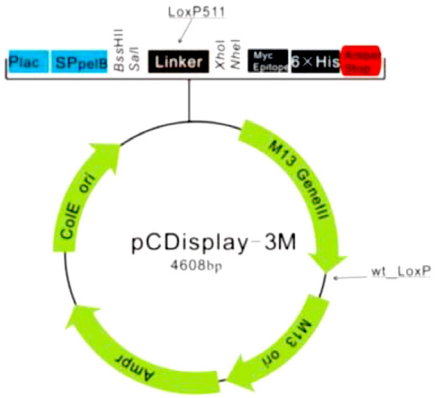

Figure 2. Phagemid containing scFv

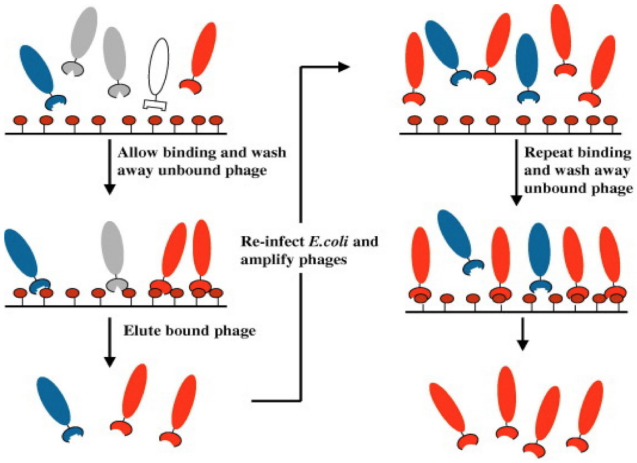

Figure 3. Biopanning

The biopanning process involves the introduction of the phage library into antigen-coated microtiter wells, stringent washes and elution. Host re-infection and repeated biopanning then allows for the amplification of target-specific phages.

RESULTS

Thus far, we have been successful in amplifying the phagemid library, as well as helper phage stocks for

back up stocks and future work. In addition, we have performed various infection assays to validate the phage library, and confirm the background genotypes of the host cells involved. Primers were also designed to track the plasmids through the infection and biopanning process.

Figure 4 **(left image below) Maxiprep results.** pCDisplay-3M phagemid linearized using SalI and XhoI restriction digestion (**B**) was electrophoresed in conjunction with the uncut control phagemid (**A**).

Figure 5 **(right image below) Maxiprep validation.** The presence of a 0.4 kilobase band resulting from the SalI and NheI restriction digestion confirms that the VH region is present in the phagemid maxiprep (**C**).

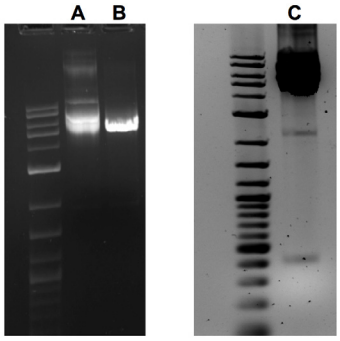

Figure 6 **(left image below) Phagemid primer validation.** Phagemid-specific primers were used to amplify a 1 kilobase region of the pCDisplay-3M. P.C.R. reactions were perform using annealing temperatures of 60C (A) and 55C (B).

Figure 7 **(right image below) Helper phagemid primer validation**. Primers were designed and used in P.C.R. to confirm the specificity to the helper phagemid, as shown by the production of a 0.3 kilobase amplicon (C).

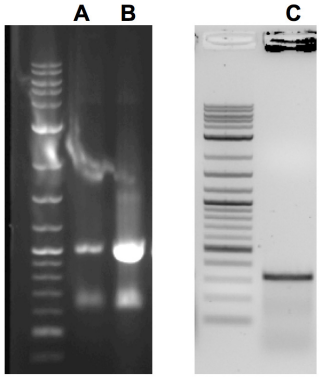

Figure 8 **(page 51).** Phage viability validation *E. coli* TG1 host cells were uninfected, infected with the phagemid display library, the helper phage stock, or both. Uninfected, infected, or coinfected host cells were then plated as on standard media with the absence or presence of antibiotics kanamycin and/or ampicillin. The control set of plates was then scored in order to determine viability of the phages and the efficiency of cell infection. Display phages contain an ampicillin resistance cassette while helper phages contain a kanamycin resistance cassette in order to select for co-infected host cells during target phage amplification.

CONCLUSIONS

Transformation, amplification and maxiprep harvest and subsequent restriction digestion and DNA agarose gel electrophoresis confirms that the

- M13 phagemid library was amplified;
- M13 phagemid is the appropriate size;
- upon restriction digestion, the M13 phagemid matches the published restriction map.

Polymerase chain reactions performed on the phagemid or helper phage stock confirm that

- the phagemid primers are specific and amplified stock is correct;
- designing helper phage specific primers were successful;
- both primer sets may be used to detect the presence of helper phages in various steps of library production.

Plating assays of *E. coli* TG1 host cells with or without infection on media containing various antibiotics indicate that

- uninfected TG1 host cells will not grow in the presence of ampicillin or kanamycin;
- phagemid stocks are intact and contain cassettes allowing infected TG1 cells to grow in the presence of ampicillin;
- helper phages are intact and contain cassettes allowing infected TG1 to grow in the presence of kanamycin;
- dual infection with phagemid and helper phage is possible; AMP/KAN may be used to select for coinfected TG1.

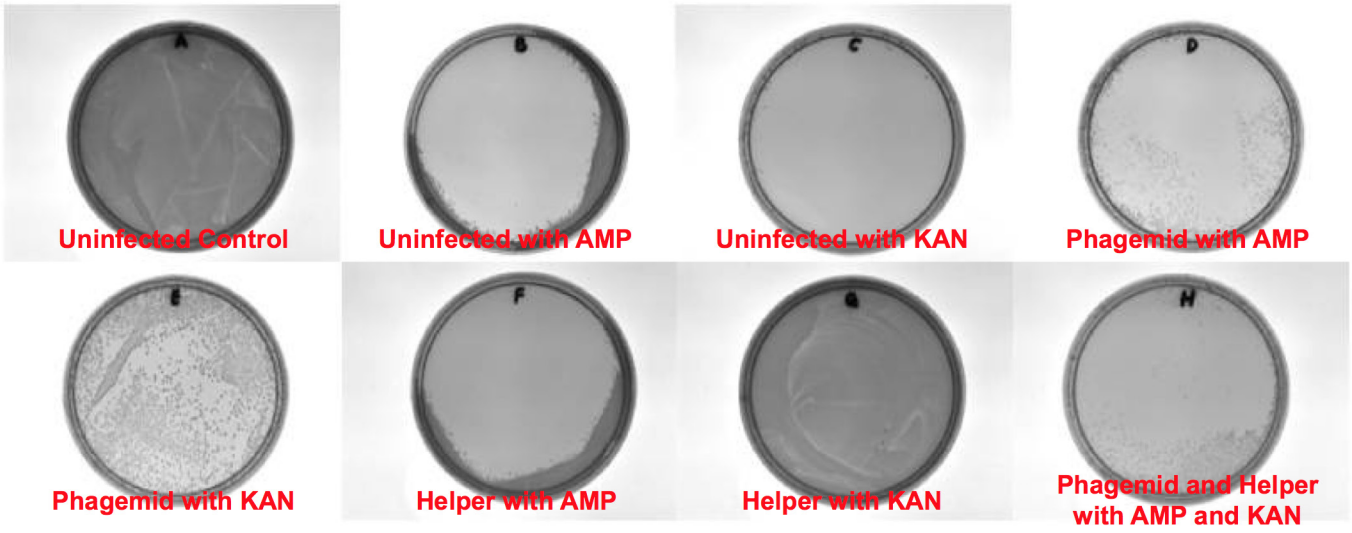

FUTURE PLANS

With stocks established and validated, we are in the process of applying the phage display methodology to *Campylobacter jejuni*. Once successful phages have been isolated, amplified and banked, this technology will allow for: epitopic tagging of antigens, immunoprecipitation, antigen isolation and characterization, and recombinant modifications of antibody variable regions. Moreover, it will allow us to increase our monoclonal output, involve more students in phage antibody production and incorporate components of the process into select campus lab courses.

LITERATURE CITED

C. F. Barbas III, D. R. Burton, J. K. Scott, and G. J. Silverman, (2001) *Phage Display: A Laboratory Manual*. Cold Spring Harbor Laboratory Press, Cold Spring Harbor, NY.

ACKNOWLEDGEMENTS

We thank C. Allen, S. Kawasaki, K. Noji and K. Noa for their ongoing laboratory and administrative support. Funding for this project was provided by the Kapiolani Community College STEM Program, the Perkins Grant and the National Center for Research Resources (5P20RR016467-11) and the National Institute of General Medical Sciences (8 P20 GM 103466) from the National Institutes of Health. The University of Hawaii RMATRIX Program is supported by award number U545MD007584 from the National Institute on Minority Health and Health Disparities, National Institutes of Health. The content is solely the responsibility of the authors and does not represent the official views of the National Institutes of Health.

Effects of Retinoic Acid on Proto-Oncogene and Tumor Suppressor Gene Expression in Neuroblastoma

By Aaron Halemano, Melanie Nakatani, and Micon Garvilles
(*Faculty Mentors*: Matthew Tuthill, Randal Wada, and John Berestecky)

INTRODUCTION

Neuroblastoma is the most common extracranial solid tumor found in children, resulting in approximately six hundred and fifty new cases in the U.S. annually. This peripheral nervous system cancer is derived from pluripotent stem cells that arise out of the neural crest during development. N-myc oncogene overexpression and/or amplification is often predictive of poor prognosis, and correlates with advanced and aggressive disease, as well as resistance to chemotherapy.

More recent clinical trials involving retinoic acid adjuvant therapy have shown efficacy in the setting of minimal residual disease. Numerous laboratory studies have also shown that retinoic acid induces the downregulation of N-myc proto-oncogene expression in select neuroblastoma cell lines. While the effects of retinoic acid appear to be mediated through promoter regulation of the N-myc gene, the exact mechanism of N-myc downregulation has not been clearly established. The specific aim of this study is to determine if possibly the expression of other gene targets are also modulated by retinoic acid.

METHODOLOGY

The LA-N-5 human neuroblastoma cell line was treated for four days with retinoic acid or dimethyl sulfoxide (control medium) before total RNA extraction. Quantitative real-time polymerase chain reaction analyses were then performed against four gene targets: RB1, TP53, AUTS2 and ROR1. N-myc downregulation via retinoic acid served as the positive control, while the HPRT1 (hypoxanthine-guanine phosphoribosyltransferase) gene target served as the reference gene and allowed for the determination of relative levels of gene expression across different sample sets.

Figure 1 (below). Workflow methodology. LA-N-5 neuroblastoma cells were treated with retinoic acid, total RNA was then extracted and served as template for RT-PCR analyses.

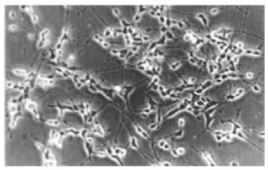

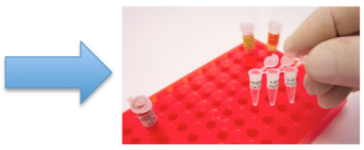

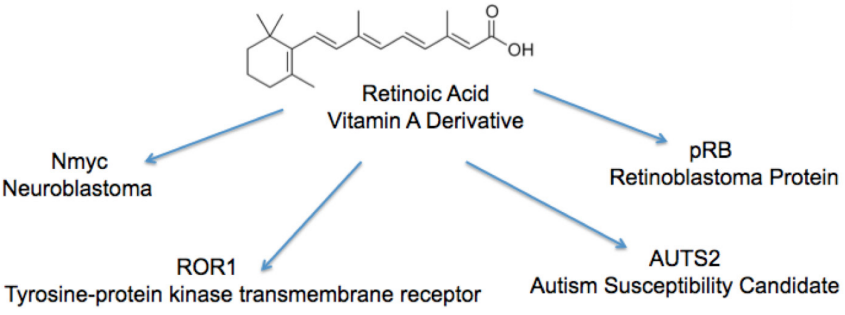

RESULTS

As expected, retinoic acid treatment of the LA-N-5 neuroblastoma cell line resulted in little change in HPRT1 reference gene expression. Moreover, transcriptional activity of the positive control N-myc gene was downregulated. However, retinoic acid treatment of LA-N-5 cells resulted in either modest, or significant upregulation of the target genes RB1, AUTS2 and ROR1.

Figure 2. Real- time polymerase chain reaction for HPRT1, N-myc and RB1. Amplification plot (a). ddCt normalized fold expression (b). Melt peak chart of HPRT1 (c), N-myc (d), and RB1 (e).

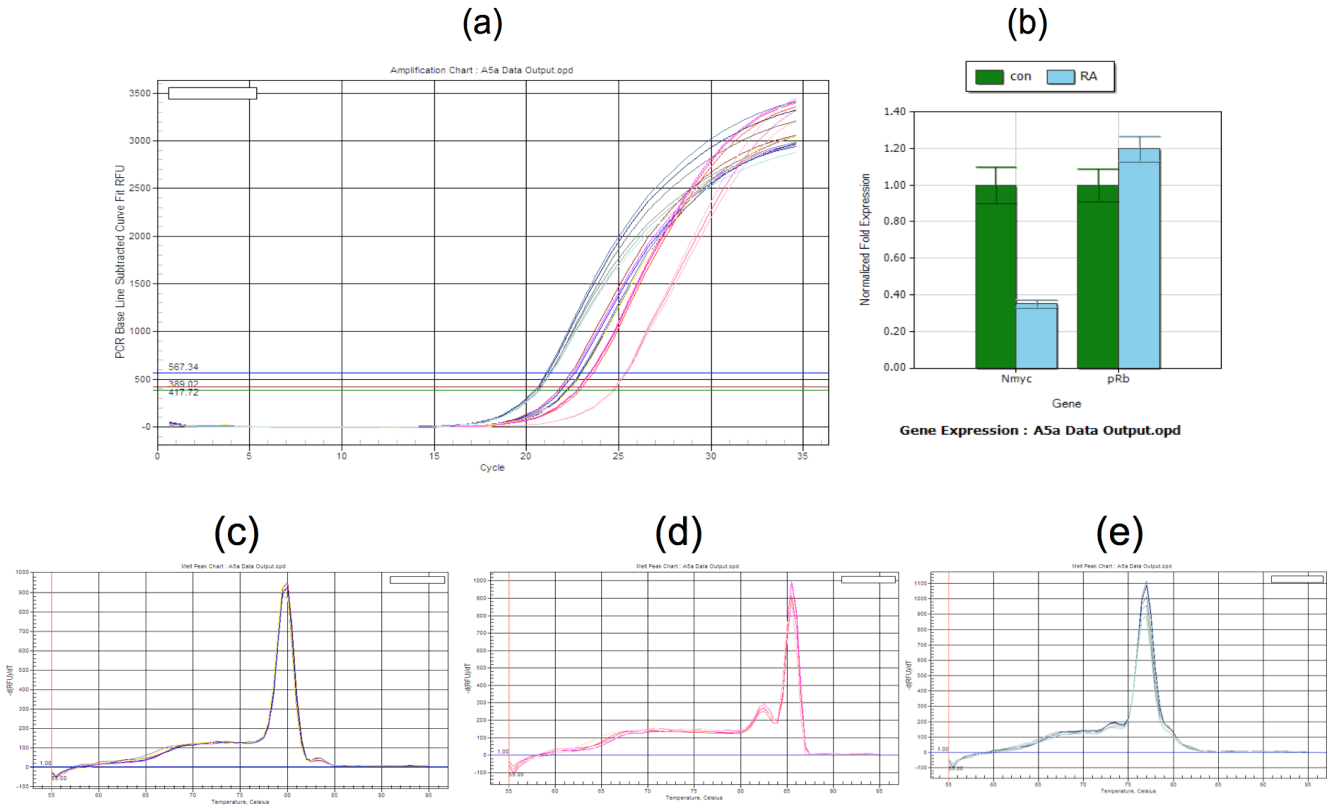

Figure 3. Real-time polymerase chain reaction for HPRT1, AUTS2 and ROR1. Amplification plot (a). ddCt normalized fold expression (b). Melt peak chart of HPRT1 (c), AUTS2 (d), and ROR1 (e).

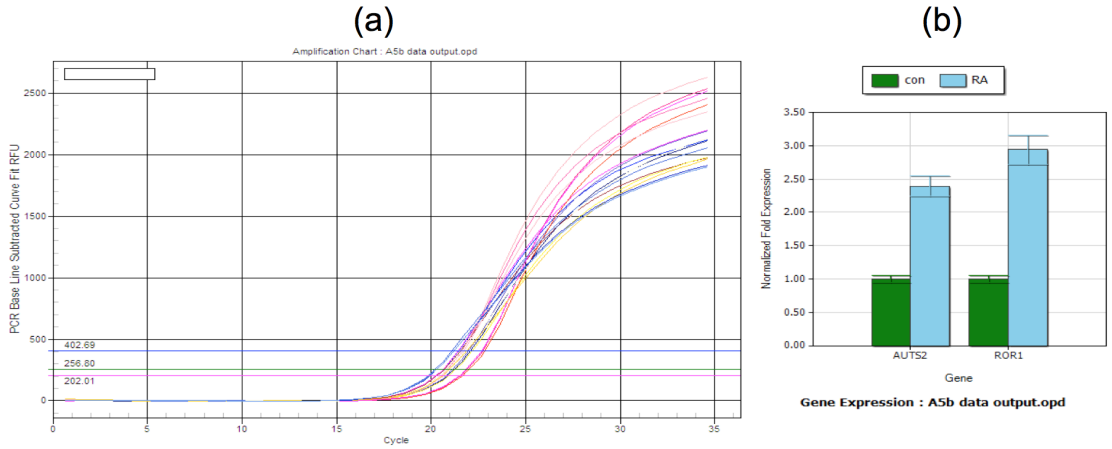

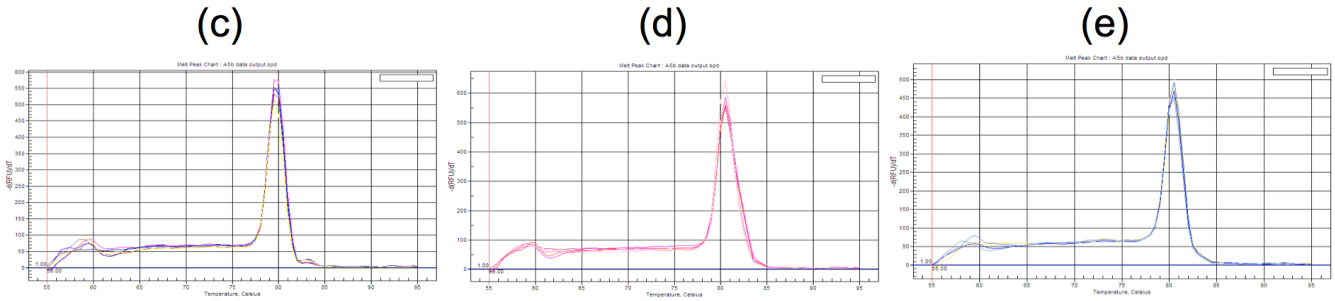

CONCLUSIONS

Our studies continue in order to determine if the observed changes are both reproducible in other neuroblastoma cell lines and significant enough to potentially have a physiological effect. Moreover, we are investigating if the effects of retinoic acid are enhanced with concurrent treatment of a cyclin-dependent kinase 4/6 inhibitor. The culmination of which may allow for a more an alternate treatment regimen at lower individual concentrations of each drug, as well as more conclusively determine if these genes are modulated by retinoic acid.

FUTURE PLANS

Polymerase chain reaction will be used to amplify target gene fragments from LA-N-5 (a). (See flow chart at the bottom of the page.) These amplicons will then be TA-cloned into the pDrive vector (b), transformed into *E. coli* (c) and screened for ampicillin resistant white colonies (d). The positive clones will then be confirmed via polymerase chain reaction and validated via DNA sequencing. Successful clones will be used to generate standard curves for subsequent absolute quantification real-time polymerase chain reactions.

LITERATURE CITED

1. S. Toegel, W. Huang, C. Piana, F. M. Unger, M. Wirth, M. B. Goldring, F. Gabor and H. Viernstein. 2007. Selection of reliable reference genes for qPCR studies on chondroprotective action. BMC Molecular Biology, 8:13.
2. Y. Liu and W.F. Bodmer.2005. Analysis of P53 mutations and their expression in 56 colorectal cancer cell lines. PNAS. 103:4, 976-981.
3. M. Hudecek, T. M. Schmitt, S. Baskar, M.T. Lupo-Stanghellini, T. Nishida, T. N. Yamamoto, M. Bleakley, C. J. Turtle, W. C. Chang, H. A. Greisman, B. Wood, D. G. Maloney, M. C. Jensen, C. Rader and S. R. Riddell. 2010. The B-cell tumor-associated antigen ROR1 can be targeted with T cells modified to express a ROR1-sepcific chimeric antigen receptor. Blood, 116:22, 4532-4541.
4. RTPrimerDB ID:1194 = Nmyc.
5. RTPrimerDB ID:8038 = RB1.

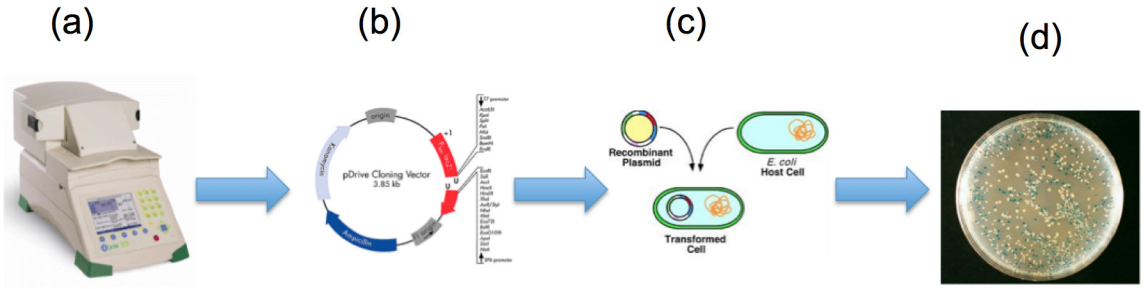

ACKNOWLEDGEMENTS

We thank A. Garcia, C. Allen, S. Kawasaki, K. Noji and K. Noa for their ongoing laboratory and administrative support. Funding for this project was provided by the Kapiolani Community College STEM Program, the Perkins Grant and the National Center for Research Resources (5P20RR016467-11) and the National Institute of General Medical Sciences (8 P20 GM 103466) from the National Institutes of Health. The University of Hawaii RMATRIX Program is supported by award number U545MD007584 from the National Institute on Minority Health and Health Disparities, National Institutes of Health. The content is solely the responsibility of the authors and does not represent the official views of the National Institutes of Health.

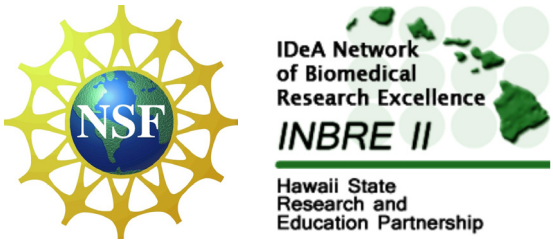

Measuring Wind on KCC Campus

By Tatiana Oje (*Faculty Mentor*: Aaron Hanai; *Peer Mentor*: Bradley Hughes)

INTRODUCTION

This is an analysis of surface winds on the Kapi'olani Community College (KCC) campus by Māunuunu Weather Station (MWS). Meteorologist use anemometers (***Fig. 1.a***) to measure wind speed. The siting of an anemometer is very important. NOAA recommends an anemometer be installed 32 feet above ground or 10 times the height of the nearest obstruction. MWS's is 9 feet above the ground. This experiment will focus on the value of MWS's wind data by comparing it to two other wind stations nearby.

Figure 1.a. Anemometer used by MWS. There are two parts, a wind vane that measure direction and wind cups that measure velocity

Māunuunu Weather Station (MWS) Design

Location: Honolulu, HI (21.3ºN, 157ºW)
Elevation: 215 ft
Anemometer Height: 9ft
Sensor Manufacturer: Davis Instruments

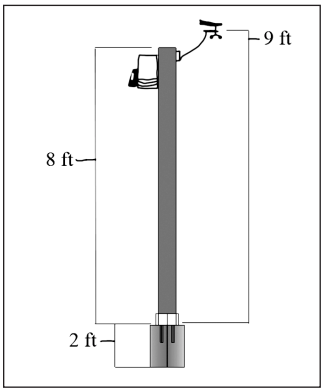

Figure 1.b. Sketch of MWS's dimensions (left) and photograph of MWS after installation (right).

Local Winds: Local wind patterns are global winds interacting with local topography and surface structures, the ocean, and vegetation. Local winds can tell a knowledgable observer many things about Hawaiian weather, such as if rain is coming or if the air will be voggy (filled with volcanic ash). It also reflects the behavior of the weather over the North East Pacific Ocean.

Timeline: Data was recorded in 30 minute intervals from May 13 to January 31, 2014. A day was chosen from this period to compare wind data to other near by sites.

Purpose/Objective: Test the accuracy of Māunuunu Weather Station's anemometer. Analyze the weather's influence on wind patterns.

METHOD

- Measured wind direction and speed (mph) with an MWS's anemometer.
- Compare time logged data to Weather Stations in proximity to MWS.
- Review of contemporary and historic Hawaiian meteorological literature.

Consulting Hawaiian Science: In T*he Wind Gourd of La'amaomao*, Moses Nakuina transcribes a complete kāhea ka makani (calling of the winds). In this Hawaiian legend, Kuapaka'a calls all the winds of the Hawaiian Islands to do his bidding. First published in old Hawaiian newspapers, this chant has allowed historians to create wind maps of the islands. The wind chant for the Kona district of O'ahu, where KCC is located, identifies the following winds and places where they blow.

Pu'uokona is of Kuli'ou'ou,
Ma-ua is the wind of Niu,
Holouhā is of Kekaha,
Māunuunu is of Wai'alae,
The wind of Lē'ahi turns here and there,
'Ōlauniu is of Kahaloa,

Wai‘ōma‘o is of Pālolo,
Kuehu-lepo is of Kahua,
Kukalahale is of Honolulu,
‘Ao‘aoa is of Māmala,
‘Ōlauniu is of Kapālama,
Haupe‘epe‘e is of Kalihi,
Ko-momona is of Kahauiki,
Ho‘e‘o is of Moanalua ...

There are two winds that travel over KCC, Lē‘ahi’s wind and Māunuunu of Wai’alae. (See the map to the right for the location of the place names in the wind chant. KCC is located on the Pālolo side of Lē‘ahi. See also ***figure 3*** below.)

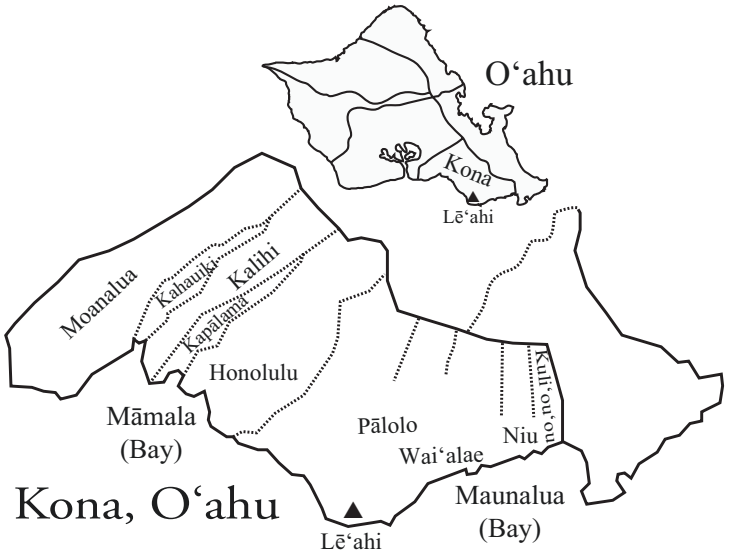

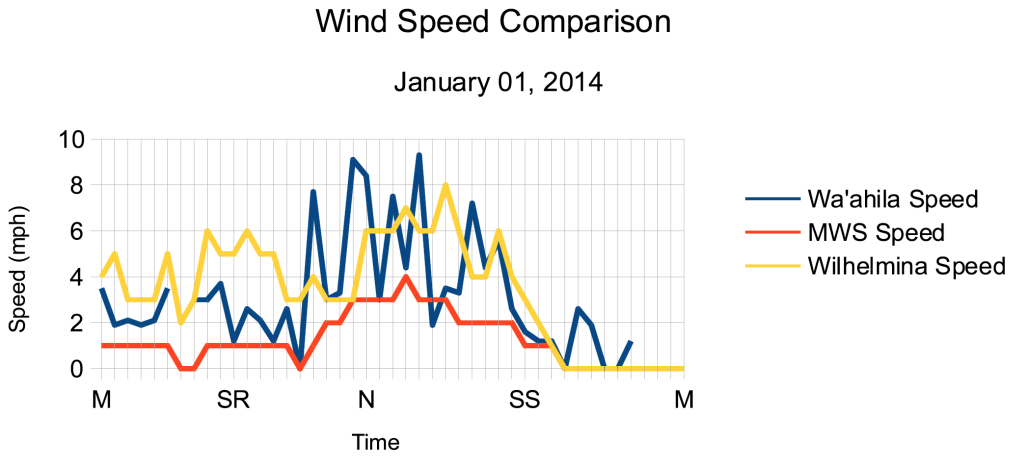

Figure 2. A chart of the distribution of wind speeds measured from MWS, the Wa’ahila Ridge, and the Wilhelmina Rise stations.

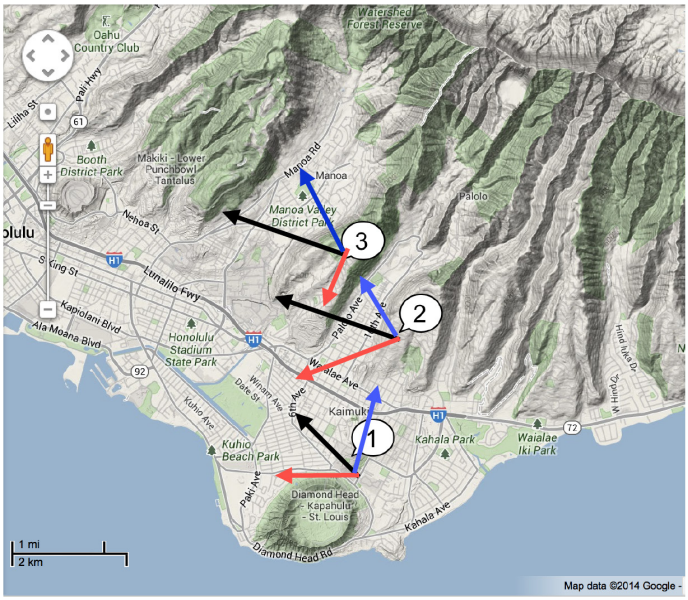

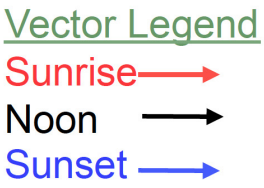

Figure 3. A map of MWS (1) in relation to Wilhelmina Rise station (2) and Wa’ahila Ridge station (3). Includes wind vectors for each station at different times in the day.

RESULTS

Diurnal wind patterns are variations in wind characteristics dependent on time of day due to solar heating. Figure 2 and Figure 3 charts wind speeds and direction, respectively, for MWS and two other wind stations in its area. In both figures the x-axis labels Midnight (M), Sunrise at 7:10am (SR), Noon (N), and Sunset at 6:00am (SS). Figure 3 shows the location of these station in relation to MWS.

ANALYSIS

From the data charted in Figures 2 and 4, a general trend can be seen. From sunrise to noon wind speeds are variable, but increase in magnitude. The direction of the wind vectors are not the same, and reflects the affect of local surface features. The Wilhelmina and Wa'ahila stations are located on mountain ridges, experience greater temperature differenced and downslope wind flow. While MWS is near a tall crater and coast line. Considering location, the wind vectors in Figure 3 were expected. Based on the data, any errors are most likely due to systematic errors because of the terrain differences and height of MWS's anemometer.

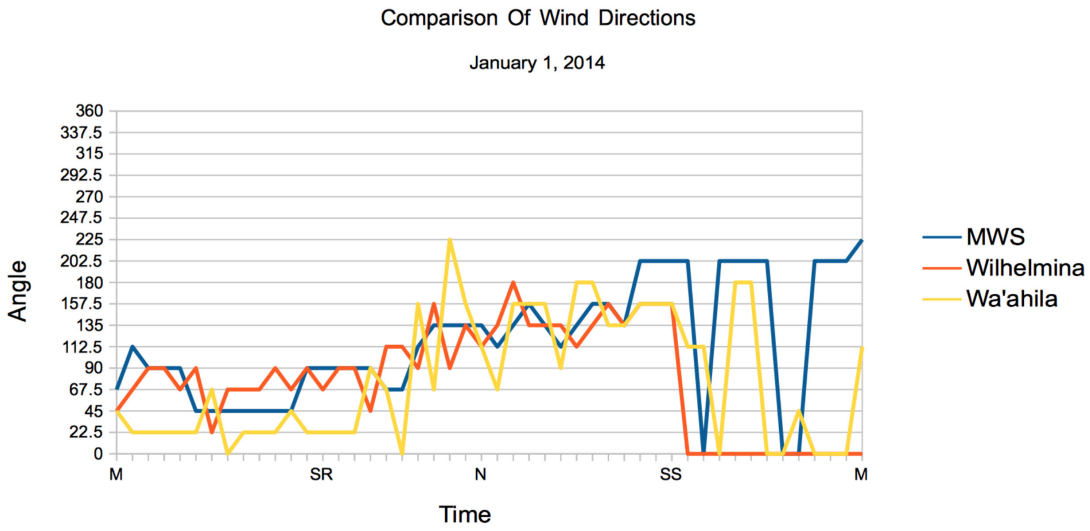

Figure 4. A chart of wind directions by time of day recorded by MWS, the Wa'ahila Ridge and the Wilhelmina Rise stations. See ***Figure 5*** for the corresponding directions of the angles from the y-axis.

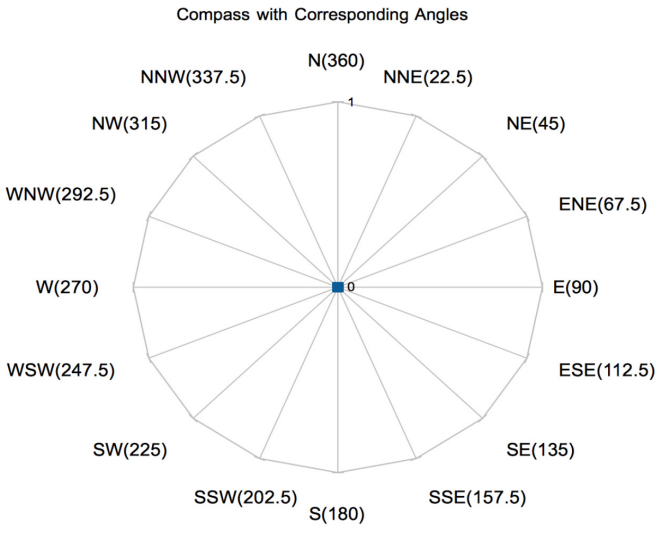

Figure 5 (left). Legend for angles and directions in Figure 4. Directions at 0 indicate times when there was no movement.

CONCLUSION

While MWS's wind data should not be used in applications such as aeronautics, marine navigation or meso-scale modeling, the data can still be useful for meteorological analysis. When combined with temperature, rain and solar radiation, MWS's wind data can show researchers valuable place-based trends and patterns.

FUTURE WORK

The next step is to build a taller structure for the anemometer or to mount it on top of a building.

REFERENCES

Leopold, Luna. Diurnal Weather Patterns on Oahu and Lania, PACIFIC SCIENCE, Vol. 11, April, 1948. PDF: 81-94.

Nakuina, M. K. (2005). The wind gourd of La'amaomao Translated by E. T. Mookini and S. Näkoa, Honolulu: Kalamakü Press. Original work published 1902.

Pukui, M. K., & Elbert, S. H. (1986.) Hawaiian dictionary. Honolulu: University of Hawai'i Press.

ACKNOWLEDGEMENTS

Mrs. Keolani Noa, Naomi Nihipali, KCC-STEM and KCC-Malama Hawaii, C-MORE Scholars Program.

Using Pupillometry To Evaluate Daytime Sleepiness

By Alexander Williams (*Faculty Mentors*: Hervé Collin, M.S., and John Rand, Ph.D.)

INTRODUCTION

Many college students endure high levels of sleep debt resulting in daytime sleepiness. Excessive daytime sleepiness (EDS) has been linked to memory impairment, mood instability, and a decrease of the immune system response, and can reduce driving performance [1]. Current quantitative methods for evaluating EDS are costly and time-intensive or are qualitative, self-reporting surveys. Therefore a simple, low-time intensive, cost effective and accurate method for evaluating EDS would be very useful for estimating sleep debt. In this pilot study, both pupil size and pupil stability are evaluated as potential quantitative markers for EDS.

HYPOTHESIS

Video pupillometry can be used to evaluate both short-term and long-term changes in pupil diameter [2], and thus may be used as a quantitative marker for EDS.

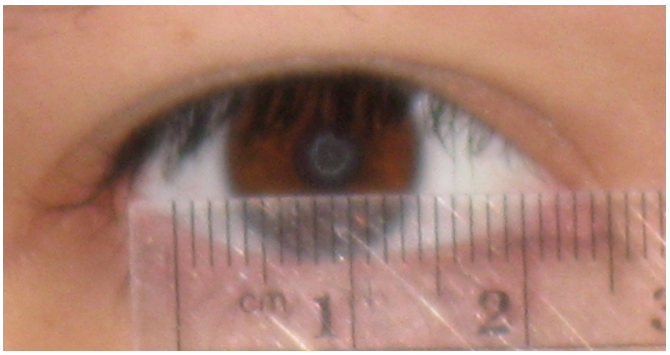

BACKGROUND

The pupil diameter is controlled by our autonomic nervous system (ANS). The ANS is made up of two subsystems known as the parasympathetic (PNS), and the sympathetic (SNS) system. The SNS is responsible for the "flight and fight" response, which increases the metabolic rate, heart rate, blood pressure, arterial blood flow and pupil diameter. The PNS has the opposite effect. Homeostasis in the human body is partially maintained by the ANS through the controlled balance of these two subsystems. However, when a person is fatigued the pupil diameter is less likely maintained [2], and therefore the stability of the pupil diameter could serve as an important marker for EDS.

METHOD

METHOD: In this preliminary study, two male subjects (21 and 45 year old) were selected based on their self reported sleepiness, one reporting to have adequate sleep (45 year old) and the other reporting <10 hours of accumulated sleep debt. Both subjects were seated in a chair in a controlled darkened room and asked to focus on red dot projected 1 meter away on the opposite wall. Subjects were asked to relax for ten minutes to allow the adaptation of their pupils to this environment. Subjects wore a cycling helmet equipped with a USB camera (***photo below***), which was used to take a video recording of their pupil for a duration of five minutes.

A ruler was placed below the subject's eye for a few seconds prior to data collection to serve as a spatial calibration of pupil diameter. The digitized data was

collected for 5 continuous minutes, a video decompiler software was used to extract pupil images at a frequency of 30 frames per second.

Manual measurement of the horizontal pupil diameter was determined on every 10th frame for both subjects. The 900 pupil diameters measurements were arranged into a time series for further analysis.

RESULTS

The mean value and standard deviation. A difference between subjects can be seem in both mean value and in standard deviation. The mean and standard deviation of the pupil diameter were computed for both alert and sleepy subjects and are reported in ***Table 1***.

A Fast Fourier analysis was performed on each time series (***Graph 1***).

CONCLUSIONS

In this pilot study, pupil diameter (Mean Value) and pupil size instability (Standard Deviation) supported the hypothesis the pupil can be used as an important marker for EDS. A subsequent Fast Fourier analysis of a generated time series further supported this hypothesis. These preliminary results suggest that alert subject have a larger pupil diameter and a higher pupil stability (low standard deviation value). A more comprehensive study using video pupillometry to estimate the stability of the pupil diameter as a marker of EDS is warranted.

REFERENCES

[1] Moldofsky, H., Evaluation of daytime sleepiness. Clin Chest Med, 1992, 13(3):417-25.

[2] McLaren, Jay W., Hauri P.J., Lin S.C., Harris C.D, Pupillometry in clinically sleepy patients. Sleep Med, 2002, 3(4):347-352.

NSF

Table 1. Mean Value and Standard Deviation of Sleepy and Non-sleepy Subjects

	Non-Sleepy Subject (mm)	Sleepy Subject (mm)
Mean Values	5.115	4.627
Standard Deviation	0.166	0.309

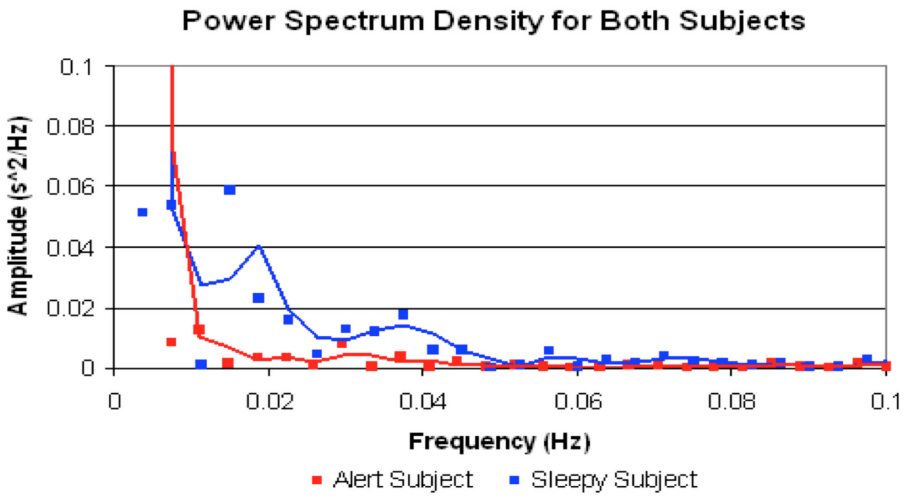

Graph 1. The relative power of the low frequency spectrum is decreased in the alert subject.

A Fourier Transformation and a Power Spectrum Density graph was computed for both subjects. A difference can be seen in the relative power at the lower end of the frequency spectrum.

Orbital Dynamics of the Earth-Moon System

By Matthew Rappeline (*Faculty Mentor*: Hervé Collin, Ph.D.)

INTRODUCTION

Gravity, which can be described as a central force, governs orbital motion in planets, stars and galaxies. The first experimental description of the motion of planets was obtained by Kepler. Later, Isaac Newton proposed a theoretical formulation of Kepler's laws using his theory of gravitation (F_g), which are based on his three laws of motion. These laws act as a predictive tool for many celestial orbits and can be stated as thus:

$$1)\sum \vec{F} = 0 \quad 2)\sum \vec{F} = \frac{d\vec{p}}{dt} \quad 3)\vec{F_{a/b}} = -\vec{F_{b/a}} \qquad \vec{F_g} = G\frac{m_1 m_2}{r^2}\hat{e}$$

The Lagrangian refined classical mechanics by including energy analysis and the principle of least action. [1] The Lagrangian (L) is defined where T is the kinetic energy of the system and U is the potential energy. The Euler-Lagrange Equation of Motion takes the general form:

$$L = T - U \qquad \frac{d}{dt}\frac{\partial L}{\partial \dot{q}} - \frac{\partial L}{\partial q}$$

These incredibly powerful tools can be used to describe and model the dynamics of almost any system.

PURPOSE

The purpose of the research is to obtain the equations of motion that model the orbital dynamics of the Moon and the Earth using 1) Newtonian Analysis and 2) Lagrangian Mechanics. First, the Earth's center of mass (C.O.M.) will be taken as the center of the system. Second, using the principle of reduced mass, The C.O.M. of the Moon/Earth System will be used as the center of the system.

Based on the theoretical prediction, the orbits of the Earth and Moon will be represented graphically and compared with experimental data from a Lunar Laser Ranging (LLR) Observatory in order to evaluate the accuracy of the theoretical model.

METHODS

All calculations are in polar coordinates, and the homogeneity of the Moon and Earth are assumed. All orbital parameters including initial conditions, are taken from NASA data [2].

Earth's C.O.M. as the Center of the System

From kinematics the total acceleration of the moon can be defined as [3]

$$a = [\ddot{r} - r(\dot{\theta})^2]\hat{e_r} + [r\ddot{\theta} + 2\dot{r}\dot{\theta}]\hat{e_\theta}$$

Starting with a Free-Body Diagram, and recognizing gravity as the only external force, Newton's second law is first used to model the force from the earth on the moon in the r and θ directions.

Here r represents the distance between the Earth's C.O.M. and the Moon's C.O.M. substituting the radial acceleration, from the previous equation, and the force due to gravity into Newton's Second Law yields the following equation.

$$\ddot{r} - r(\dot{\theta})^2 = -\frac{Gm_e}{r^2}$$

The solution to the above equation takes on the general form below.

$$u = Asin\theta + Bcos\theta + \frac{Gm_e}{r_o^2 v_o^2}$$

Here u=1/r and we use the initial conditions to find A and B. Finding the specific solution for this equation produces the Newtonian equation of motion.

Similarly, the moon's kinetic energy (T) and potential energy (U) can be defined and combined to produce the Lagrangian for the moon:

$$L = [\tfrac{1}{2}m_m((\dot{r})^2 + (r^2(\dot{\theta})^2)] + \frac{Gm_e m_m}{r}$$

Applying the general form of the Euler-Lagrange equations to the Lagrangian for the moon produces the following equation of motion. Cancelling the mass of the moon and rearranging terms yields the same equa-

tion as the Newtonian analysis.

$$[m_m\ddot{r} - [m_m r(\dot{\theta})^2 - \frac{Gm_e m_m}{r^2}] = 0$$

Earth/Moon System C.O.M. as the center of the system

To model the effect of the Moon's gravity on Earth's orbit, the principle of reduced mass is now considered [4]. Only systems united by a single, central force, ascribe to the doctrines of this principle. The total mass M is defined as $M = m_m + m_e$ and the reduced mass as $\mu = (m_m * m_e) / M$. The r here, represents $r_m - r_e$ and given that the coordinate system is centered at the C.O.M., this will be a summation of terms.

Given that the C.O.M. of the system is fixed, and that the total distance between the two bodies is constant, the individual position vectors of the moon (r_m) and the earth (r_e) can be written as:

$$r_m = \frac{m_e}{M}r,\ r_e = -\frac{m_m}{M}r$$

These reduce to an identical equation, below, as the reduced mass principle dictates.

$$\mu\ddot{r} = F$$

The reduced mass Lagrangian starts by defining the kinetic and potential energies of both the Moon and the Earth and combining them into their respective equations:

$$L_m = \tfrac{1}{2}m_m(\tfrac{m_e}{M})^2(\dot{r})^2 + g\mu r, \quad L_e = -\tfrac{1}{2}m_e(\tfrac{m_m}{M})^2(\dot{r})^2 - g\mu r$$

Again applying the general form of the Euler-Lagrange equations to the respective Lagrangians produces the following equations of motion in the direction for the Moon and the Earth. Note that these equations reduce to the same equation, for reduced mass, as the Newtonian analysis.

$$\frac{m_m m_e^2}{M^2}\ddot{r} - g\mu = 0,\ -\frac{m_e m_m^2}{M^2}\ddot{r} + g\mu = 0$$

Experimental Data

The experimental data was extracted from the Apache Point Observatory Lunar Laser Operation (APOLLO) located at Apache Point, New Mexico [5]. This site conducts weekly LLR tests and compiles the data as a series of normal points. First I extracted the 'two-way time of flight', a 14 digit value, from the normal point data and converted it to seconds. Then I multiplied this value by the speed of light to obtain the experimental distances in kilometers. These experimental distances will be compared to the theoretical distances produced by the equations.

RESULTS

Both the Newtonian and the Lagrangian analysis produce equivalent equations of motion. However, when the Earth is considered as the center of the system, the moon's equation is:

$$r(\theta) = \frac{r_o(1+e)}{1+ecos(\theta)} = \frac{383241.537}{1+(0.05489cos\theta)} \qquad (1)$$

When the Earth/Moon System C.O.M. is taken as the center of the system, the equations of motion for the moon is refined and the earth can also be obtained.

$$r_m = \frac{a_m(1-e^2)}{1+ecos(\theta)} = \frac{380263.8616}{1+0.05489(cos\theta)} \qquad (2)$$

$$r_e = \frac{a_e(1-e^2)}{1+ecos(\theta)} = -\frac{4680.9286}{1+0.05489(cos\theta)} \qquad (3)$$

The graphical representation below, produced via Octave, depicts equation (1) in light blue, (2) in red, (3) in green and the points from the experimental data (x) in dark blue.

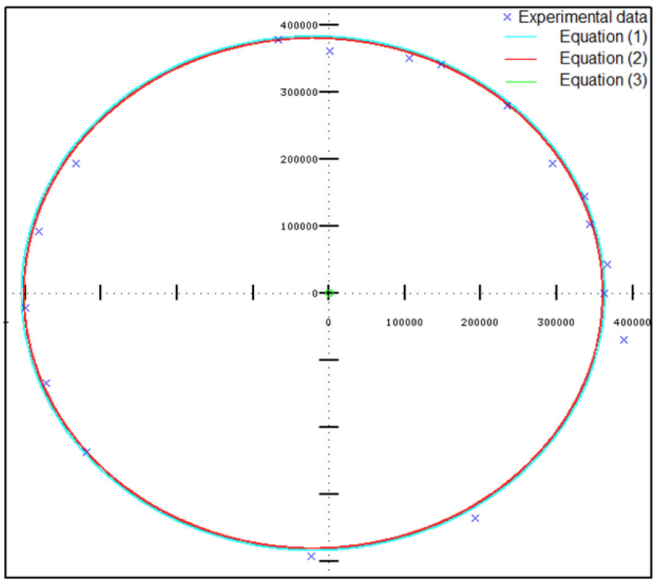

ANALYSIS

I computed the percent error from the theoretical data, from equation (1) and (2) above, against the experimental data. The average percent error with the Earth's C.O.M. as the center of the system, equation (1), was 2.58%. The average percent error with the Earth/Moon C.O.M. as the center, equation (2), was 2.38%. As expected, the model of the orbit around the Earth/Moon C.O.M. better reflects the actual dynamics of the Moon and Earth with a higher accuracy. The experimental data agrees well with the theoretical data, though for higher values of θ, the experimental is generally greater than the theoretical data.

CONCLUSION

Equivalent equations of motion were obtained from Newtonian analysis and Lagrangian Mechanics for the Moon/Earth system with 1) the Earth as the center of the system and 2) the Earth/Moon C.O.M. as the center of the system. The equations displayed a high level of accuracy when compared to the experimental data from APOLLO.

REFERENCES

[1] Marion, Jerry and Stephen Thornton. Classical Dynamics of Particles and Systems 4th ed. Orlando: Saunders College Publishing, 1995. Print. Ch. 5-9.

[2] http://nssdc.gsfc.nasa.gov/planetary/factsheet/moonfact.html

[3] Bedford, Anthony and Wallace Fowler. Engineering Mechanics: Dynamics 4th ed. New Jersey: Pearson Prentice Hall, 2005. Print. Ch. 14.

[4] http://farside.ph.utexas.edu/teaching/336k/Newton.pdf

[5] http://physics.ucsd.edu/~tmurphy/apollo/norm_pts.html

ACKNOWLEDGEMENTS

I would like to acknowledge Shea Arakaki, Dr. Hervé Collin, Dr. Aaron Hanai, Nari Okui, Keoki Noji, KapCC STEM Program, EPSCoR, as well as Peter and Nina Rappeline.

Identifying variable objects in star-forming regions using data from the Infrared Imaging Survey (IRIS)

By Matt Rappeline (*Faculty Mentor*: Dr. Klaus Hodapp)

INTRODUCTION

IRIS is a 0.8m infrared CCD telescope located at the Cerro Armazones Observatory site in Chile. It was installed in March 2010 and upgraded in November 2010. It surveys in three bands of the near-infrared, but primarily in the Ks band. It was commissioned solely for the purpose of investigating star-forming regions. IRIS has a very small field of view allowing for small high resolution images.

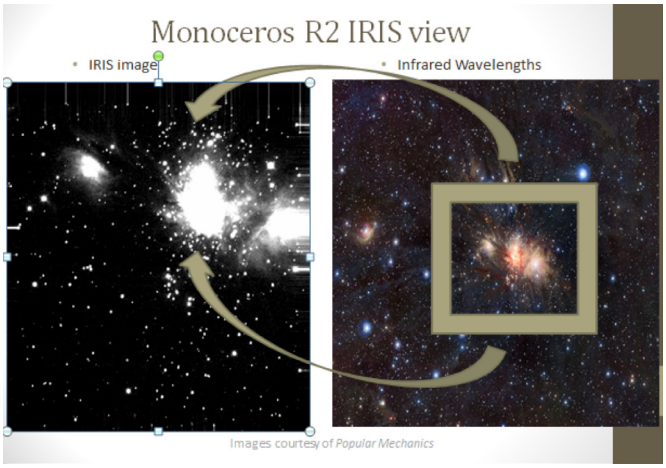

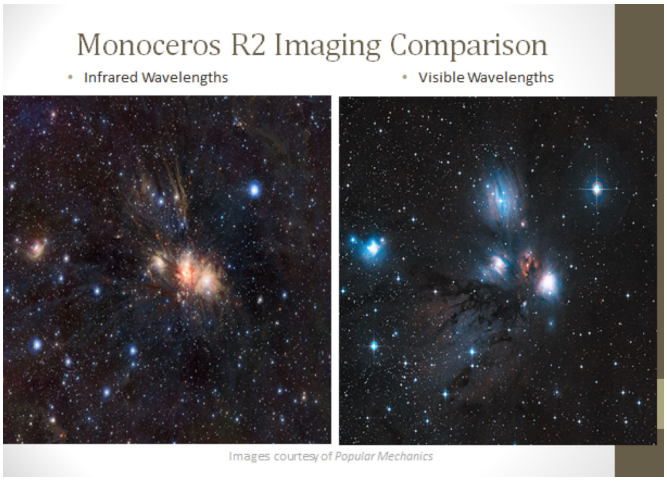

Advantages of Infrared Imaging

1. Infrared Images more easily penetrate interstellar dust and gas accretions granting increased visibility in the star-forming regions.
2. Some objects only radiate in the infrared and thus are only visible at these wavelengths

PURPOSE

The purpose of this project is to convert raw IRIS image data into a usable format for analysis. My part in this project is refining the conversion process via IRAF and C scripts and to apply this process to as many regions as possible during the internship.

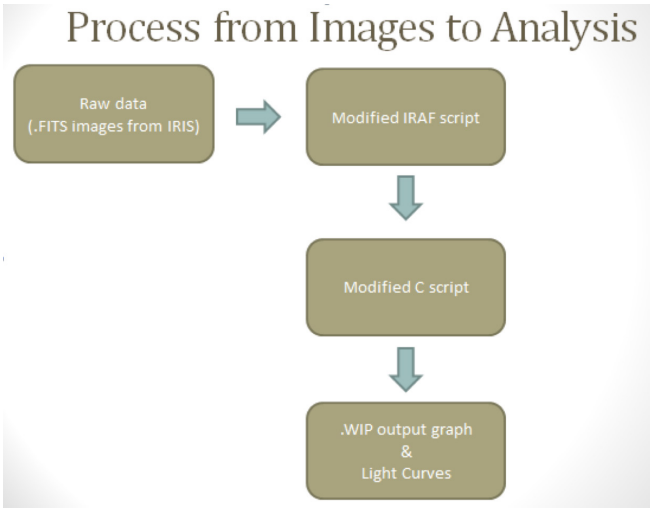

METHOD

The image processing was done in the Image Reduction and Analysis Facility software (IRAF). It is a command line prompt software in the Linux environment. In conjunction ds9 an astronomical imaging and data visualization application.

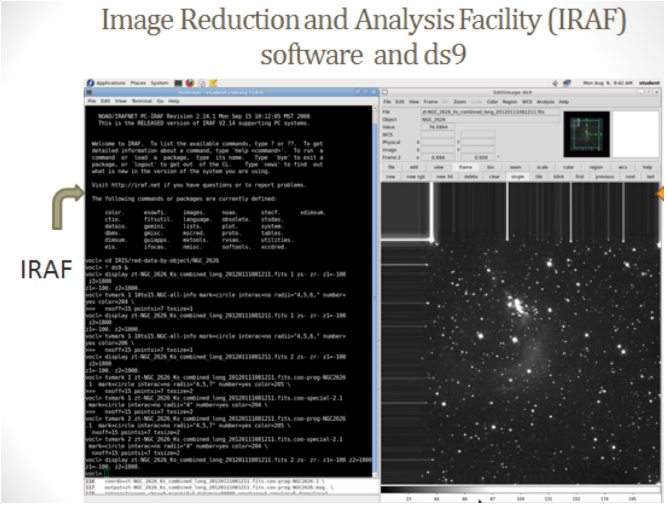

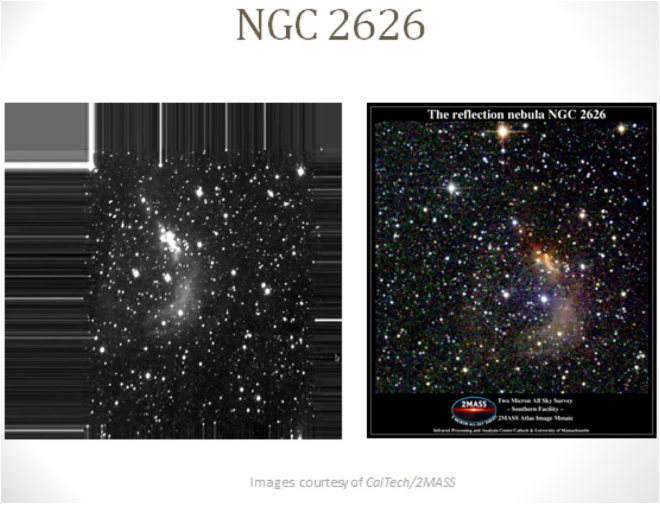

1. Retrieve and filter raw IRIS data

The IRIS data was pipelined in via a virtual machine in Germany. It initially came arranged as 111 dates on which the data was collected. I wrote a script to sort the image data into 50 directories arranged by object. Out of these 50, only 20 had sufficient data from which to extract instrumental magnitudes.

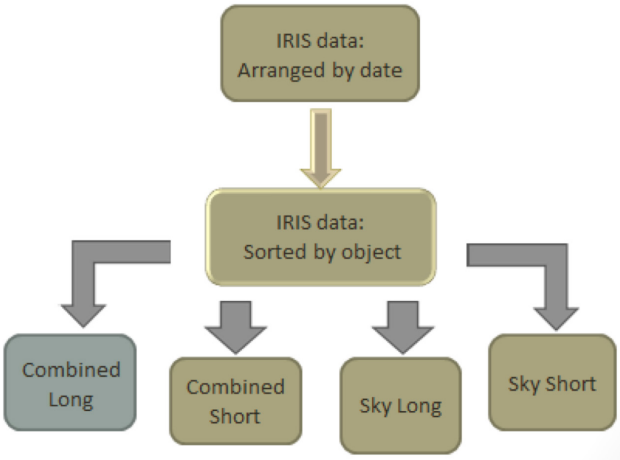

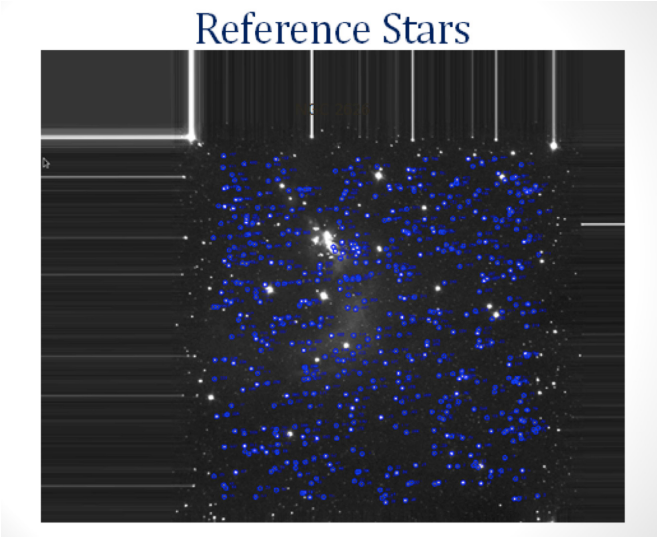

2. Identify Three Types of Stars

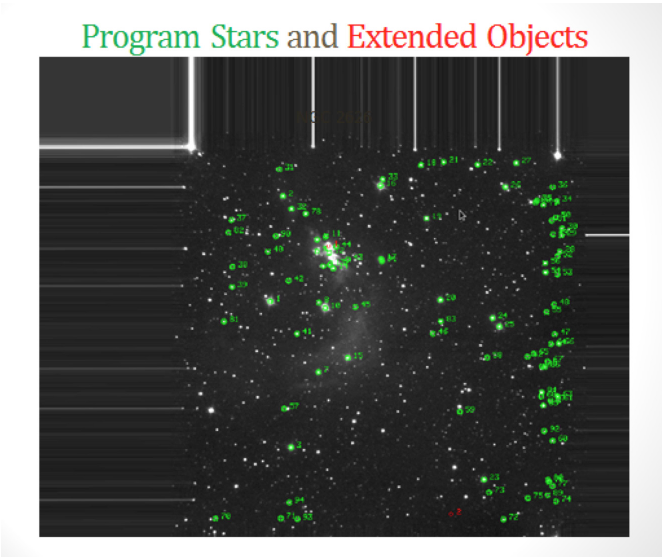

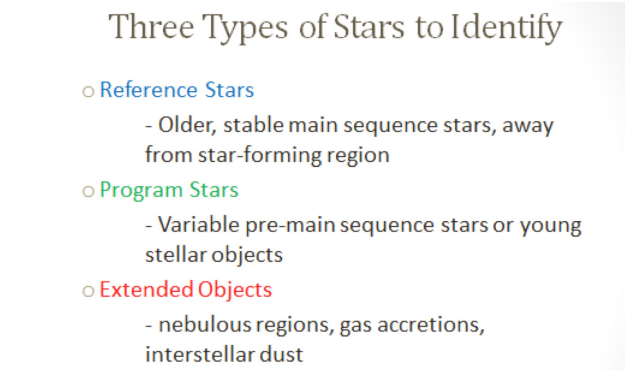

3. Extract data using IRAF

IRAF extracts instrumental magnitudes from these images containing all the marked stars. IRAF extracts instrumental magnitude data from each region during each epoch. These are then run through a C script to produce usable data for analysis.

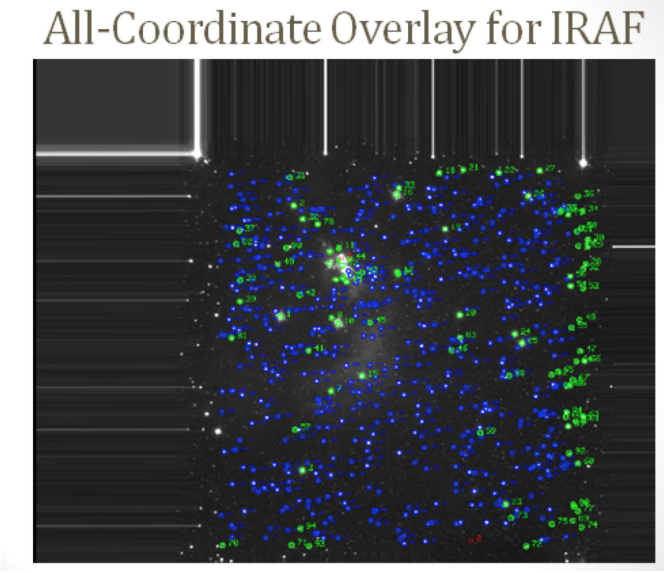

RESULTS

A C script cleans up the magnitude from IRAF and produces the .wip graph below as the final output. This graph shows all the stars over all epochs in a given star-forming region. Stars off of the blue 2MASS distribution are considered variable and any that vary on the order of 2-2.5 magnitudes or more are very interesting cases that warrant further investigation.

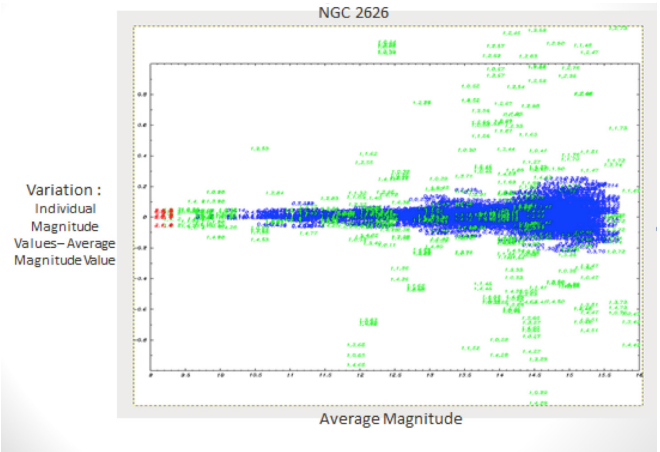

Results compared to existing studies

This shows the IRIS data compared with data from YSOVAR. YSOVAR is a Caltech study conducted using a warm Spitzer telescope. It was conducted over 40 consecutive days focused on the Orion Nebula. Note that these are not identical objects or even regions of the sky, but are presented to show similar trends in existing literature.

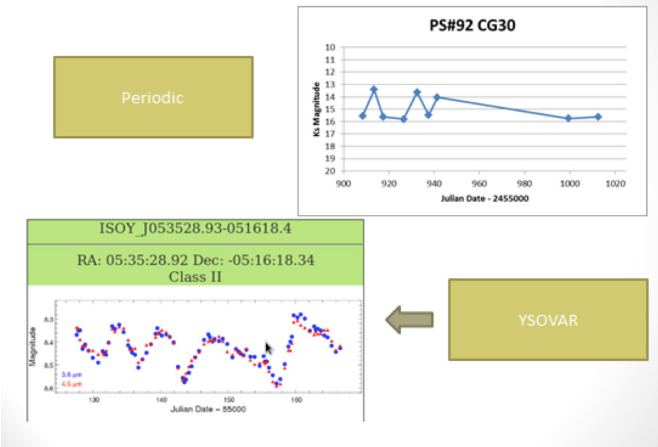

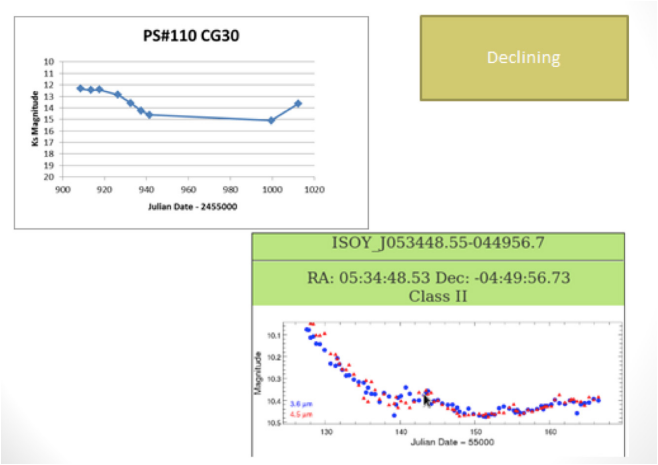

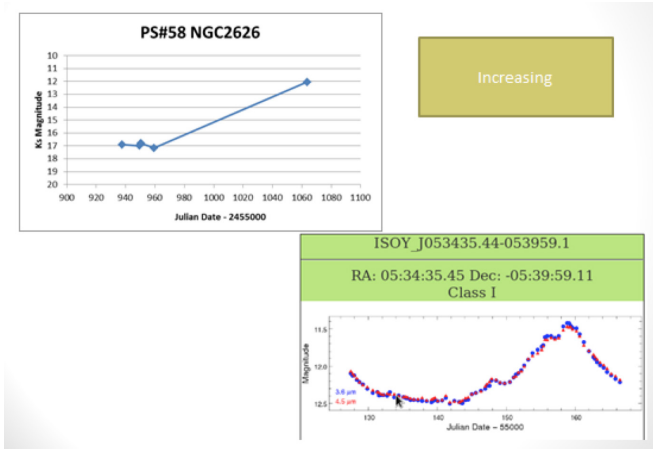

CONCLUSION

We identified several highly variable objects from this process and constructed light curves to monitor the individual, variable objects. This process will need to be continually be applied to the incoming IRIS data as it becomes available. Continued analysis of the high quality photometric data from IRIS will produce more authentic magnitude readings. The manner in which the magnitude changes will give us deeper insight into the dynamics of star formation, stellar evolution and the universe abroad

We identified several highly variable objects from this process and constructed light curves to monitor the individual, variable objects. This process will need to be continually be applied to the incoming IRIS data as it becomes available. Continued analysis of the high quality photometric data from IRIS will produce more authentic magnitude readings. The manner in which the magnitude changes will give us deeper insight into the dynamics of star formation, stellar evolution and the universe abroad.

ACKNOWLEDGEMENTS

- This material is based upon work supported by the Akamai Workforce Initiative with funding from the National Science Foundation (AST#0836053), Air Force Office of Scientific Research (FA9550-10-1-044), University of Hawaii, Air Force Research Laboratory, Kamehameha Schools, and Thirty Meter Telescope
- Institute for Astronomy
- Dr. Klaus Hodapp
- Dr. Herve Collin, Aunty Keolani Noa, Nari Okui, Keoki Noji, Shea Rappeline, Nina and Peter Rappeline, Craig and Wilma Arakaki.

Autonomous Mapping Platform

By Eric Jordan & Jeff Griffith (*Faculty Mentors*: Hervé Collin, M.S., John D. Rand, Ph.D.)

ABSTRACT

Robots have become an increasingly popular platform for data generation and remote sensing. Utilizing a suite of sensors, the Autonoous Mapping Platform (AMP) is able to generate high-resolution 3D maps. These maps can be used for accessibility mapping, historical records, security, and disaster daage evaluation. AMP is designed to semi-autonomously map an environment. This data is then processed as required by the end-user. The operator moves AMP into position. The LIDAR sensor is leveled, and AMP performs a full 460-degree scan. Once a scan is complete, GPS coordinates, linear displacement, and altittude are recorded as metadata. Once several scans have been completed of an area, the operator combines each individual scan using the metadata to produce a single high resolution 3D map. Over the next 6 months, AMP will have the capability to authomously navigate and map an environment.

INTRODUCTION

AMP is a semi-autonomous robot capable of producing high-resolution 3D maps of an environement. Using a robotic platform, we are able to collect precise and reproducible results. The high-resolution 3D maps produced by AMP have several applications, including:

- Accessibility Mapping and Evaluation
- Historical records
- Security
- Disaster damage evaluation.

Utilizing LIDAR and 3D point clouds, precise measurements between points and objects become possible. These measurements enable the precise estimate of widths between walls and entryways (accessibility requirements) as well as accurage mapping of building exterior and interior (historical records). It is also possible to detect environmental changes over time when multiple scans taken at different times are compared (security and disaster evaulation).

OBJECTIVE

The purpose of this project is to design and build a semi-authonomous robot capable of mapping urban environments for accessibility purposes by combining multiple scans to create a virtual reconstruction fo the environment.

METHOD

An operator remotely controls AMP using an Xbox 360 wireless controller. During operation, AMP collects distances traveled, elevation changes, and GPS coordinates. Once AMP has been

positioned for a scan, it rotates its two-dimensional LIDAR sensor in order to generate a three-dimensional point cloud around itself. After the robot has completed its mission, the point clouds are processed using CAD software. We are able to combine multiple scans to create a virtual reconstruction of the environment.

Mechanical

The chassis originated from an electric wheelchair. In order to accomodate extra batteries, a sensor platform, and LIDAR leveling system, the original chassis was modified. Linear actuators attach the LIDAR sensor to the chassis. Mounted on top of the linear actuators are a rotary table, stepper motor, and the LIDAR sensor. The rotary table provies a 1:72 gear reduction. Combined with the stepper motor's 1.8-degree size, AMP is capable of stepping in 0.025-degree increments.

Sensors

In order for the operator to combine multiple scans, the operator must know the precise location of each individual scan. AMP attaches GPS coordinates, dead-reckoning linear displacement, and elevation data to each scan. This metadata allows the operator to quickly move and rotate each individual scan.

Barometer: A high-resolution barometer detects the elevation of the AMP.

Global Postioning System [GPS]: A GPS sensor detects the general position of the AMP.

Hall Effect: AMP uses a dead-reckoning algorithm to determine the linear displacement between scans.

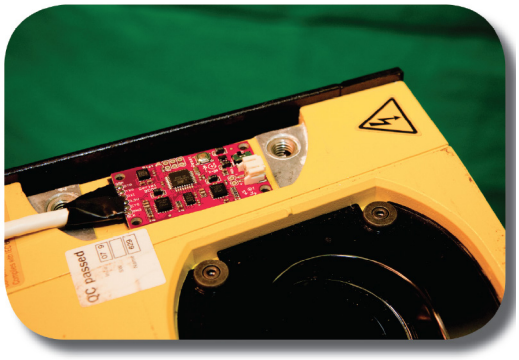

Utilizing two Hall Effect sensors per axis allows the robot to determine clockwise or counter-clockwise rotation of the wheels, and counting the number of rotations of each wheel determines the linear displacement.

Inertial Measurement Unit (IMU): The IMU provides triple axis accelerometer and magnetometer readings.

Light Detection and Ranging (LIDAR): Rotating a vertically mounted 2D LIDAR sensor 360 degrees around its center generates a 3D point cloud.

Ultra Sonic Range Finder: An ultrasonic range finder detects LIDAR sensor elevation from the chassis.

Power

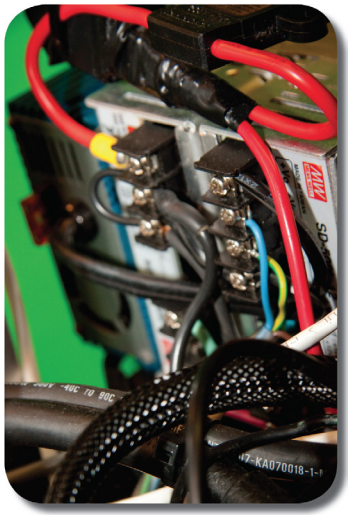

A series and parallel combination of four 12-volt deep cycle gel batteries provides 100 amp-hours at 24 volts. The 100 amp-hours provide approximately 8 hours of continuous runtime. The battery voltage is regulated to 24, 12, and 5 volts. The 24-volt regulation ensures that the rest of the system has clean power without any spikes. The 24 volts are then regulated down to 12 volts, which is used, by the wheel motors and linear actuators.

The 12 volts are regulated down to 5 volts and are used by our electronic circut.

Data Acquisition & Processing

To produce a map, several steps are required:

1. An operator moves AMP into position.
2. The linear actuators raise the LIDAR several inches and then perform leveling. The ultrasonic range finder measures the distance from the chassis to the LIDAR, as the linear actuators have no direct feedback. The accelerometers on the inertial measurement unit provide the leveling data. A single linear actuator is moved, leveling the LIDAR on a single axis. Then a second actuator is moved to level the LIDAR on the second axis.
3. The magnetometers from the inertial measurement unit are used to read the initial heading of the LIDAR sensor.
4. The LIDAR performs a single reading providing 761 distance points in a 190-degree vertical plane.
5. The stepper motor is stepped 7 times, rotating the LIDAR sensor 0.175 degrees.
6. Steps 4 and 5 are repeated until the LIDAR has rotated 360 degrees (2058 scans).
7. The individual scans are combined into a single file containing approximately 1.6 million x, y, and z-data points.
8. The GPS coordinates, elevation, initial heading, and linear displacement are written into a metadata file.
9. Steps 1-8 are repeated until the entire area to be mapped has been covered.
10. These individual scans are combined during post processing to create a virtual map. Every measurement point in these scans is accurate to within 3cm and can be used to determine changes or clearances from any computer with CAD software installed.

RESULTS

The current prototype of AMP semi-autonomously analyzes a scene and determines positions to scan. It navigates to each position, raises the LIDAR, levels it, and performs a complete 360-degree scan. After performaing a scan, AMP moves on to the next position and performs additional scans until the area has sufficient coverage. All scans are then combined in CAD software to render a three-dimensional virtual map of the scanned environment.

FUTURE DEVELOPMENT

In the near future, AMP will have full autonomous capability. This includes object detection and avoidance, basic artificial intelligence, and machine learning. This will allow AMP to perform more scans over a given time period, raising its overall efficiency.

Remote Robotic Intervention

By Arvin Niro, Makana Ramos, & Jeffery Oshiro (*Faculty Mentor*: Aaron Hanai, Ph.D.)

ABSTRACT

In 2011, multiple workers were exposed to life-threatening levels of radiation while attempting to contain the Fukushima Daiichi nuclear disaster. This incident highlighted the need for remote robotic intervention in order to minimize human injury in hazardous situations. Robotic intervention allows for safe interaction with an environment when direct human contact is not feasible or possible due to hazardous conditions. In this project we are exploring applications of holonomic movement and wireless communication utilizing a robotic platform to accomplish remote intervention tasks.

For this specific research project, we built a robot that is capable of holonomic motion, remote interaction, and also able to work wirelessly with the operator. Holonomic motion is accomplished by using four independently driven Mecanum wheels mounted to a modular chassis. The electronic control system operates on the CAN (controller area network) standard which allows for easy integration with computer based control software. The addition of the anthropomorphic robotic manipulator greatly expands the capabilities of the robotic platform by enabling precise interactive capabilities with its surroundings. Being capable of holonomic motion, having the capability of anthropomorphic interaction with the environment, and being able to be controlled wirelessly make this robot a versatile platform for accomplishing remote intervention tasks. Remote robotic intervention will become the standard method for responding to life-threatening situations in the future.

GOAL

Our goal was to drive the robot across campus, grab a drink and bring it back. The goal is not only about the task, but about the things that make the task possible such as communication and maneuverability.

FEATURES

- 2 CAN
- Canipede
- TrendNet Wireless Router
- AX-18A Smart Arm
- Mecanum Wheels

RESEARCH

- Benefits of CAN Communication
- Mobility achieved by Holonomic Motion
- Integration of robotic smart arm

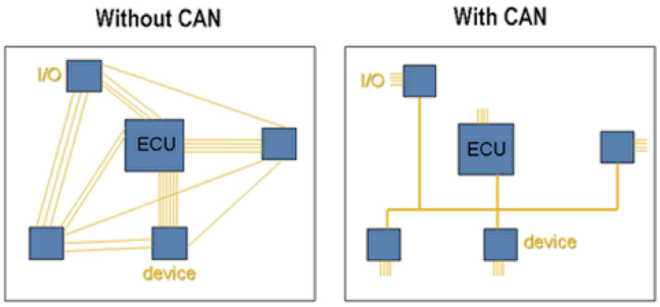

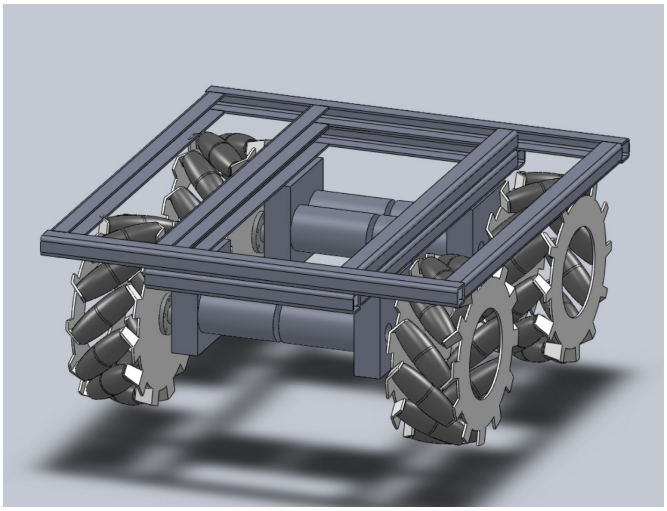

FUTURE GOALS

- Integrate smart arm & webcam
- Redesign chassis
- Set up wireless communications (mobile hotspots, WIFI)

Implementing Intelligent Electronic Traction Control Systems in Robotic Platforms

By Arvin Niro, Makana Ramos, and Lee Do (*Faculty Mentor*: Aaron Hanai, Ph.D.)

ABSTRACT

Automobiles have a unique way of distributing power to two or four wheels via a differential. This simple piece of automotive engineering has proven to be useful in contemporary vehicles when faced with tire slippage. Differentials solve this problem by means of a traction control system in order to distribute the power elsewhere to regain traction. Implementing an electronic traction control system onto a robotic platform can serve as an intelligent traction systems to control each individual wheel.

PURPOSE

In this project, we aim to supersede the concept of the differential by implementing an intelligent electronic traction control system onto our robotic vehicle. Our robot is outfitted with four mecanum wheels, each individually driven by a motor. By monitoring each wheel's angular velocity and current/torque, we can determine when a wheel is slipping and therefore adjust the slipping wheel in order to regain traction.

INTRODUCTION

Traction control is defined as a system that helps limit the tire slip due to acceleration on slippery platforms. Differentials are used to help tires regain traction by controlling the output level of torque in the motors which allows each wheel to rotate at different velocities. Figure 1 displays some of the components used in a traction control system.

According to research done by Hanai, Marani, and Choi (2010), they developed an automatic thrust redistribution algorithm for an underwater vehicle to generate a solution to help distribute the thruster forces to each motor when one is losing thrust while still trying to maintain the desired motion. In other research done by Hartani, Bourahla, Miloud, and Sekour (2009),

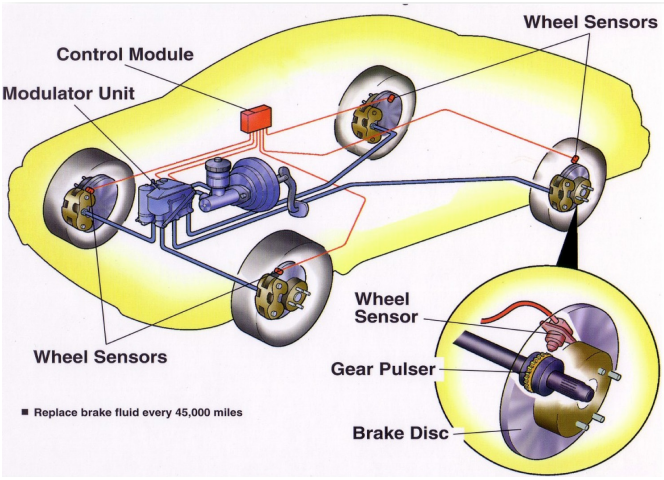

Figure 1. Traction Control System, http://hda-bob.com/the-vehicle/traction-control/

they mentioned that by having a motor for each wheel on a vehicle, it increases the vehicle's power and weight distribution without the use of transmissions, drive shafts, and differentials by monitoring each wheel's drive torque and braking force. Because each wheel is individually driven by a motor, there is no power loss between the differential gear , thus the stability of the vehicle is increased.

For our research, our robot is outfitted with four mecanum wheels, each wheel individually driven by a motor. Similar to the research done by Dr. Hartani, we can measure each individual wheel's angular velocity through encoders as well as the amount of current being supplied to each motor through motor controllers. Equipping our robot with mecanum wheels allows our robot to achieve a special motion called holonomic motion. Holonomic motion is defined as being able to control all of the degrees of freedom (DOF) that a rigid body system has. These degrees of freedom can be seen in ***Figure 2*** **(see page 78)**. The uniqueness of holonomic motion allows our robot to maneuver in any direction without disrupting its orientation.

Mecanum wheels are special wheels with rollers

mounted at a 45˚ around the entire wheel. When the rollers are configured to look like an "X," this allows the robot to achieve holonomic motion.

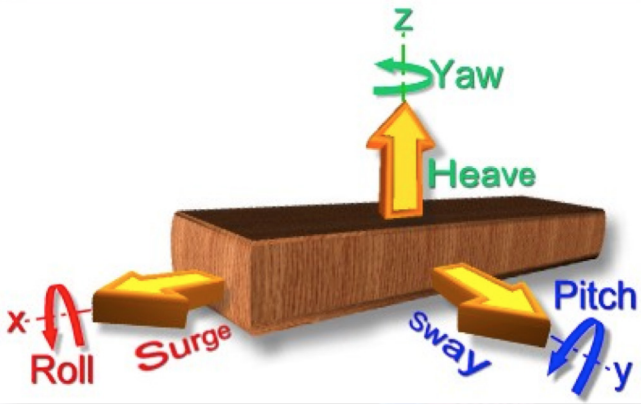

Figure 2. Degrees of Freedom, http://www.world-wideflood.com/ark/anti_broaching/wave_yaw.htm

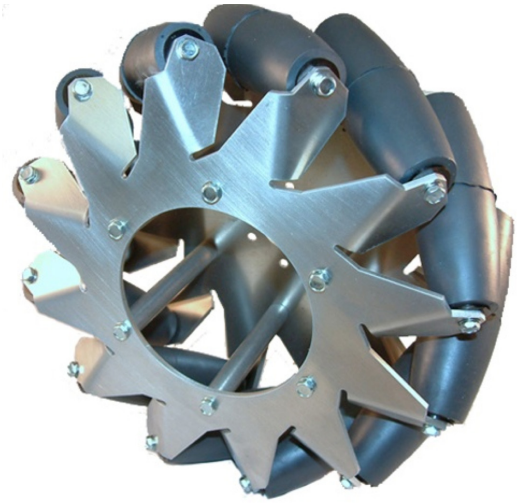

Figure 3. 10" Mecanum Wheel, http://www.andymark.com/product-p/am-0583.htm

METHOD

Before collecting data, our group brainstormed a list of possible scenarios where a wheel may lose traction and constructed a list of solutions to each scenario. These heuristic rules served as our foundation for our project.

To define a Traction Coefficient we performed three main experiments:

- Run the robot under normal conditions.
- Simulate one wheel slipping under normal conditions.
- Adjust conditions to regained control of the robot.

Our experiments addressed a specific scenario where the front left wheel (wheel 3 in ***Figure 4***) started to slip while we were driving forward approximately five meters along a straight path.

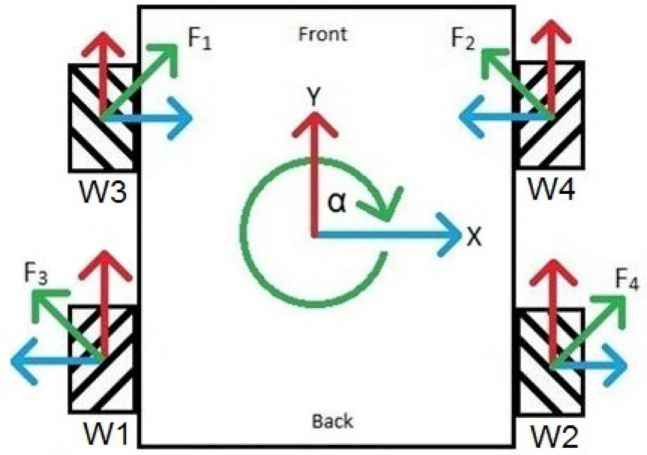

Figure 4. Vector components of our robot

Experiment 1
Experiment 1 served as our control in which the robot drove forward with all four mecanum wheels with good traction. This process was repeated 10 times, recording the current and angular velocity of each wheel.

Experiment 2
Experiment 2 served as a slipping condition where wheel 3 was slipping, therefore indicating there was no traction. Given the same forward input as the first experiment, the robot drove forward but consistently drifted off to the right due to the force vectors of each wheel. This process was repeated 10 times, recording the current and angular velocity of each wheel.

Experiment 3
According to our heuristic rules, we supplied more current to the third motor in order to compensate for the simulated slipping wheel of motor two. By applying extra current to the third motor the robot should have followed the straight path ending up in the same position as it did in the experiment 1. This process was repeated 10 times, recording the current and angular velocity of each wheel.

To define our Traction Coefficient, we needed to convert the data into SI units. To do this, we use

Equations 1 & 2. Then to find our Traction Coefficient, we use Equation 3.

$$\text{Normalized Velocity} = \frac{\left(\frac{\text{Encoder Value}}{\text{Encoder CPR}}\right)}{\text{Free Motor Speed}} \quad \text{(Equation 1)}$$

$$\text{Normalized Torque} = \frac{\left(\text{Measured Amps} \times \text{Motor Constant}\right)}{\text{Stall Torque}} \quad \text{(Equation 2)}$$

$$\text{Normalized Traction Coefficient} = \frac{\text{Normalized Torque}}{\text{Normalized Velocity}} \quad \text{(Equation 3)}$$

RESULTS

Using encoders and motor controllers, we measured the velocity and current of each wheel in order to measure and determine when a wheel would be slipping.

We defined our normalized traction coefficient to be 10.3. This was calculated using Equations 1-3. This coefficient served as our control, meaning when all four wheels had perfectly even traction, the robot would move forward. If the coefficient were to be higher or lower than the normalized traction coefficient, then it would indicate that one of the wheels is either slipping or locked. In experiment 2, we calculated our slipping coefficient to be 9.6, which clearly indicates that wheel 3 is slipping. ***Figure 5*** (***below***) displays the relationship between these two numbers.

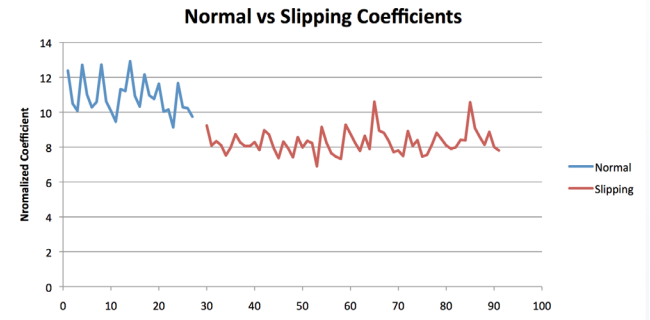

Figure 5

Figures 6 & 7 (***right column***) display the behaviors of motor 2 and motor 3.

FUTURE RESEARCH

In our current research, we utilized a low level "open-loop" traction control system where modifications to the robot were controlled through human input. In future research, we plan to implement a higher level "closed-loop" traction control system where the computer will be able make modifications based on given inputs from the encoders/sensors/and human input.

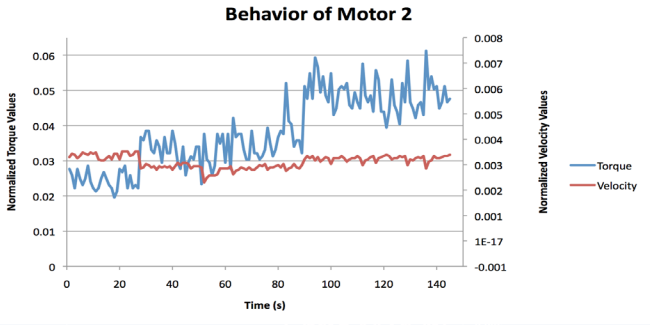

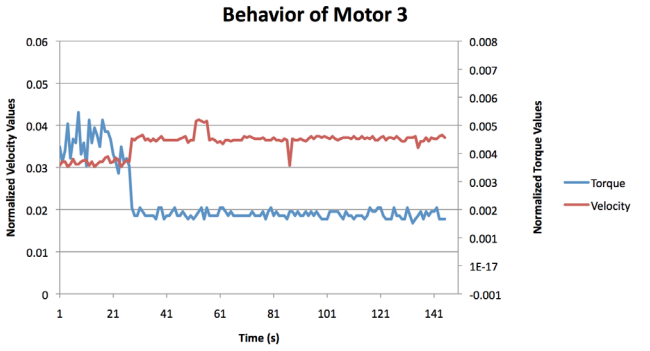

To expand our robot's capabilities, we plan to integrate an onboard GPS navigation system (***Figure 8, below***), gyros and accelerometers (***Figure 9, page 80***), as well as an anthropomorphic robotic arm, specifically the AX-18A robotic arm made by CrustCrawler Robotics (***Figure 10, page 80***). With these components, they will expand our robot's capabilities to better interact with, and be aware of its environment.

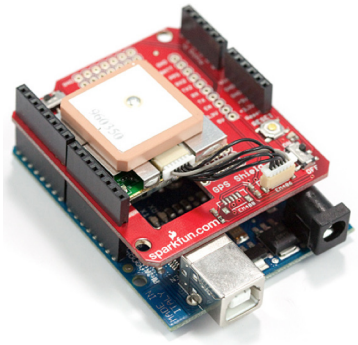

Figure 8. GPS Shield, https://www.sparkfun.com/products/9487

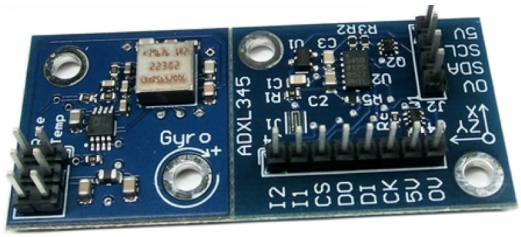

Figure 9. Gyro and Accelerometer, http://www.andymark.com/product-p/am-2067.htm

Figure 10. AX-18A Robotic Smart Arm, http://www.crustcrawler.com/products/AX-18F%20Smart%20Robotic%20Arm/

CONCLUSIONS

Throughout this project, we have demonstrated that our robot has achieved a electronic traction control system. By applying extra power to the wheel opposite of the slipping wheel, we were able to maintain a forward motion, even with a slipping wheel.

This type of electronic traction control system is already in use in automobiles, specifically electric vehicles. By being able to monitor each individual wheel, the onboard computer system is able adjust each wheel's' velocity and current being supplied, therefore allowing for a stable ride. Benefits of this electronic system allow for mechanical systems to be replaced, therefore increasing the life span of the electronic traction system.

REFERENCES

Hanai, A., Marani, G., Choi, S.K. "Automatic fault-accommodating thrust redistribution for a redundant AUV". Proceedings of the 5th JSME International Conference on Advanced Mechatronics. Osaka, Japan. Oct 2010K.

Hartani, K., Bourahla, M., Miloud, Y., Sekour, M. "Electronic Differential with Direct Torque Fuzzy Control for Vehicle Propulsion System". Turk J Elec Eng & Comp Sci, Vol.17, No.1, pp 22, 2009.

ACKNOWLEDGEMENTS

Acknowledgements: Big mahalo to our mentor Dr. Aaron Hanai for providing insight and assistance with the project, Dr. Hervé Collin for providing additional assistance, KCC STEM Program for allowing us to use the facilities, and NSF for their monetary support.

Design and Control of an Interactive Self-balancing Robot

By Liem Nguyen and Holm Smidt (*Faculty Mentor*: Hervé Collin, Ph.D.)

INTRODUCTION

A two-wheeled self-balancing robot relies on the Segway concept, which classically is the problem of balancing an inverted pendulum. The problem with balancing an inverted pendulum is the external torque on the system due to horizontal and vertical accelerations caused by gravity given an angular displacement with the vertical. To counteract this imposed torque and maintain balance, an equal and opposite torque must be imposed on the system. The amount of torque and hence acceleration imposed is dependent on the angular displacement of the system and the angle theta between the system and the vertical.

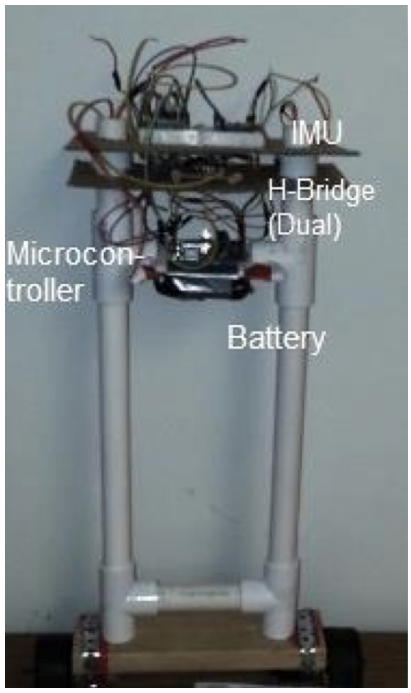

Using simple geometry and small angle approximation, we can express the displacement angle as a function of acceleration.

Our robot uses an Inertial Measurement Unit (IMU) to determine the accelerations it is experiencing, which are then converted to the pitch angle and its direction using an IMU algorithm. Data from the IMU is then sent to the PID controller to activate the motors. The PID control algorithm will determine and signal to the motors which direction to go and how fast, in order to keep the angle theta relatively small and balanced. The continuous loop of executing IMU and PID controller keeps the two wheeled robot balanced.

PURPOSE

The purpose of this research is to develop a self-balancing robot capable of interacting with and responding to its environment through the use of Ultrasonic Range Finders and also to design a dead reckoning system to determine the position of the robot.

For the self-balanced robot to rove with a top heavy load of electronics, high torque produced at the wheels is of more importance than high rpm-output. We were able to design a gearbox , composed of spur gears and drive shaft, which attaches to the motors to give us an efficient conversion from high rpm to low rpm with high torque on the wheels. The resulting ratio of input to output is an 1:100 gear ratio.

Inertial Measurement Unit (IMU)

IMU's are composed of accelerometer and gyroscope (sometimes also magnetometer) and are used to obtain velocity, orientation and forces on an object, which in turns makes IMU's useful in navigating objects. Neither accelerometer nor gyroscope could be used by itself due to vulnerability to mechanical noises (accelerometer) and problems with "zeroing" after measuring the rate of change in inclination (gyroscope); however, by applying a simplified version of the Kalman Filter on the sensor fusion, one can obtain a reliable angle of inclination.

The chart below shows inclination angle versus time

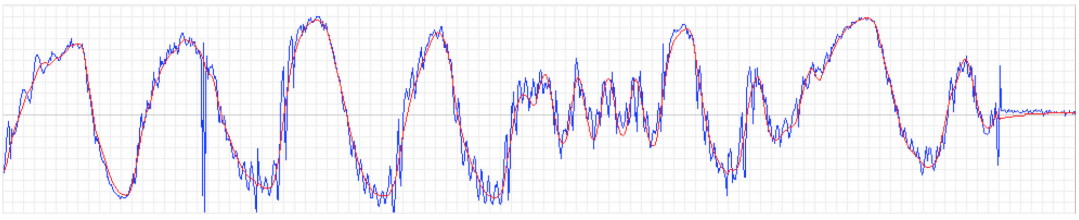

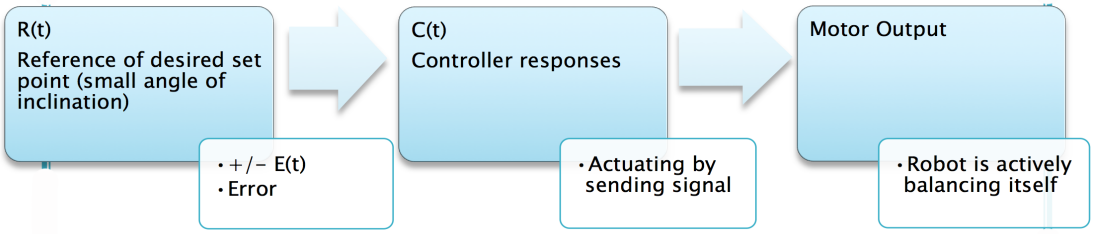

Graphic 2: Simplified PID Control System Model

determined by accelerometer itself in blue and by IMU in red. The applied filter smoothens out the mechanical noises of the accelerometer; yet, it doesn't cause any lag of the data.

PID Controller

Graphic 2 shows the basic concept of the simplified PID motor controller. In our case, R(t) resembles the centered position where the inclination angle is zero and the error E(t) is the difference between the inclination angle provided by the IMU and the desired angle of zero. The PID algorithm utilizes three constant parameters: the proportional, integral, and derivative values.

Equations used to evaluate the proportional, integral, and derivative terms are combined to determine C(t). C(t) dictates the direction and speed of the motor's spin, which is the direction and magnitude of the necessary acceleration and torque to keep the robot balanced.

Gearbox

For the self-balanced robot to rove with a top heavy load of electronics, high torque produced at the wheels is of more importance than high rpm-output. We were able to design a gearbox , composed of spur gears and drive shaft, which attaches to the motors to give us an efficient conversion from high rpm to low rpm with high torque on the wheels. The resulting ratio of input to output is an 1:100 gear ratio.

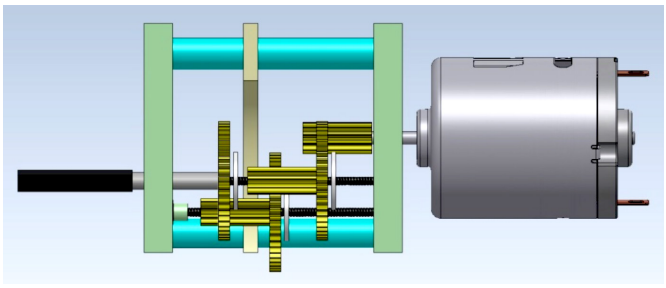

RESULTS

- Construction of two-wheeled robot with high torque gear drive system
- Developed IMU and PID algorithm for self-balancing
- Successful IMU and PID algorithm test with robot's drive motors

FUTURE RESEARCH

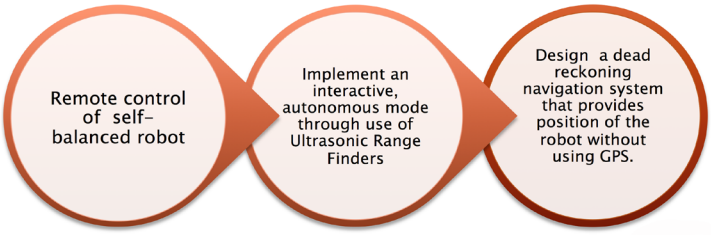

ACKNOWLEDGEMENTS

We would like to thank our devoted mentor, Dr. Hervé Collin, for his time, detailed critiques, and willingness to go out of his way to assist with our project. We would also like to thank the KCC STEM program for the use of their facilities and the NSF for their support.

Thrust Force Analysis of a Rotating Ionocraft under High Voltage

By Rae-Zan Belen (*Faculty Mentor*: Hervé Collin, Ph.D.)

INTRODUCTION

In the early 1920s, Brown and Biefeld [1], [2] discovered that when a very high voltage is applied to an asymmetric capacitor, a force is produced parallel to the electrodes and causes a thrust in the direction of the positive one. Modifying the geometry of the asymmetric capacitor results in a lightweight ionocraft or "lifter," that may represent a candidate for an alternative novel propulsion system with no moving parts. The potential of this ionocraft to revolutionize future transports with a novel technology has piqued the interest of the US Army [3], [4], the US Navy [5], NASA [6], as well as private companies such as the Honda Corporation [7].

Since the discovery of this thrust force in the nineteen twenties, its origin has been highly speculated upon, and is still poorly understood. There have been several theories proposed to predict the magnitude and origin of this force. The leading theory involves the ionic wind effect (Biefeld-Brown), which describes the polarization of air molecules as the source of propulsion. Other speculative theories also include electrogravitics, which consider antigravity as a possible source. None of these theories however are able to predict the correct magnitude of the thrust force (three order of magnitude lower) [3].

An additional difficulty arises when attempting to experimentally measure the thrust force through kinematic variables due to the high variation of motion of the ionocraft's lift. If the kinematic variables prove to be a reliable method to infer the dynamics of the system, it is essential to control its motion. Therefore, in this experiment, we decided to constraint the ionocraft into a controlled rotational configuration in order to analyze the ionocraft's motion on a fixed flight path.

PURPOSE

The purpose of this research is to confirm the constant behavior and magnitude of the thrust force of an ionocraft constrained to move in a circular motion.

METHOD

The method employed in this experiment involved the use of Newton's second law $\boldsymbol{\Sigma \tau = I\alpha}$, to derive the theoretical functional form of the angular displacement of the lifter $\boldsymbol{\theta}$ ($\boldsymbol{t}$) a function of the thrust force ($\boldsymbol{F}$), the moment of inertia ($\boldsymbol{I}$), the position of the center of mass of the lifter ($\boldsymbol{r}$), and the frictional force ($\boldsymbol{f}$). The experimental angular displacement was then measured, and a nonlinear regression was performed to match the theoretical function with the experimental data by adjusting the value of the thrust force $\boldsymbol{F}$.

Design Of The Experimental Set-Up

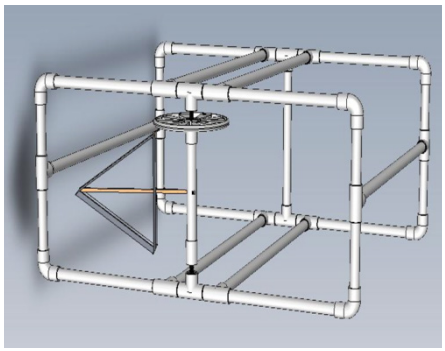

First, the system was designed on SolidWorks in order to obtain necessary values required to fit the theoretical model.

In order to perform a regression analysis between the theoretical model of $\boldsymbol{\theta}$ ($\boldsymbol{t}$) and the experimental data, the knowledge of 2 essential values are required: the moment of inertia of the lifter ($\boldsymbol{I}$) and the location of its center of mass ($\boldsymbol{r}$) with respect to the rotating shaft. Since our system is rotating perpendicular to the force due to gravity, the mass of the system was not considered explicitly (it only affected the moment of inertia of the system).

SEQUENCE OF DATA ACQUISITION

1) Frictional force

The friction present in our system comes from three sources: the drag, the friction in the bearings, and the surface friction. We considered two possible models for

the frictional force: $f = kv$ and $f = kv^2$. We derived the functional form of the theoretical angular displacement as a function of time t using both models. Applying Newton's second law $-rf = Ia$, we first rewrote our equation in terms of the angular velocity

$$(-r^2 k\omega = I\frac{d\omega}{dt},\ \text{and}\ -r^3 k\omega^2 = I\frac{d\omega}{dt})$$

separated the variables t from w, integrated once, separated our variables t and θ once more before integrating a second time. ***Table 1 below*** (***theoretical prediction of the angular displacement as a function of time for each model of the frictional force***) shows our final prediction for both models:

$f = kv$	$\theta(t) = -\frac{\omega_0 I}{kr^2}(e^{-\frac{kr^2 t}{I}} - 1)$
$f = kv^2$	$\theta(t) = \frac{I}{kr^3} ln(\frac{I + \omega_0 kr^3 t}{I})$

In order to estimate the frictional force present in our system, we gave an initial angular velocity to our rotating system and let it rotate freely until it stops while measuring the angular displacement with respect to time. A nonlinear regression analysis was then performed between each theoretical model of the angular displacement and the experimental data in order to obtain the value of k. The magnitude of the error given by GnuPlot for each value was used to identify which model of the frictional force best fit our data (smallest error in the k value).

2) Powered system

The second stage of the experiment was to power our ionocraft with 40kV volts from rest, and let it rotate for 60 seconds while measuring the angular displacement with respect to time. We proceeded in a similar manner as for the frictional force method, but also included the thrust force in our derivation: -rf + rF = Ia. The following equation for the angular displacement as a function time was obtained:

$$\theta(t) = \frac{F}{kr}(t + \frac{I}{kr^2}e^{\frac{-kr^2 t}{I}} + \frac{I}{kr^2})\ \ (1)$$

A nonlinear regression was performed again between the above equation and the experimental data of our powered system to adjust the optimum value of the thrust force F in order to obtain the best possible fit.

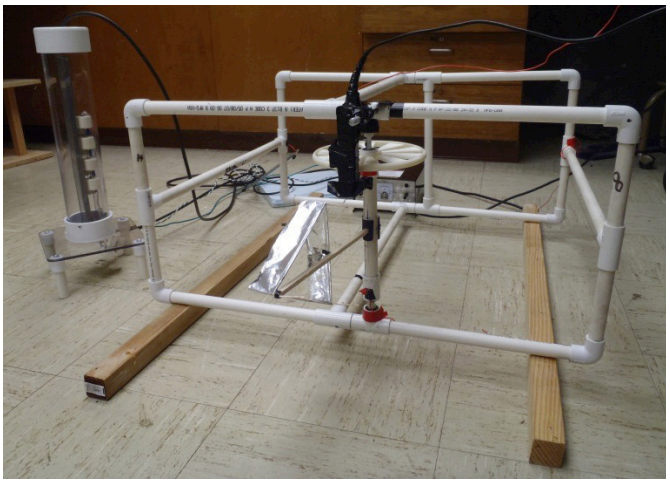

RESULTS

The two necessary experimental values obtained from Solidworks were the moment of inertia (I = 0.00155 kg m^2), and the distance of the ionocraft's center of mass with respect to the center of mass of the rotating shaft (r = 0.135 m). The results of the regression analysis to obtain the optimum value of for the frictional force are given in the ***table 2 below (k values obtained from regression analysis for each model of the frictional force***). Since the uncertainty is smaller for $f = kv$, the precision of the best fit and of k is higher and this model is chosen.

$f = kv$	$k = 0.0240 \pm 0.0008$
$f = kv^2$	$k = 0.0405 \pm 0.0028$

Based on the value of our uncertainties, $f = kv$ appeared to be the most adequate model as confirmed

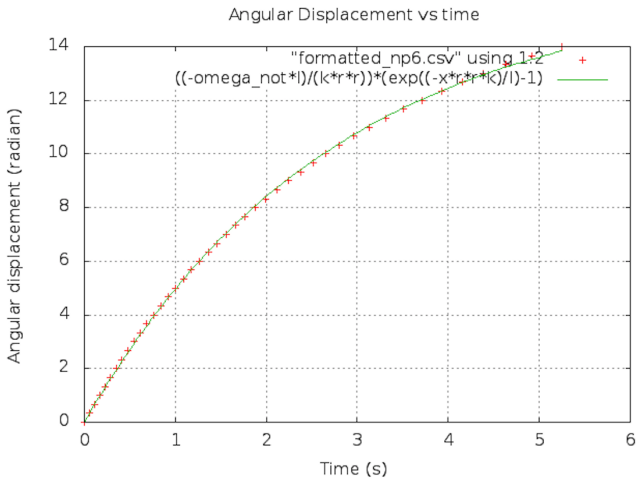

Figure 1: Nonlinear Regression using $f = kv$.

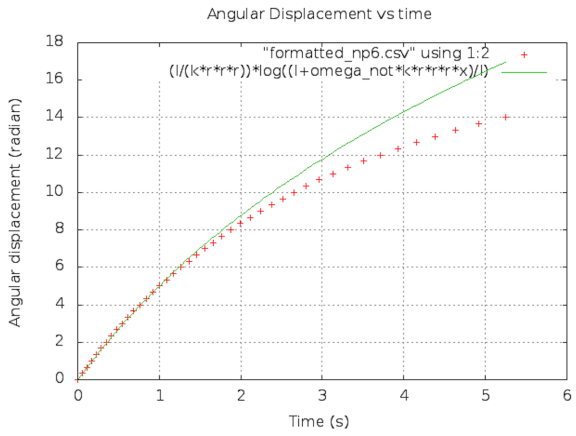

Figure 2: Nonlinear Regression using $f = kv^2$.

by a visual inspection of each case treated.

The results of the regression analysis performed using data obtained from the ionocraft system powered by 40kV, and equation (1), provided the following value for the thrust force: F=0.029856 +/- 0.000273 N.

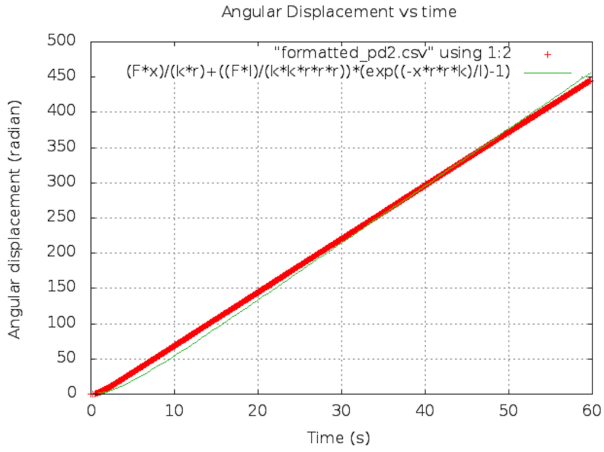

Figure 3: Linear Regression using Equation (1).

DISCUSSION AND CONCLUSION

Although I initially thought the model $f = kv^2$ would have been the best fit, after obtaining the frictional force value, the model $f = kv$ turned out to be the best fit to determine the thrust force. Throughout this project, I have made progress by determining the theoretical analysis for the horizontal configuration of the rotating ionocraft system. I evaluated the torque and found the equation of the angular displacement of the rotating system. The best fit equation for the angular displacement was determined as

$$\theta(t) = \frac{F}{kr}\left(t + \frac{I}{kr^2}e^{\frac{-kr^2t}{I}} + \frac{I}{kr^2}\right).$$

From here, the equation was evaluated assuming that the system started at rest with a friction directly proportional to the velocity where the thrust force was determined as 0.029856 +/- 0.000273 N. Although the thrust force value was determined, there is still a lot of work that needs to be done to complete the theoretical analysis of the rotating ionocraft system.

FUTURE RESEARCH

In the future, I could 1) decouple the friction term into three different distinct types in order to obtain a better accuracy 2) increasing the number of ionocrafts in our configuration to confirm that the magnitude of the thrust force is simply additive (by a factor of n in our theoretical prediction). In order to achieve a better frictional force model, we will need to get better bearings for the configuration and obtain precise values of the frictional coefficients from the manufacture.

REFERENCES

[1] Brown, Thomas T. "How I Control Gravity". Science and Invention. August 1929.

[2] Brown, Thomas T. "Electrokinetic Apparatus". "U.S. Patent No. 2,949,550'. August 16,1960.

[3] Bahder ,Thomas B. & Chris Fozi, "Force on an Asymmetric Capacitor," Army Research Laboratory, March 2003.

[4] Miller,William M., Paul B. Miller, Timothy J Drummond. "Force Characteristics of Asymmetrical Capacitor Thrusters in Air," Army Research Lab-TR-3005, Dec 2002.

[5] United State Department of Labor. "Ozone Chemical Sampling Information" http://www.osha.gov/dts/chemicalsampling/data/CH_259300.html.

[6] "Is ablation responsible for Asymmetric Capacitor Thrust in Vacuum?" Proposal by Quantum Potential Corporation in response to 2011 NASA SBIR Solicitation, Web pdf.

[7] Martins, Alexandre A. "Modeling of an EHD Corona Flow in Nitrogen Gas Using an Asymmetric Capacitor for Propulsion." Journal of Electrostatics, Vol 69, Issue 2, 133–138, April 2011.

ACKNOWLEDGEMENTS

I would like to acknowledge the National Science Foundation for the funding they have provided to support my research, my advisor Dr. Hervé Collin, our STEM Coordinator Mrs. Keolani Noa, the Kapi`olani Community College STEM Program, Logan Tamayo, Michelle Chu, James Bynes, and Lisa Kotowski. Much mahalo to my family and friends for their support towards the completion of this project.

CanSat 2013

By Kelsey Kawaguchi, Diamond Tachera, Rae-Zan Belen, McClyde Gaborno, Taylor Viti, Logan Tamayo, and Joshua Tamayo (*Faculty Mentor*: Hervé Collin, Ph.D.)

INTRODUCTION

The International CanSat Competition, sponsored by the American Astronautical Society (AAS), the American Institute of Aeronautics and Astronautics (AIAA), and NASA, is an annual event that engages undergraduate and graduate students in the design, the fabrication, and the launch of a satellite-like system in a space-related mission. This mission simulates a sensor payload traveling through a planetary atmosphere sampling the atmospheric composition during descent.

OBJECTIVES

The objectives of the 2013 mission are to:

1. Provide a safe flight and landing for an egg while collecting data and performing various maneuvers.
2. Deploy a container from a rocket at approximately 670 meters above earth surface.
3. Control the descent rate of the payload with a passive control system at 20 m/s until 400 meters.
4. Release the payload from the container and deploy an aero-breaking system responsible for actively control the descent rate to 20 m/s.
5. Transmit telemetry data throughout the duration of the entire flight, and display in real time at the Ground Control Station (GCS).

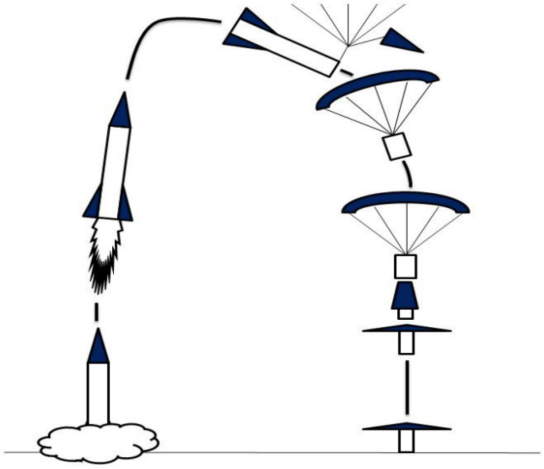

Figure 1. System Concept of Operation

6. Measure the impact force of the lander at a frequency of 100 Hz.

METHOD

The design process has been broken down in several main subsystems aligned with the mission requirement guidelines:

- Physical Layout
- Descent Rate Control
- Deployment Mechanism and Aero breaking Structure
- Sensors and Communications

Physical Layout

The Cansat is composed of two systems: a payload (***Figure 2***) and a container (***Figure 3***). The container's role is to protect the payload from apogee to 400 meters, and control the descent rate with a parachute.

Figure 2 (Left). Physical layout of the payload.

Figure 3 (Above). Container connected to the parachute.

Descent Rate Control

The first deployment occurs at apogee, an altitude of approximately 700m. The passive descent control system, a parachute, must ensure that the rate of the Cansat is 20m/s until 500m. In order to design and

predict the parachute diameter D, equation (1) is used:

$$D = \sqrt{\frac{8mg}{\pi \rho C_D v^2}} \quad (1)$$

Where ***m*** is the mass, ***g*** the acceleration due to gravity, **ρ** the density of the air, C_D the drag coefficient, and ***v*** the requirement descent rate.

Deployment Mechanism and Aero Breaking Structure

At 500m above earth surface, the sensor payload must deploy itself from the container and is required to utilize its own active descent control system until landing. The deployment mechanism is controlled by the rotation of two servos that releases the base of the container at 400 meters.

The payload is able to slide out of the container, and triggers its active descent rate mechanism with four springs located at the spill hole of the aero breaking system, as shown in ***Figure 4***.

Sensors and Communications

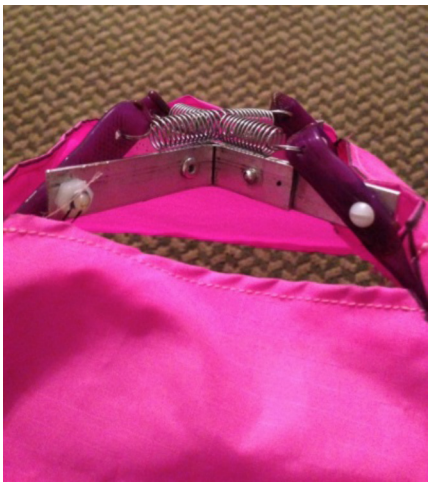

Figure 4. Servos mounted in Tier 1

The sensor payload that was utilized in this project, as shown in ***Table 1***, was composed of one microcontroller, four main sensors, and two types of receiver/transmitters.

All sensors are mounted on several layers (***Figure 5***) and placed on PCB boards (***Figure 6***) that have been designed and built specifically for this payload, in agreement to all dimensional and physical constraints dictated by the competition rules.

MCU	*Arduino Nano*
Barometric sensor and Air Temperature	*Bosch BMP180*
GPS	*EM406A*
3-axis accelerometer sensor	*SEN-10345*
Voltage and current sensor	*ACS712*
Transceiver	*Xbee Series 1*
Receiver (Antenna)	*A25-FNF*

Table 1: Sensors mounted in the payload.

RESULTS

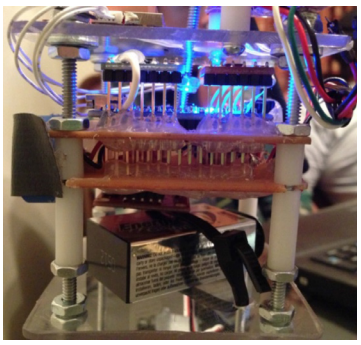

Figure 5 (Above). Sensor Payload

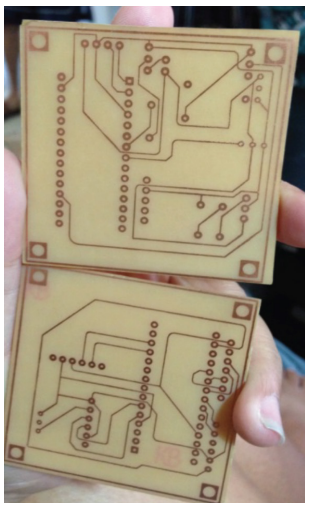

Figure 6 (Right). PCB Boards

The flight was entirely successful: the payload deployed from the container successfully and fell within ranges of the desired descent rates. The sensor payload as well as the raw egg survived the impact of landing as shown in ***Figure 7***, and all telemetry was sent to the Ground Control Station in integrality. Some results are displayed in ***Figure 8***.

Figure 7. Intact Egg

Competing against more than twenty other Universities from the United States, and around the world, the Kapi‘olani Community College Team MOD 6 placed first, and won the 2013 Cansat competition (***Figure 9***).

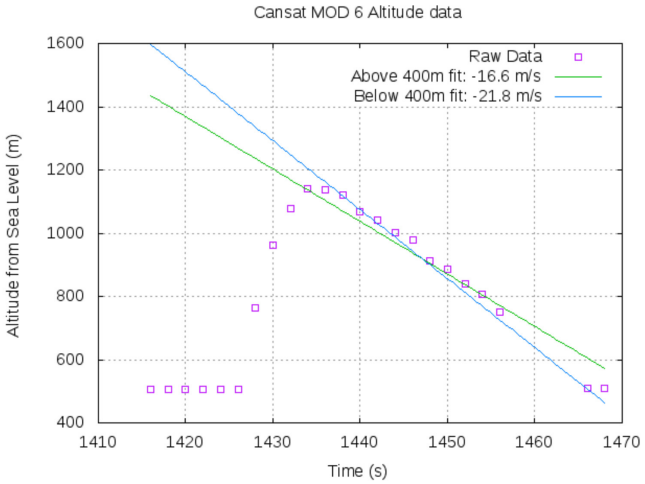

Figure 8. Results

ACKNOWLEDGEMENTS

Kapi‘olani Community College’s STEM Program, the Hawai‘i Space Grant Consortium, Aunty Keolani Noa, and our ‘Ohana for all their support throughout this entire project.

Figure 9. MOD 6 Team, First-Place Award at 2013 Cansat Competition